



저작자표시-비영리-변경금지 2.0 대한민국

이용자는 아래의 조건을 따르는 경우에 한하여 자유롭게

- 이 저작물을 복제, 배포, 전송, 전시, 공연 및 방송할 수 있습니다.

다음과 같은 조건을 따라야 합니다:



저작자표시. 귀하는 원저작자를 표시하여야 합니다.



비영리. 귀하는 이 저작물을 영리 목적으로 이용할 수 없습니다.



변경금지. 귀하는 이 저작물을 개작, 변형 또는 가공할 수 없습니다.

- 귀하는, 이 저작물의 재이용이나 배포의 경우, 이 저작물에 적용된 이용허락조건을 명확하게 나타내어야 합니다.
- 저작권자로부터 별도의 허가를 받으면 이러한 조건들은 적용되지 않습니다.

저작권법에 따른 이용자의 권리는 위의 내용에 의하여 영향을 받지 않습니다.

이것은 [이용허락규약\(Legal Code\)](#)을 이해하기 쉽게 요약한 것입니다.

[Disclaimer](#)

Ph.D. Dissertation of Science Education

Understanding of Antarctic ice mass balance  
using multiple remote sensing and climate models

다중 인공위성 센서 및 기후 모델을 활용한  
남극 얼음 질량 변화의 이해

August 2021

Graduate School of Science Education  
Seoul National University  
Earth Science Major

Byeong-Hoon Kim

Understanding of Antarctic ice mass balance  
using multiple remote sensing  
and climate models

Supervised by:  
Prof. Ki-Weon Seo

Submitting a Ph.D. Dissertation of  
Science Education

June 2021

Graduate School of Science Education  
Seoul National University  
Earth Science Major

Byeong-Hoon Kim

Confirming the Ph.D. Dissertation written by  
Byeong-Hoon Kim  
August 2021

Chair \_\_\_\_\_  
Vice Chair \_\_\_\_\_  
Examiner \_\_\_\_\_  
Examiner \_\_\_\_\_  
Examiner \_\_\_\_\_

# Abstract

Over the past few decades, understanding of ice mass changes in Antarctica has been greatly improved by advances in satellite observation and geophysical modeling techniques. Satellite observations have clearly shown evidence of ongoing Antarctic ice mass loss, and numerical models have quantitatively estimated future ice mass loss. Both observation and modeling have found that Antarctic ice mass loss is accelerating and this would continue in the future. Within this century, Antarctica is expected to be the most important contributor to sea-level rise. To accurately predict Antarctic ice mass loss, continuous Antarctic observation is required, and the cause of Antarctic ice mass loss should be understood.

Ice mass variations over Antarctic glaciers are determined by many factors, and their magnitudes differ significantly from glaciers to glaciers. Understanding ice mass variations at individual glaciers are important to project future Antarctic ice mass losses and subsequent sea level rise. Because glacier mass balances are affected by different physical mechanisms associated with atmospheric and oceanic circulations and solid earth deformation, multidisciplinary studies have been required for the accurate understanding of the interaction between Antarctic Ice Sheet (AIS) and the entire Earth system.

In this dissertation, three studies are carried out using multiple climate models and remote sensing data to understand the current status of glacier mass balance in AIS. The first study examines the role of precipitation in AIS ice mass changes, identifying the interaction between atmosphere and cryosphere. It is found that the precipitation accounts for most of the inter-annual ice mass variability in recent decades and about 30% of the acceleration in contemporary ice mass loss can be explained by precipitation decrease. EOF analysis suggests that such precipitation variability is closely related to periodic climate change in the high altitude of the Southern Hemisphere, named Southern Annular Mode (SAM). After removing effects associated with precipitation decrease, Antarctic ice mass loss associated with

glacier dynamics can be obtained.

The second study is to develop a new method to improve the spatial resolution of the Antarctic ice mass change by combining two different satellite observations. Antarctic ice mass change in higher resolution can be estimated by a new linear inversion technique using satellite altimetry and gravimetry observations together. The new method provides monthly ice mass changes (2003-2016) for all Antarctic glaciers with a spatial resolution of 27 km. The high-resolution ice mass data agree better with the ice mass change from the Input-Output method than data conventionally obtained either from gravimetry or altimetry satellite.

The third study estimates the Glacial Isostatic Adjustment (GIA) effect beneath the Antarctic glaciers. This aims to minimize the GIA error in ice mass observations. By comparing the high-resolution mass estimates with multiple climate models, the GIA effect beneath the Kamb Ice Stream (which is located near the Ross Ice Shelf in West Antarctica) is estimated. The estimated GIA effect is then compared with many GIA models. It is found that most of the GIA models overestimate the GIA effect at the Kamb Ice Stream. Given that a number of models simulate the highest GIA rate beneath the Kamb Ice Stream within Antarctic glaciers, this finding has significant implications to improve the accuracy of Antarctic ice mass change by reducing the GIA uncertainty.

Lastly, we aggregate the results of the three studies to project the future mass loss of Antarctic glaciers. This result is distinct from previous studies in that it provides glacial-scale projections of ice mass changes based on ice dynamic effects after removing effects of precipitation and solid earth deformation from glacial-scale ice mass observations.

**Keyword :** Antarctica, Ice Mass Balance, Sea-Level Change, Satellite Remote Sensing, Joint Inversion, Glacial Isostatic Adjustment  
**Student Number :** 2016-30431

# Table of Contents

<b>Chapter 1. Introduction.....</b>	<b>1</b>
<b>Chapter 2. Backgrounds .....</b>	<b>5</b>
2.1 Satellite gravimetry .....	5
2.1.1 Overview & Principle.....	5
2.1.2 Estimation of surface mass densities from GRACE gravity data ..	6
2.1.3 Spatial filtering .....	8
2.2 Satellite altimetry .....	11
2.2.1 Overview & Principle.....	11
2.2.2 Laser & radar altimetry.....	12
2.2.3 Data types .....	13
2.3 Least squares inversion .....	14
2.3.1 Simple least squares for linear inverse problem.....	14
2.3.2 Application of least square inversion to GRACE data .....	16
<b>Chapter 3. Surface mass balance contributions to Antarctic ice mass change investigated by climate models and GRACE gravity data.....</b>	<b>19</b>
3.1 Introduction .....	19
3.2 Data & Methods .....	20
3.2.1 Precipitation models .....	20
3.2.2 EOF analysis of SMB .....	21
3.2.3 REOF analysis of SMB.....	21
3.3 AIS SMB from 1979 to 2017 .....	23
3.4 Observation of AIS SMB .....	29
3.5 Implications of SMB to present-day ice mass loss in AIS .....	34
3.6 Conclusion .....	35
<b>Chapter 4. Estimation of high-resolution Antarctic ice mass balance using satellite gravimetry and altimetry .....</b>	<b>38</b>
4.1 Introduction .....	38
4.2 Data .....	39
4.2.1 GRACE gravity data .....	39
4.2.2 Satellite altimetry data .....	40
4.3 Methods .....	43
4.3.1 Forward Modeling (FM) solution .....	43
4.3.2 Joint estimation using constrained linear deconvolution ..	46
4.3.3 Uncertainties .....	50
4.3.3.1 Uncertainty of GRACE observation .....	52
4.3.3.2 Uncertainty of FM solution .....	52

4.3.3.3 Uncertainty of altimetry-based mass loads .....	54
4.3.3.4 Uncertainty of CLD solution .....	57
4.4 High resolution Antarctic ice mass loads .....	59
4.5 AIS glacier mass balance .....	62
4.6 Conclusion .....	66
<b>Chapter 5. Estimation of GIA effect beneath the Antarctic Glacier using multiple remote sensing and climate models.....</b>	<b>68</b>
5.1 Introduction .....	68
5.2 Data & Method .....	69
5.2.1 Method .....	69
5.2.2 Basin boundary .....	71
5.2.3 SMB models .....	73
5.2.4 Mass densities from GRACE data .....	73
5.2.5 Mass densities from satellite altimetry data .....	74
5.2.6 High-resolution GRACE data and its sensitivity to GIA estimates ..	75
5.3 Result & Discussion .....	77
5.3.1 Estimated mass rates .....	77
5.3.2 GIA mass rate beneath the KIS .....	80
5.4 Conclusion .....	81
<b>Chapter 6. Sea-level projections.....</b>	<b>82</b>
<b>Chapter 7. Conclusion .....</b>	<b>86</b>
<b>Appendix : Glacial mass balance calculated by satellite gravimetry, altimetry, and their joint estimation .....</b>	<b>89</b>
<b>References.....</b>	<b>112</b>
<b>Abstract in Korean .....</b>	<b>122</b>

## List of figures

<b>Figure 3.1</b> Variations of monthly precipitation rates (1979–2017) in Antarctica .....	24
<b>Figure 3.2</b> (a) Antarctic accumulated precipitation accumulation after removing a linear trend (1979–2017) (b) Map of acceleration rate of accumulated precipitation. ....	24
<b>Figure 3.3</b> Leading three modes of EOF analysis from AIS $\Delta$ SMB (accumulated precipitation).....	26
<b>Figure 3.4</b> Spatial and temporal patterns of the first REOF mode calculated from the leading three EOF modes of AIS $\Delta$ SMB. ....	28
<b>Figure 3.5</b> Prediction of $\Delta$ SMB modulated by $\Delta$ SAM using regression analysis.....	28
<b>Figure 3.6</b> Comparison of $\Delta$ SMB and reconstructed $\Delta$ SMB for the first REOF mode over the Pacific Sector and Atlantic–Indian Sector.....	30
<b>Figure 3.7</b> Comparison between $\Delta$ SMB (blue) and GRACE mass estimates $\Delta$ M (red). ....	32
<b>Figure 3.8</b> Spatial patterns and their PCs of leading three EOF modes calculated from $\Delta$ M– $\Delta$ SMB. ....	33
<b>Figure 3.9</b> (a) AIS ice mass change from IMBIE2 estimates. (b) Detrended variability of ice mass $\Delta$ M, $\Delta$ SMB and $\Delta$ D .....	36
<b>Figure 3.10</b> Changes in Antarctic annual mean precipitation (1979–2017) from ERA5 reanalysis. ....	36
<b>Figure 4.1</b> Linear trend maps of Antarctic ice mass change observed by GRACE and satellite altimetry .....	41
<b>Figure 4.2</b> Spatial distributions of land and ocean functions .....	45

<b>Figure 4.3</b> L-curve obtained by varying the regularization factor, $\lambda$ .....	49
<b>Figure 4.4</b> a, b: Linear trend maps of Antarctic ice mass loads estimated by different value of $\lambda$ (a: $\lambda = \mathbf{10^2}$ , b: $= \mathbf{10^6}$ ), c: Time-series of Antarctic ice mass change in each case. ....	51
<b>Figure 4.5</b> Spatial distribution of GRACE errors estimated around the world and in Antarctica.....	53
<b>Figure 4.6</b> Spatial distribution of FM solution error .....	53
<b>Figure 4.7</b> Spatial distribution of $\sigma_{s\_mass}$ , $\sigma_{f\_mass}$ , and $\sigma_A$ ....	56
<b>Figure 4.8</b> Uncertainties of the CLD solution .....	58
<b>Figure 4.9</b> Time-series of Antarctic total mass variability estimated by FM , Altimetry, and revised CLD.....	60
<b>Figure 4.10</b> Linear trend maps of ice mass loads estimated by FM and the revised CLD .....	60
<b>Figure 4.11</b> Similar to Figure 4.4 except that mass fields are smoothed by 400km Gaussian filter .....	61
<b>Figure 4.12</b> Linear trend maps of Antarctic ice mass change from CSR, JPL, and GSFC mascon solutions.....	61
<b>Figure 4.13</b> Comparison of ice mass variability at Pine Island, Thwaites, and Jutulstraumen Glaciers estimated from FM, Altimetry, CLD, and IOM.....	63
<b>Figure 4.14</b> Comparison of linear changes in ice mass estimated from the IOM and three methods.....	65
<b>Figure 5.1</b> Apparent surface mass variability due to GIA effects estimated by multiple GIA models .....	70
<b>Figure 5.2</b> Glacier flow speeds and their directions near KIS provided by MEaSURES2 project.....	72

**Figure 5.3** (a) Map of differences between  $\Delta\sigma_{alt}^*$  and  $\Delta\sigma_{alt}^{**}$ . (b) Map of differences between two mass rates after the joint estimation. .... 78

**Figure 5.4** (a) Linear trend map of estimated mass changes near KIS. The magenta line is the boundary of the KIS. (b) Time-series of mass changes in KIS estimated by SMB models and the revised CLD. (c) Comparison of linear trends in mass variability shown in (b) ..... 78

**Figure 5.5** Similar to Figure 5.4(a) except for the entire Antarctic Ice Sheet ..... 79

**Figure 6.1** (a) Antarctic ice mass change and ice discharge estimates. (b) Future sea-level changes projected using long-term components of ice mass change and ice discharge..... 84

**Figure 6.2** Future sea-level rise projected by mass loss in the Thwaites and Pine Island Glaciers..... 85

**Figure 6.3** Future sea-level rise projected by  $\Delta D$  in the Thwaites and Pine Island Glaciers. GIA model from Caron and Ivins (2019) is used for  $\Delta D$  estimates ..... 85

# Chapter 1. Introduction

Over the past few decades, rapid ice mass loss in the Earth's cryosphere under a warming climate has contributed significantly to global sea-level rise (Slater et al., 2021). Sustained sea-level rise will, in turn, lead to economic, social, and biological damages to humanity in the future. Accurate prediction of future sea-level rise is essential for humanity to establish appropriate control policies against imminent danger. As part of the Coupled Model Intercomparison Project (CMIP), dozens of numerical simulations have been developed by multiple countries, which have estimated sea-level changes over the next few hundred years. According to the special report prepared by Intergovernmental Panel on Climate Change (IPCC) (Oppenheimer et al., 2019), the models predict that the global mean sea-level will be about +0.84 m from the present at the end of this century, under the current rate of climate change. However, the prediction also shows a high variance of 0.61-1.10 m due to different model sensitivities. To further constrain such diverse predictions, it is necessary to improve our understanding of ongoing global change including ice mass loss over polar ice sheets due to climate warming.

Antarctic Ice Sheet (AIS) is the largest ice reservoir in the Earth's cryosphere. If all of the ice in AIS melts, it will cause a sea-level rise of about 58 m, at which time most metropolitan cities on the Earth will sink below sea-level. Recent observations from satellite remote-sensing suggest that the mass loss in AIS's glaciers is the second largest contributor to sea-level rise, following Greenland Ice Sheet. The mass loss rate in Antarctic glaciers measured by multiple remote sensing (1992-2017) is about 105 Gtons (giga-tons) per year, equivalent to global sea-level rise of about 0.29 mm yr<sup>-1</sup> (IMBIE team, 2018). Several studies have also suggested that the rate of AIS' mass loss is accelerating (Chen et al., 2009; Seo et al., 2015; Velicogna et al., 2014), which may lead to more rapid sea-level rise in the future. Even though the mechanisms leading to the acceleration are not yet clear, the current acceleration rate implies that AIS would be the first contributor to sea-level rise

within this century.

The mass loss rates from AIS glaciers evidently differ from each other. During the satellite observation period (since 1979), significant mass loss has been concentrated in the glaciers located in West Antarctica and Antarctic Peninsula. Pine Island and Thwaites Glaciers account for most mass loss in West Antarctica and are expected to be the largest sea-level rise contributors in the near future. In Antarctic Peninsula, the mass loss is evident near Graham Land, located at the northern tip of the Antarctic Peninsula (Rignot et al., 2019). In contrast, there have been ice mass increases in most East Antarctica during the same period, particularly over the Dronning Maud Land located at 20°W - 60°E (Boening et al., 2012). Uniquely, an apparent mass loss, about  $-15 \text{ Gton yr}^{-1}$ , has been found in the Totten Glacier (located at the Wilkes Land) among East Antarctic glaciers (Mohajerani et al., 2018). Various physical mechanisms, such as atmospheric (Boening et al., 2012) and ocean circulations (Dutrieux et al., 2014), subglacial hydrology (Alley et al., 1994), and solid earth response (Whitehouse et al., 2019) would explain such non-uniform distribution of ice mass change at different Antarctic sectors. In contrast, the present-day AIS mass prediction models do not implement all of these complex mechanisms, leading to high uncertainties in future sea-level variability (Kopp et al., 2017).

There are two major issues to improve the prediction accuracy of future Antarctic ice mass variability. The first is, as noted above, to understand causes of ice mass change. Recent studies suggested increasing water temperatures in Antarctic coastal regions as the major cause of the ice mass loss and its acceleration over the past several decades (e.g., Dutrieux et al. (2014); Spence et al. (2017)). This is based on the mechanism that ice-shelf thinning caused by ocean warming weakens the buttressing for inland ice flow, thereby increases ice discharge. Both observations and ice dynamics modeling support this mechanism, but there are still many debates about the ocean forcing as the main cause of ice mass loss. For example, Seo et al. (2015) reported that Antarctic snowfall changes during 2003-2013 could explain the acceleration of ice mass loss by about 56%. This is different from that most

acceleration is caused by increased ice discharge from ocean warming. Quantifying the contribution of the forcing mechanism to ice mass changes would be very useful to the future ice dynamics modeling.

The second is to propose appropriate initial conditions for the ice dynamics modeling by accurately observing Antarctic ice mass change. Over the past few decades, spatio-temporal variability of Antarctic ice mass change has been observed by both satellite gravimetry and altimetry. However, the observations by each technique do not agree with each other due to their own observational limits. For example, satellite gravimetry has a spatial resolution of hundreds of kilometers, making it difficult to identify the mass change signals occurring at individual glaciers which areas are smaller than satellite gravity resolution. In addition, the inaccuracy of the model correction for the uplift rate of solid earth (i.e., glacial isostatic adjustment (GIA)) results in a large error in estimating the ice mass change ( $\sim 40$  Gton  $\text{yr}^{-1}$ ) (Shepherd et al., 2012). Satellite altimeters observe changes in ice surface elevation at much higher spatial resolutions than satellite gravimetry (within a few kilometers), but have significant error sources when converting the measured elevations into ice mass variability due mostly to incorrect understanding of firn density. Continuous efforts are required to overcome such limitations to understand the ongoing Antarctic ice mass change more accurately.

Therefore, this dissertation (1) examines precipitation effect to on-going AIS mass loss, (2) develops a new method for accurate AIS mass changes by combining different satellite observations and (3) reduces uncertainty in AIS mass loss estimate associated with GIA effect. Chapter 3 presents a study on the contribution of Antarctic snowfall to ice mass changes. Previous studies have reported that post-industrial climate warming has increased Antarctic snowfall over the past 200 years. However, precipitation over the past 40 years has not shown this increasing trend. This study investigates the underlying causes of snowfall variability during 1979-2017 and quantitatively analyzes its impact on Antarctic ice mass change. In Chapter 4, linear inversion scheme is developed by merging two types of data observed from

satellite gravimetry and altimetry. An unprecedented high-resolution Antarctic ice mass change is estimated and cross-validated by estimates from other method (Input-Output Method). Chapter 5 is a study of estimating the solid earth's uplift rate (GIA) beneath the Antarctic glaciers. Geophysical models poorly constrain the present-day GIA effect in AIS. By comparing satellite observations and climate models, this study effectively isolates the mass change induced by GIA under Kamb Ice Stream (KIS), where showing the highest uplift rates in multiple numerical GIA models. The three studies are expected to contribute for accurate projection of sea-level rise by extending our understanding of Antarctic ice mass change (Chapter 6). The concluding remarks are presented in Chapter 7.

# Chapter 2. Backgrounds

## 2.1. Satellite gravimetry

### 2.1.1 Overview & Principle

Since May 2002, the time-varying gravity field caused by the mass re-distribution on the Earth's surface has been observed by the GRACE. The GRACE mission was terminated in 2017, and the new satellite mission, GRACE Follow-On (GFO) (2018-present) has continued gravity observations. GRACE and GFO consists of twin satellites in the along-track direction, orbiting around the earth along the equi-geopotential surface at an altitude of about 500km from the surface. Varying gravitational potential modulates the distance between the two satellites, which is continuously observed by microwave interferometry mounted on each satellite body. After sensor calibration, GRACE provides accurate range rate data. An inversion using range-rate data and other auxiliary observations yields gravitational fields of the Earth including static components due to solid earth and time-varying components. The time-varying gravitational fields are caused by the mass distribution associated with atmospheric pressure, ocean bottom pressure, terrestrial water storage (TWS), ice mass change, and mantle creeping. Among these, the atmospheric and oceanic effects are well understood by the development of numerical model (e.g., Atmosphere and Ocean De-Aliasing (AOD) product) and thus removed from the gravitational fields. GRACE and GFO have provided the gravitational fields represented by spherical harmonic (SH) coefficients, usually with monthly time intervals.

Despite the low spatial resolution (hundreds of kilometers), GRACE's high accuracy ( $\sim 2$  mm water thickness (Wahr et al., 1998)) has allowed effective detection of global- and regional- scale mass variabilities. At the global scale, GRACE observations have been used to estimate the rate of global sea-level rise induced by the land water inflow. GRACE also has been used to investigate Earth's dynamic processes such as geocenter variations (Swenson et al., 2008) and polar

motion (Seo et al., 2021). At the regional scale, GRACE observations have been applied to observe the geophysical phenomena such as river and groundwater storage variability (e.g., Eom et al. (2017); Rodell et al. (2009)), the mass balance of ice sheet and glaciers (e.g., Seo et al. (2015); Velicogna and Wahr (2013)), co-seismic and post-seismic deformation (e.g., Chen et al., (2007)), and modern sediment discharge process (e.g., Mouyen et al. (2018)).

### 2.1.2. Estimation of surface mass densities from GRACE gravity data

The SH coefficients ( $C_{lm}$  and  $S_{lm}$ , in which  $l, m$  are degree and order, respectively) provided by GRACE data centers can be converted into the geoid (Wahr et al., 1998):

$$N(\theta, \phi) = a \sum_{l=0}^n \sum_{m=0}^l \tilde{P}_{lm}(\cos\theta) (C_{lm}\cos(m\phi) + S_{lm}\sin(m\phi)) \quad (2.1)$$

where  $a$  is the radius of the Earth, and  $\tilde{P}_{lm}$  are normalized associated Legendre functions.  $\theta$  and  $\phi$  are colatitude and longitude, respectively. In general, data users utilize coefficients of less than degree 60 ( $n < 60$ ) to avoid higher measurement noise that increases with higher degrees. The geoid is mostly determined by static component of Earth gravitational field. By removing temporal mean values of SH coefficients from the original data, we can obtain the time-varying geoid anomalies:

$$\Delta N(\theta, \phi, t) = a \sum_{l=0}^n \sum_{m=0}^l \tilde{P}_{lm}(\cos\theta) (\Delta C_{lm}\cos(m\phi) + \Delta S_{lm}\sin(m\phi)) \quad (2.2)$$

The geoid anomalies,  $\Delta N$  (indicated as SH coefficients), is caused by the gravitational attraction of the surface mass density anomalies,  $\Delta\sigma$ , and the relation between the two is (Wahr et al., 1998):

$$\begin{bmatrix} \Delta C_{lm} \\ \Delta S_{lm} \end{bmatrix}_{mass} = \frac{3}{4\pi a \rho_{ave}(2l+1)} \int \Delta\sigma(\theta, \phi, t) \tilde{P}_{lm}(\cos\theta) \begin{bmatrix} \cos(m\phi) \\ \sin(m\phi) \end{bmatrix} \sin\theta d\theta d\phi \quad (2.3)$$

where  $\rho_{ave}$  is the average density of the Earth ( $\sim 5517$  kg). The elastic earth underlain by mass loads (represented by  $\Delta\sigma$ ) is radially deformed, and such earth deformation induces additional geoid perturbation. This effect can be estimated by introducing the load Love number,  $k_l$ , a series of numbers representing geoid perturbation as a point mass is applied in an elastic earth:

$$\begin{bmatrix} \Delta C_{lm} \\ \Delta S_{lm} \end{bmatrix}_{solid\ earth} = \frac{3k_l}{4\pi a \rho_{ave}(2l+1)} \int \Delta\sigma(\theta, \phi, t) \tilde{P}_{lm}(\cos\theta) \begin{bmatrix} \cos(m\phi) \\ \sin(m\phi) \end{bmatrix} \sin\theta d\theta d\phi. \quad (2.4)$$

The total geoid change caused by the mass load and corresponding solid earth deformation is sum of equations (2.3) and (2.4)

$$\begin{bmatrix} \Delta C_{lm} \\ \Delta S_{lm} \end{bmatrix} = \begin{bmatrix} \Delta C_{lm} \\ \Delta S_{lm} \end{bmatrix}_{mass} + \begin{bmatrix} \Delta C_{lm} \\ \Delta S_{lm} \end{bmatrix}_{solid\ earth} \quad (2.5)$$

Similar to equation (2.2), the surface mass distribution on the Earth's surface ( $\Delta\sigma(\theta, \phi, t)$ ) can also be expressed by introducing corresponding SH coefficients,  $\Delta\hat{C}_{lm}$  and  $\Delta\hat{S}_{lm}$ :

$$\Delta\sigma(\theta, \phi, t) = a\rho_w \sum_{l=0}^n \sum_{m=0}^l \tilde{P}_{lm}(\cos\theta) (\Delta\hat{C}_{lm}\cos(m\phi) + \Delta\hat{S}_{lm}\sin(m\phi)) \quad (2.6)$$

where  $\rho_w$  is density of water (1000kg m<sup>-3</sup>) and is a term to assign a unit corresponding to the thickness of the water. Another form of the above equation can be obtained from the orthogonality of SH:

$$\begin{bmatrix} \Delta\hat{C}_{lm} \\ \Delta\hat{S}_{lm} \end{bmatrix} = \frac{1}{4\pi a \rho_w} \int_0^{2\pi} d\phi \int_0^\pi \sin\theta d\theta \Delta\sigma(\theta, \phi, t) \tilde{P}_{lm}(\cos\theta) \begin{bmatrix} \cos(m\phi) \\ \sin(m\phi) \end{bmatrix}. \quad (2.7)$$

Using equation (2.3), (2.4), and (2.7), we obtain a relation between SH coefficients described above:

$$\begin{bmatrix} \Delta\hat{C}_{lm} \\ \Delta\hat{S}_{lm} \end{bmatrix} = \frac{\rho_{ave}(2l+1)}{3\rho_w(1+k_l)} \begin{bmatrix} \Delta C_{lm} \\ \Delta S_{lm} \end{bmatrix}. \quad (2.8)$$

Finally, by inserting  $\Delta\hat{C}_{lm}$  and  $\Delta\hat{S}_{lm}$  into equation (2.6), we can estimate the distribution of surface mass density at a given time using SH coefficients obtained by GRACE:

$$\Delta\sigma(\theta, \phi, t) = \frac{a\rho_{ave}}{3} \sum_{l=0}^n \sum_{m=0}^l \tilde{P}_{lm}(\cos\theta) \frac{2l+1}{1+k_l} (\Delta C_{lm} \cos(m\phi) + \Delta S_{lm} \sin(m\phi)). \quad (2.9)$$

### 2.1.3. Spatial filtering

Atmospheric surface pressure and ocean bottom pressure vary with much shorter time scale than the GRACE observational epoch (about a month). Such pressure fields are corrected in GRACE data by AOD product (numerical model output for barometric pressure and ocean bottom pressure), but residual fields remain and cause spatial aliasing error (Seo et al., 2008). To reduce GRACE's aliasing errors and measurement noise, various types of filtering techniques have been developed such as Gaussian spatial filter (Wahr et al., 1998), decorrelation filter (Swenson & Wahr, 2006), or their combinations (Kusche, 2007). This chapter briefly introduces Gaussian and decorrelation filters, which are most widely used in the post-processing of GRACE data.

Gaussian filtering is a spatial averaging technique applying different weight as determined by Gaussian function for grid points. Let the distribution of the surface mass density at a specific time is  $\Delta\sigma(\theta', \phi')$ , and its Gaussian averaging ( $\Delta\bar{\sigma}(\theta, \phi)$ ) is calculated by using Gaussian averaging function  $W$  (Wahr et al., 1998):

$$\Delta\bar{\sigma}(\theta, \phi) = \int \sin \theta' d\theta' d\phi' \Delta\sigma(\theta', \phi') W(\alpha), \quad (2.10)$$

$$W(\alpha) = \frac{b \exp[-b(1-\cos \alpha)]}{2\pi (1-e^{-2b})} \quad (2.11)$$

where  $\alpha$  is angular distance between  $(\theta, \phi)$  and  $(\theta', \phi')$  on the Earth's surface and  $b$  is defined by

$$b = \frac{-\ln(2)}{(1-\cos(r/a))}. \quad (2.12)$$

$r$  is the distance at which  $W(\alpha)$  drops to half of  $W(0)$  and is referred as the averaging radius.

In the spherical harmonic domain, the Gaussian weighting operator varies depending on the degree ( $l$ ) of coefficients. The Gaussian averaging functions at each degree can be obtained with the following recurrence formula according to Jekeli (1981):

$$W_0 = \frac{1}{2\pi}, W_1 = \frac{1}{2\pi} \left[ \frac{1+e^{-2b}}{1-e^{-2b}} - \frac{1}{b} \right], W_{l+1} = -\frac{2l+1}{b} W_l + W_{l-1} \dots \quad (2.13)$$

Combined with Equation 2.9, the distribution of surface mass density after Gaussian spatial filtering is calculated as follows:

$$\Delta\bar{\sigma}(\theta, \phi, t) = \frac{2\pi a \rho_{ave}}{3} \sum_{l=0}^n \sum_{m=0}^l W_l \tilde{P}_{lm}(\cos\theta) \frac{2l+1}{1+k_l} (\Delta C_{lm} \cos(m\phi) + \Delta S_{lm} \sin(m\phi)). \quad (2.14)$$

Decorrelation filter is to suppress north-south stripes appearing in observed geoid anomalies. The filter utilizes the fact that the GRACE's aliasing errors are

correlated in the spectral domain. Swenson and Wahr (2006) found that SH coefficients larger than order 8 showed smoothly varying patterns with increasing degrees ( $l$ ) at a fixed order, when the degrees are divided by odd and even numbers. And they found that this correlated pattern, spatial aliasing error, produced the north-south stripes in GRACE observations.

The coefficient for each order ( $m$ ) divided by odd and even degrees ( $l$ ) can be approximated by the following  $p$ -order polynomial (Swenson & Wahr, 2006):

$$\tilde{C}_{lm} = \sum_{i=0}^p Q_{lm}^i l^i, \quad (2.15)$$

where  $Q_{lm}^i$  are  $i$ th order coefficients of polynomial.  $Q_{lm}^i$  can be estimated using the least-square fit of the polynomial to the observed stokes coefficients:

$$Q_{lm}^i = \sum_{j=0}^p \sum_{n=l-w/2}^{l+w/2} L_{ij}^{-1} n^j C_{nm}, \quad L_{ij} = \sum_{n=l-w/2}^{l+w/2} n^i n^j. \quad (2.16)$$

Using the above equation, the relationship between  $C_{lm}$  and  $\tilde{C}_{lm}$  can be obtained as follows (Swenson & Wahr, 2006):

$$\tilde{C}_{lm} = \sum_{n=l-w/2}^{l+w/2} \Lambda_{lnm} C_{nm}, \quad (2.17)$$

where  $n$  are even or odd numbers. The decorrelation filter ( $\Lambda_{lnm}$ ) is defined as:

$$\Lambda_{lnm} = \sum_{i=0}^p \sum_{j=0}^p L_{ij}^{-1} n^j l^i. \quad (2.18)$$

SH coefficients approximated by the polynomial fitting are assumed to represent the aliasing error and are subtracted from GRACE SH coefficients to diminish the effect of aliasing error.

## 2.2. Satellite altimetry

### 2.2.1. Overview & principle

Satellite altimetry was developed in the 1970s to observe the Earth's sea level and its changes. Contrary to its original purpose, satellite altimeters were also featured in observing surface elevation changes on the ice surface, leading to a leap forward in polar geophysics. Antarctica is one of the regions where satellite altimetry observations are widely used. Continuous observation of the ice sheet surface elevation has been used to understand the spatial pattern of the anomalous ice volume changes and determine their mechanical causes (e.g., Shepherd et al. (2019)). On smaller spatial scales, satellite altimetry has also been used to detect ice dynamical phenomena such as subglacial lake's activities (e.g., Smith et al. (2009)), grounding line retreat (e.g., Konrad et al. (2018)), and basal melt rates beneath ice shelves (e.g., Pritchard et al. (2012)). Multiple altimetry missions (ERS-1 mission (1991-2000), Topex/Poseidon (1992-2016), ERS-2 (1995-2003), ENVISAT (2002-2012), ICESat (2003-2009)) have been used for Antarctic researches. More recently, the Cryosat-2 (2010-) and ICESat-2 (2018-) missions have been launched, providing more precise observation data.

Satellite altimeters measure two-ways travel time of electromagnetic waves emitting from satellites to Earth's surface and their reflections to the satellites. Considering the speed of light ( $\sim 3.0 \times 10^8$  km s<sup>-1</sup>), the travel time is converted to the distance between the satellites and the surface of the Earth. Surface elevation can be estimated from the difference between the measured range and the distance of the satellite away from the reference surface (e.g., reference ellipsoid). Despite the simple principle of satellite altimetry observation, a number of techniques are necessary to obtain higher measurement accuracy. The satellite's position and orientation are accurately observed by a ground-based positioning system (e.g., Doppler Orbitography and Radiopositioning Integrated by Satellite (DORIS)) and a star-tracker. The arrival time of the reflected wave is delayed as it passes through the neutral atmosphere and ionosphere, which is corrected by observation or climate

reanalysis. The solar and lunar tide vertically deforms the ocean and solid Earth's surface at an hour to monthly time scales, which makes periodic variations in observed elevation change ranging from several tens of centimeters to several meters. Tide models (e.g., FES2004; Lyard et al. (2006)) are used correct this effect.

### **2.2.2. Laser & radar Altimetry**

Satellite altimeters are classified into radar and laser altimeters according to the type of sensor used. In general, radar altimeters use microwaves with a wavelength of 2.2cm (~13.5 GHz, e.g., ERS-1 & 2, ENVISAT, and Cryosat-2), and laser altimeters use visible light with a wavelength of 1064 nm (e.g., ICESat). Because the two sensors use very different wavelengths, their own strength and limitation are apparently distinct. First, radar altimetry using longer wavelengths requires less power for pulse generation. This allows radar altimetry to have wide spatial coverage and to observe elevations in a study area at a higher sampling rate. On the other hand, laser altimeters require more power for pulse generation because it uses shorter wavelength. Since satellites are powered by solar energy, the limited power supply to the laser pulse system requiring much energy makes it difficult to observe the elevation change continuously. To obtain high observational efficiency under the limited power supply, the laser altimeter observes intermittently only during laser operational periods named 'campaigns'. For example, the ICESat-1 mission had been carried out for 596 days in 18 campaigns during 2003-2009 (National Snow & Ice Data Center). Since intermittent observations would induce bias in elevation observations between one campaign and another (inter-campaign bias), additional corrections based on field observations or physical assumptions are required (e.g., Hofton et al. (2013)).

The different wavelengths used for those altimetry also determines their sensitivity to weather conditions. Since the laser wavelength is similar to the size of the cloud particle, the incident wave (with a wavelength of 1064nm) is rapidly dissipated by scattering when it propagates into the cloud layer. If the target area is

covered by cloud, laser altimeters would not observe reflected waves from the Earth's surface. As a result, the observations of laser altimetry are restricted by weather condition. On the other hand, microwaves used in radar altimeters pass through the cloud layer and are not affected by weather conditions. Accordingly, it is possible to estimate the elevation change of the target area with an almost constant sampling rate.

Despite the shortcomings of laser altimetry described above, needs of the laser altimetry missions have been increased. Unlike radar altimetry, which emits waves in the radial directions from satellite, laser altimetry projects pulses straight onto the ground. The resulting size of the footprint (i.e., spatial resolution) is about 70m diameters (ICESat-1; Markus et al. (2017)), which is much smaller than the maximum spatial resolution that can be achieved by radar-type altimetry (about 200m for Cryosat-2 (Wingham et al., 2006)). Moreover, the vertical resolution of the laser altimetry on the ice surface is a few centimeters, which is much higher than that of the radar altimetry, several tens of centimeters to several meters (which depends on the surface topography). By utilizing the high accuracy and precision, laser altimetry have been used to observe alpine regions that are not accessible to radar altimetry (e.g., Treichler and Kääh (2016)), and to validate radar altimetry observations (Wang et al., 2015). Recently the National Aeronautics and Space Administration (NASA) launched the new laser altimetry mission (ICESat-2) in 2018. ICESat-2 operates with three pairs of high-performance beams arranged along a cross-track direction. Each beam has a footprint of about 17m in diameter (Markus et al., 2017), which is useful for improving the accuracy of elevation observations.

### **2.2.3. Data types**

Typically, satellite altimeter data are classified into five types (Level 0-4) according to levels of data processing. Level 0 is primitive observational data such as measurement time, navigating system (e.g., operation of DORIS system and star-trackers), and data quality. This data is managed only by data preprocessing centers

and is not distributed to users for scientific purposes. On the other hand, Level 1-4 data are provided to users after the registration process for permission. Level 1 data includes waveforms, satellite position and orientation, and additional geophysical correction data. In this case, users have to calculate the surface elevations by themselves using the data provided. Level 2 data is estimates of along-track surface elevations, named 'point clouds'. Using the point clouds data, ones can estimate the elevation change at a resolution suitable for the target area. Users are also able to investigate the influence of geophysical correction on the measured elevation anomalies. Level 3 data are along-track geophysical data with additional calculations (e.g., surface elevation anomaly). Finally, Level 4 data is gridded elevation change data calculated from single- or multi-mission satellites (e.g., ice surface elevation change data from Schröder et al. (2019)).

## 2.3. Least squares inversion

### 2.3.1. Simple least squares for linear inverse problem

Least squares are widely used in geophysics to estimate model parameters ( $\mathbf{m}_{est}$ ) to understand complex observational data ( $\mathbf{d}_{obs}$ ):

$$\begin{aligned}\mathbf{d}_{obs} &= [d_1, d_2, d_3, \dots, d_N]^T \\ \mathbf{m}_{est} &= [m_1, m_2, m_3, \dots, m_M]^T\end{aligned}\tag{2.19}$$

where  $N$  and  $M$  are the numbers of data and model parameters, respectively. We can consider a data kernel  $\mathbf{G}$  with a size of  $N \times M$ , which linearly links  $\mathbf{d}_{obs}$  and  $\mathbf{m}_{est}$  like

$$\mathbf{d}_{obs} = \mathbf{G}\mathbf{m}_{est} + \mathbf{e}.\tag{2.20}$$

$\mathbf{e}$  are prediction errors, typically increasing as observational noise increases and/or

model parameters are inaccurately defined. To obtain appropriate model parameters, prediction errors should be minimized. At this time, there are various criteria for measuring the size of errors. The most widely used criterion is least squares, which considers the length of the errors to be the sum of the squares of each anticipated error element:

$$\Phi_1 = \sum_{i=1}^N e_i^2 = \mathbf{e}^T \mathbf{e} = [\mathbf{d}_{obs} - \mathbf{G}\mathbf{m}_{est}]^T [\mathbf{d}_{obs} - \mathbf{G}\mathbf{m}_{est}]. \quad (2.21)$$

Model parameters can be estimated by minimizing  $\Phi_1$  (e.g., Menke (2012), pp 44-45):

$$\mathbf{m}_{est} = [\mathbf{G}^T \mathbf{G}]^{-1} \mathbf{G}^T \mathbf{d}_{obs}. \quad (2.22)$$

Equation (2.22) assumes that each element in  $\mathbf{d}_{obs}$  includes the same level of uncertainty, which is not true for most cases. Each observation has different uncertainty determined by observational conditions. Further, temporal or spatial filtering applied to observations induces high correlation between adjacent observations, creating correlated noise. To consider different noise levels of observational data and their correlation, we can introduce the covariance matrix:

$$\mathbf{C}_{obs} = \begin{bmatrix} E[(n_1 - E[n_1])(n_1 - E[n_1])] & \cdots & E[(n_1 - E[n_1])(n_N - E[n_N])] \\ \vdots & \ddots & \vdots \\ E[(n_N - E[n_N])(n_1 - E[n_1])] & \cdots & E[(n_N - E[n_N])(n_N - E[n_N])] \end{bmatrix} \quad (2.23)$$

where  $n_N$  is the expected noise of the  $N$ th element, and  $E$  denotes the mean of its argument. Model parameters should be obtained by giving more weight to accurate observations, and vice versa. In many cases, the weighting factor is assumed to be the inverse of the covariance matrix. Accordingly, the minimizing problem given in Equation (2.21) is changed to:

$$\Phi_2 = [\mathbf{d}_{obs} - \mathbf{G}\mathbf{m}_{est}]^T \mathbf{C}_{obs}^{-1} [\mathbf{d}_{obs} - \mathbf{G}\mathbf{m}_{est}]. \quad (2.24)$$

The solution to minimize  $\Phi_2$  in Equation (2.24) is

$$\mathbf{m}_{est} = [\mathbf{G}^T \mathbf{C}_{obs}^{-1} \mathbf{G}]^{-1} \mathbf{G}^T \mathbf{C}_{obs}^{-1} \mathbf{d}_{obs}. \quad (2.25)$$

The term  $[\mathbf{G}^T \mathbf{C}_{obs}^{-1} \mathbf{G}]^{-1} \mathbf{G}^T \mathbf{C}_{obs}^{-1}$  in Equation (2.25) is called “the generalized inverse” [Menke, 2015]. If the observations are uncorrelated and have a uniform variance of  $\sigma_{obs}$  (i.e.,  $\mathbf{C}_{obs} = \sigma_{obs}^2 \mathbf{I}$ ), Equation (2.25) is equal to Equation (2.22).

### 2.3.2. Application of least square inversion to GRACE data

The least square inversion introduced in the previous chapter can also be applied to GRACE observations. Seo et al. (2020) assumed that low-resolution surface mass densities observed by GRACE are linearly related to the actual surface mass densities. Because low-resolution of surface mass densities of GRACE data is mainly caused by the application of the Gaussian filter to suppress noise, the linear relationship can be obtained as follows, similar to Equation (2.20):

$$\mathbf{M}_G = \mathbf{G}\hat{\mathbf{m}} + \mathbf{e} \quad (2.23)$$

where  $\mathbf{M}_G$  is surface mass densities from GRACE, and  $\mathbf{G}$  is Gaussian smoothing operator.  $\hat{\mathbf{m}}$  is surface mass density (i.e., model parameter) to be estimated. In accordance with Equation (2.22), the least square solution to minimize the prediction error ( $\mathbf{e}$ ) of the above Equation is:

$$\hat{\mathbf{m}} = [\mathbf{G}^T \mathbf{G}]^{-1} \mathbf{G}^T \mathbf{M}_G. \quad (2.24)$$

Typically, the solution ( $\hat{\mathbf{m}}$ ) includes much noise because Equation (2.24) is a spatial deconvolution that amplifies the observational noise included in  $\mathbf{M}_G$ . To suppress the noise, we can add a constraint to the cost function (Menke, 2012):

$$\Phi_{LS} = |\mathbf{M}_G - \mathbf{G}\hat{\mathbf{m}}|^2 + \lambda |\sum_{n=1}^k \mathbf{D}_n(\hat{\mathbf{m}} - \mathbf{m}_0)|^2 \quad (2.25)$$

where  $\mathbf{m}_0$  is a-priori estimate of  $\hat{\mathbf{m}}$  which is set to zero here. Typically,  $\mathbf{D}_n$  are matrices that measures the length of solution, but in Seo et al. (2020), they used  $\mathbf{D}_n$  as the spatial gradient (i.e., steepness) of  $\hat{\mathbf{m}}$  with inverse-distance weighing, by considering the spatial characteristic of GRACE data.  $\lambda$  is regularization factor that adjust the steepness of the solution For example,  $\mathbf{D}_1$  consists of the following elements:

$$\mathbf{D}_1 = \begin{bmatrix} -1/r_{12} & 1/r_{12} & 0 & \dots \\ -1/r_{13} & 0 & 1/r_{13} & \dots \\ \vdots & \vdots & \ddots & \dots \\ -1/r_{1k} & 0 & \dots & 1/r_{1k} \end{bmatrix} \quad (2.26)$$

in which  $r_{1n}$  ( $n=2, 3, \dots, k$ ) is the distance between the first and  $n$ th mass load. Including steepness constraint, we obtain a new solution that minimizes spatial gradients while minimizing prediction error,

$$\hat{\mathbf{m}} = [\mathbf{G}^T \mathbf{G} + \lambda \mathbf{W}]^{-1} \mathbf{G}^T \mathbf{M}_G \quad (2.27)$$

where  $\mathbf{W} = \sum_{n=1}^k \mathbf{D}_n^T \mathbf{D}_n$ .

Seo et al. (2020) also modified Equation (2.27) to suppress the spatial leakage problem of GRACE data. They added another constraint  $\mathbf{H}$  whose diagonal elements are ones for ocean and zeros for all others:

$$\mathbf{H}\hat{\mathbf{m}} = h \quad (2.28)$$

in which  $h$  is zero vector. Using Equation (2.28), the ocean mass loads in  $\hat{\mathbf{m}}$  are effectively constrained to zero, and thus the mass densities leaked into the ocean area can be recovered to the inland area. By including Equation (2.28) in the cost function, we obtain two equations which must be solved simultaneously by combining them into the matrix from (Chapter 3.4 in Menke (2012)):

$$\begin{bmatrix} \hat{\mathbf{m}} \\ \hat{\mathbf{n}} \end{bmatrix} = \begin{bmatrix} G^T G + \lambda W & H^T \\ H & 0 \end{bmatrix}^{-1} \begin{bmatrix} G^T M_G \\ h \end{bmatrix} \quad (2.29)$$

where  $\hat{\mathbf{n}}$  is null vector.

Determining the regularization factor,  $\lambda$ , plays an important role in the spatial resolution and quality of the solution. The most widely used method for selecting an appropriate  $\lambda$  is to draw an L-curve, which evaluates the geometry of the solution as well as the similarity between the observation and solution. The application of L-curve to the inversion of GRACE observation will be addressed further in Chapter 4.

# **Chapter 3. Surface mass balance contributions to Antarctic ice mass change investigated by climate models and GRACE gravity data**

## **3.1. Introduction**

A rise in global mean sea level (GMSL) is generally associated with global warming, and there is great interest in projecting future changes in GMSL in climate forecasts. The rate of GMSL increase is estimated at about  $1.9 \text{ mm yr}^{-1}$  during the 20th century (Jevrejeva et al., 2014), increasing to  $3.1 \text{ mm yr}^{-1}$  during the past three decades (2018). The increase in GMSL rate in recent decades is mostly attributed to water mass inflow from mountain glaciers ( $0.7 \text{ mm yr}^{-1}$ ) and from the Greenland Ice Sheet (GrIS) ( $0.5 \text{ mm yr}^{-1}$ ) (Shepherd et al., 2018). During the same period, the Antarctic Ice Sheet (AIS) has contributed about  $0.3 \text{ mm yr}^{-1}$  to GMSL, roughly half the amount from the GrIS. However, the Ice sheet Mass Balance Inter-comparison Exercise 2 (IMBIE2) (Shepherd et al., 2018) reported recently that the rate of AIS ice mass loss has evidently increased during the last decade; the rate was estimated to about  $-47 \text{ Gton yr}^{-1}$  during 1992-2006, increasing to  $-194 \text{ Gton yr}^{-1}$  during 2007-2017. If such an acceleration of AIS ice mass loss continues, then the AIS would soon become a larger contributor to GMSL change than the GrIS.

AIS ice mass balance is determined by ice discharge (D) and surface mass balance (SMB). The latter includes precipitation, sublimation and meltwater runoff, but sublimation and runoff are negligible for the AIS (Van Wessem et al., 2014). The empirical projection of AIS mass balance and its contribution to GMSL is based on the assumption that long-term variations of AIS mass is mostly controlled by D which undergoes slow (decadal and longer) variability because significant long-term variations have not been seen in AIS precipitation rates during the last a few decades (Shepherd et al., 2018). However, the previous study (Seo et al., 2015) based on

comparison of GRACE gravity data and a SMB reanalysis model estimated that acceleration of ice mass loss in the Amundsen Sea Embayment portion of the AIS during 2003-2013 was  $-13.6 \text{ Gton yr}^{-2}$ , and that precipitation decrease during the same period explained about 60% of this ( $-8.2 \text{ Gton yr}^{-2}$ ). Precipitation effects on AIS mass balance (i.e., SMB) should be carefully considered in order to understand multi-decadal and longer AIS mass changes, given that precipitation tends to vary on relatively long climate oscillation time scales. Therefore, abrupt AIS mass loss during the last decade found in IMBIE2 needs to be understood by separating contributions of D and SMB.

The objective of this study is to examine AIS SMB since 1979 using the state-of-the-art numerical model and its contribution to AIS mass balance. It will be shown that inter-annual and longer SMB variations are significant. This study also finds a bi-polar SMB pattern associated with a precipitation decrease in the Pacific sector, and increases in Atlantic and Indian sectors, which is highly correlated with the Southern Annular Mode (SAM). AIS SMB variations produce apparent abrupt AIS mass loss, and after correcting for the SMB contribution, AIS mass loss associated with D shows a steady increase.

## **3.2 Data & Methods**

### **3.2.1 Precipitation models**

To examine AIS SMB, the ERA5 (Hersbach et al., 2019) precipitation, an improved version of the previous ERA-Interim (Dee et al., 2011) reanalysis was used. ERA-Interim has been known to represent well both sub-annual (Palermo et al., 2017) and long-term variability of AIS precipitation (Bromwich et al., 2011). The horizontal resolution of ERA5 is notably improved (31km compared to ERA-Interim, 80km), similar level to existing regional climate models, RACMO (=27km) (Van Wessem et al., 2014) or MAR (=35km) (Agosta et al., 2019). AIS precipitation over Antarctic drainage basins determined by satellite altimeter observations (Zwally et al., 2012) was considered.

### 3.2.2 EOF analysis

Geophysical data can be contained in a matrix of dimension of  $p \times n$  (where  $p$  and  $n$  are the lengths of discrete spatial and temporal components, respectively). The matrix is separated into several orthogonal modes using singular value decomposition (SVD):

$$\Delta\text{SMB} = \text{USV}^T, \quad (3.1)$$

in which  $U$  and  $V$  are orthogonal matrix with dimension of  $p \times p$  and  $n \times n$ , respectively. The superscript  $T$  means matrix transpose. The  $i$ th column of  $U$  represents the spatial pattern of the  $i$ th mode, and similarly the  $i$ th column of  $V$  represents the temporal variation (principal component) of the  $i$ th mode.  $S$  is a rectangular matrix with only diagonal components, and each component is a singular value of each mode. If the  $i$ th diagonal component of  $S$  is  $d_i$ , the explained variance (EV) of the corresponding mode is:

$$EV = \frac{d_i^2}{\sum_{j=1}^m d_j^2} \times 100 \quad (\%), \quad (3.2)$$

where  $m$  is equal to  $p$  or  $n$ , whichever is smaller.

### 3.2.3 REOF analysis

Rotated EOF (REOF) analysis is a variant of EOF analysis. Typically, it may be difficult to interpret individual EOF modes because they are spatially coupled so a specific variation is contained in multiple modes. REOF transforms EOF modes into coordinate axes rotated relative to the original. To obtain rotated modes (or axes) from the original EOF modes we use a rotation matrix:

$$W = U_m R \quad (3.3)$$

where  $U_m$  is a  $p \times m$  matrix consisting of  $m$  column vectors representing selected EOF modes.  $R$  is a  $m \times m$  orthonormal matrix to rotate the EOF modes ( $U_m$ ) to new modes ( $W$ ) while keeping their orthogonality during rotation.

The rotation matrix  $R$  needs to be determined to obtain  $W$  in which vector columns are uncoupled from one another. The degree of 'uncoupling' for the  $W$  can be evaluated at a geographic point with a maximum value in a single mode while values at the same point are near 0 in other modes. There are various criteria to solve such an optimization problem. Here we adopt the VARIMAX approach, the most widely used (Harman, 1976; Navarra & Simoncini, 2010). VARIMAX appraises the degree of uncoupling for a rotated mode based on maximizing an objective function:

$$f(W_k) = \frac{1}{p} \sum_{i=1}^p l_{i,k}^4 - \frac{1}{p^2} \left[ \sum_{i=1}^p (l_{i,k}^2) \right]^2 \quad (3.4)$$

where  $l_{i,k}$  is the value at  $i$ th grid-point explained only by the  $k$ th column of  $W$ , i.e.,  $W_k$ .

Practically, the  $W$  (and simultaneously  $R$ ) is determined using an iterative scheme. First, a column vector is calculated from the sum over each row of  $U_m$  and then normalized by its vector norm. This is equivalent to  $W$  in equation (3.3) when using the initial  $R$ ,  $R_0$ : the first column in  $R_0$  is an  $m \times 1$  vector of ones divided by its norm, namely  $\tilde{R}_1$ , and the other columns are all zeros. One seeks a local maximum of the objective function (equation (3.4)) by finely tuning  $\tilde{R}_1$  iteratively. After determined the optimal  $\tilde{R}_1$ , the second and following columns ( $\tilde{R}_k$  with  $k = 2, \dots, m$ ) are determined in the same manner, but constrained to be orthogonal to all previous  $\tilde{R}_n$  ( $n = 1, \dots, k - 1$ ). Finally, rotated modes  $W$  are calculated from equation (3.4) with the optimal rotation matrix,  $R$  where  $R = [\tilde{R}_1 \ \tilde{R}_2 \ \dots \ \tilde{R}_m]$ .

### 3.3. AIS SMB from 1979 to 2017

Precipitation rates (1979-2017) of numerical models show common variation in sub-annual and annual time scales (Figure 3.1). This may be partly because that they are commonly forced by the European Centre for Medium Range Weather Forecasts (ECMWF) reanalyses (Agosta et al., 2019; Dee et al., 2011). There are minor inter-annual and longer period variations, and long-term trends are not statistically significant (Bromwich et al., 2011). The linear trend of precipitation rates from ECMWF Reanalysis 5th Generation (ERA5) (Hersbach et al., 2019) is estimated to  $-0.1 \pm 0.5$  Gton  $\text{yr}^{-1}$  with a 95% confidence interval, and other models provide similar near-zero rates. As a result, it has been thought that the role of precipitation in long-term AIS mass variation can be ignored (Shepherd et al., 2018). The most recent state-of-the-art reanalysis, ERA5, was used to investigate this.

AIS mass change ( $M$ ) is approximately determined by ice discharge ( $D$ ) and SMB, related by  $M = SMB - D$ . Precipitation accumulation (time integration of precipitation) contributes to AIS mass change in SMB. Small long-term precipitation variations will tend to be amplified, while shorter period but larger sub-annual and annual fluctuations will tend to be suppressed by integration. A small negative linear trend in precipitation rate, for example, can produce a significant acceleration in ice mass loss. Figure 3.2a shows accumulation of precipitation (approximately equivalent to SMB). A linear trend was removed from accumulated precipitation time series, equivalent to removing the mean value in precipitation rate, which is not the focus of this study. Detrended SMB ( $\Delta\text{SMB}$ ) from ERA5 shows inter-annual and longer variations (Wouters et al., 2013), but an acceleration rate in  $\Delta\text{SMB}$  is minor over the entire study period (1979-2017). The acceleration at grid points is estimated to obtain acceleration maps in Figure 3.2b. Only statistically significant values (non-zero within a 95% confidence interval) are plotted. Acceleration rates in most regions are significant despite their small spatial average over the entire AIS ( $-0.3$  Gton  $\text{yr}^{-2}$ ). For example, a positive acceleration of about 2 Gton  $\text{yr}^{-2}$  is shown in Atlantic and

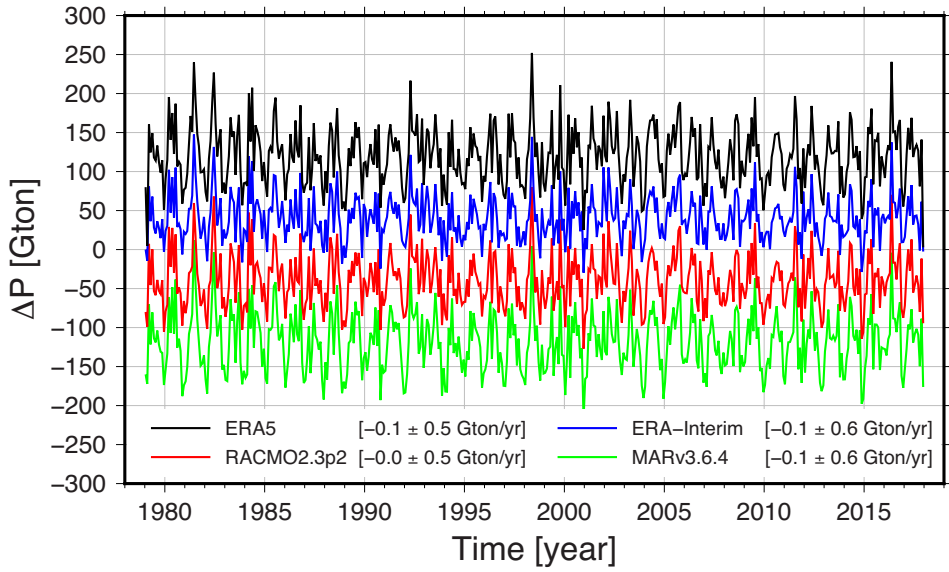


**Figure 3.1.** Variations of monthly precipitation rates (1979-2017) in Antarctica: ERA5 (black), ERA-interim (blue), RACMO2.3p2 (red) and MARv3.6.4 (green). Linear trends (1979-2017) of each model are shown in parentheses. Vertical offsets are applied to distinguish each time series.

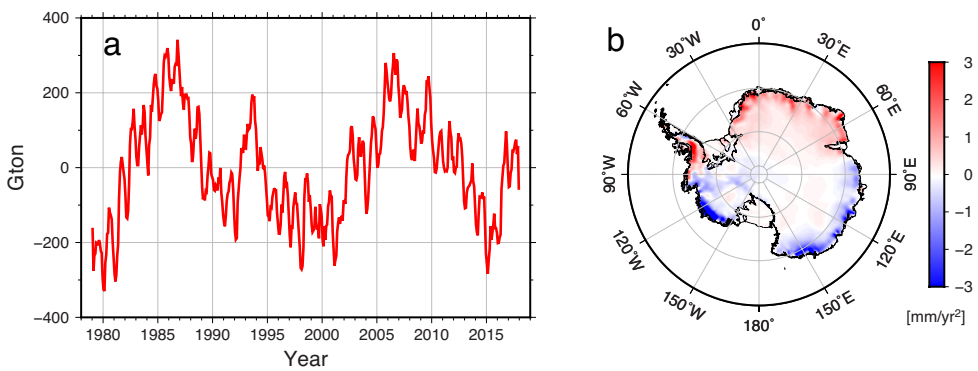
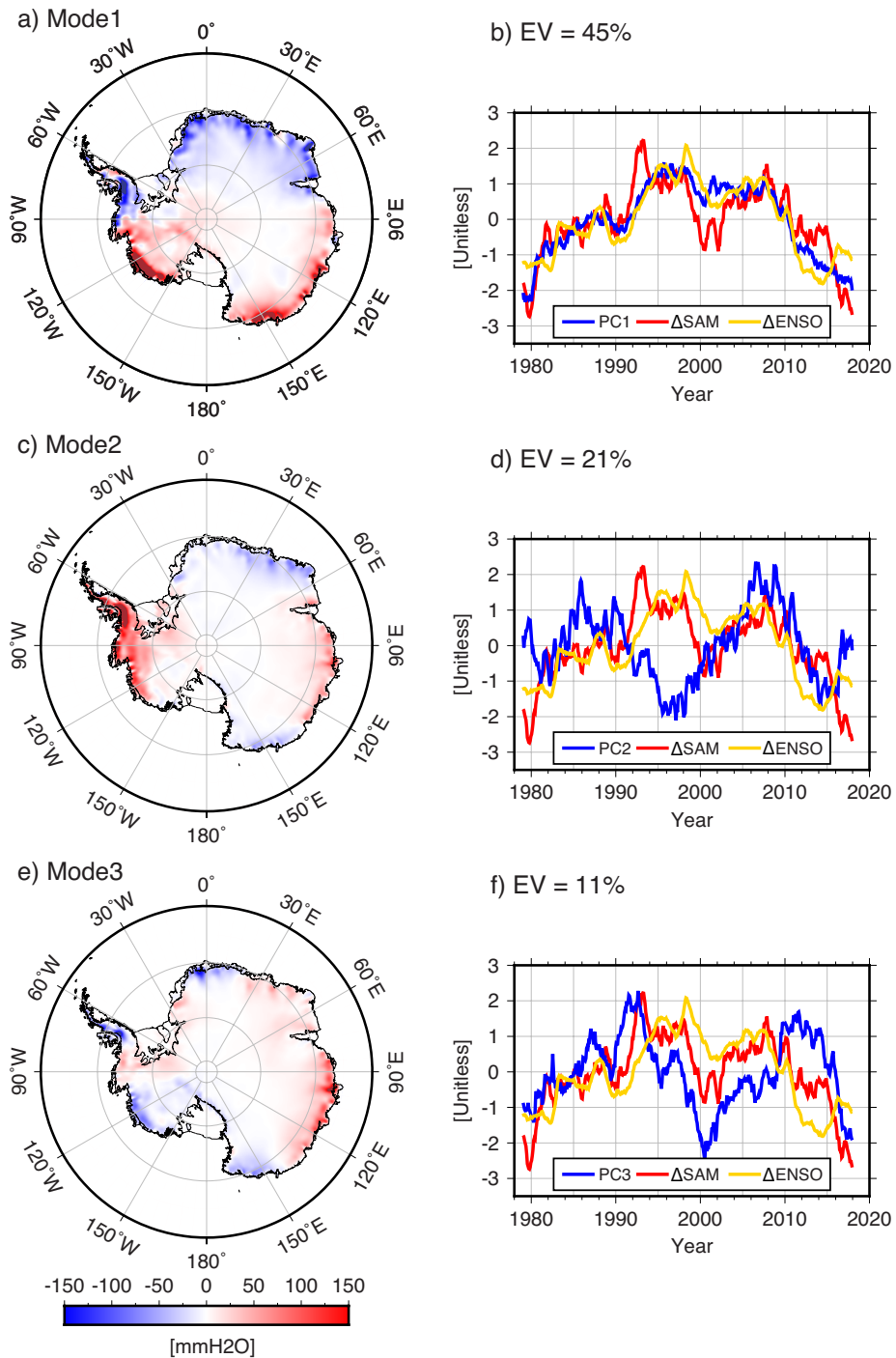


**Figure 3.2.** (a) Antarctic accumulated precipitation accumulation after removing a linear trend (1979-2017) (b) Map of acceleration rate of accumulated precipitation.

Indian Sectors while a negative acceleration of about  $-2 \text{ Gton yr}^{-2}$  is found in the Pacific Sector. A spatial pattern of significant acceleration bisects the entire AIS.

AIS SMB shows significant variability at inter-annual to decadal time-scales as indicated in Figure 3.2. Because such variability is important to ongoing AIS ice mass change, it is important to understand its underlying causes. Medley and Thomas (2018) reviewed the two causes of long-term variations in AIS precipitation rates, thermodynamic processes and atmospheric circulation. The first is associated with a near exponential increase in water vapor with increasing air temperature (Clausius-Clapeyron relation) and would induce a long-term positive trend in precipitation rate over the past 100 years (Held & Soden, 2006). However, AIS  $\Delta\text{SMB}$  acceleration ( $-0.3 \pm 0.2 \text{ Gton yr}^{-2}$ ) is small (implying a near-zero trend in precipitation rate). This indicates relatively small thermodynamic process contributions to AIS precipitation during this period (1979-2017).

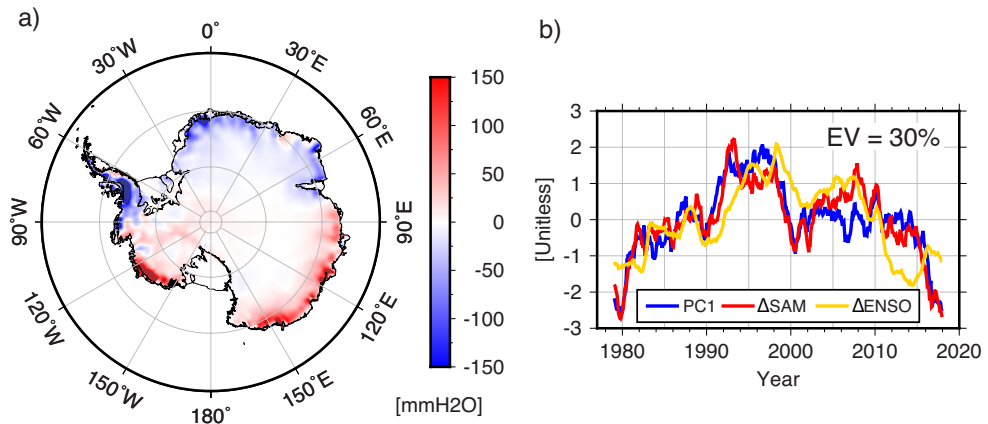
SAM and El Niño-Southern Oscillation (ENSO), are primary modes of atmospheric circulation variability in Southern high latitudes (Bromwich et al., 2000; Genthon et al., 2003). For example, SAM modulates low pressures around Antarctica and thus alternates warm/moist and cold/dry air advection (Genthon et al., 2003). As a result, the previous study (Medley & Thomas, 2018) suggested that a positive trend in SAM is a cause of a decrease in AIS net precipitation rate. To examine this, we first use ordinary EOF analysis on the area-weighted  $\Delta\text{SMB}$  field determined from ERA5 model. Figure 3.3 shows the three leading EOF modes explaining 77% of  $\Delta\text{SMB}$  variance. The left panels are the spatial patterns of each mode. Blue lines in the right panels show corresponding PCs. Time-integrated SAM and ENSO indices can also be compared with  $\Delta\text{SMB}$  (time integration of precipitation rate). Time-integrated ENSO indices have also been used to examine ENSO effects on ice shelf volume changes (Paolo et al., 2018). Red and yellow lines in the right panels show time-integrated SAM and ENSO indices after removing linear trends ( $\Delta\text{SAM}$  and  $\Delta\text{ENSO}$ , respectively) as done for  $\Delta\text{SMB}$ . The first mode PC shows a long-term variation similar to  $\Delta\text{SAM}$  and  $\Delta\text{ENSO}$  (Figure 3.3b) confirming that Antarctic



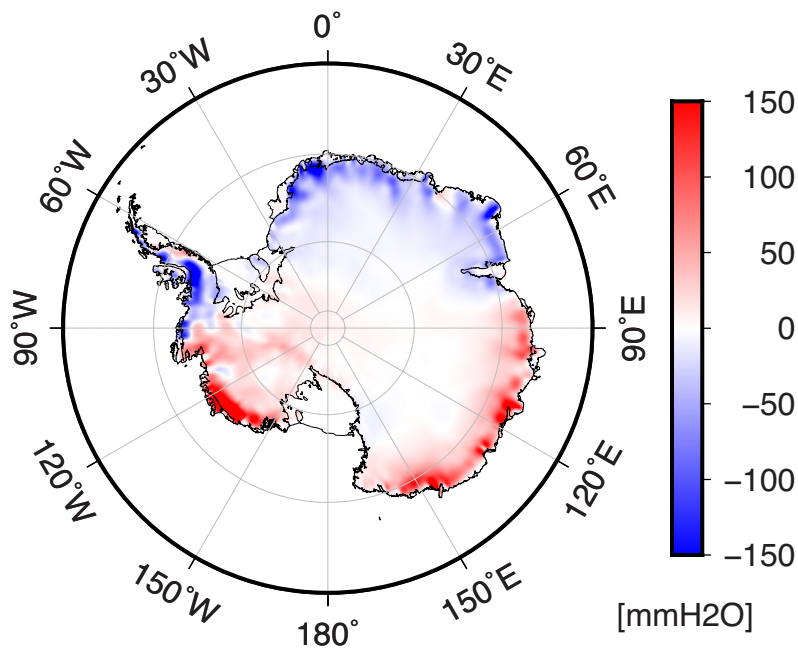
**Figure 3.3.** Leading three modes of EOF analysis from AIS  $\Delta$ SMB (accumulated precipitation). Each of red and yellow lines in right panels show  $\Delta$ SAM (time-integrated) and  $\Delta$ ENSO (time-integrated), respectively. For clarity, both  $\Delta$ SAM and  $\Delta$ ENSO are displayed reversed in sign.

precipitation is affected by SAM and ENSO (Bromwich et al., 2000; Genthon et al., 2003). However, there is no apparent inter-annual variability in the first PC unlike both indices. On the other hand, second and third mode PCs partly show similar inter-annual variations as  $\Delta$ SAM during the latter (2010-2015) and former (1979-2000) periods, respectively (Figures 3.3d and 3.3f), suggesting that  $\Delta$ SMB signals modulated by  $\Delta$ SAM are mapped into multiple EOF modes. It is difficult to interpret the multiple modes if this is the case.

The rotated EOF (REOF) analysis can be applied to map ordinary EOF modes into other modes by rotating associated basis functions. If AIS  $\Delta$ SMB is dominated by  $\Delta$ SAM or  $\Delta$ ENSO (i.e., precipitation rate is dominantly affected by SAM or ENSO (Genthon et al., 2003)), the first REOF mode PC should be similar to  $\Delta$ SAM or  $\Delta$ ENSO. The left panel of Figure 3.4 shows the first REOF spatial mode. The blue line in the right panel is its temporal variation, and the red and yellow lines show  $\Delta$ SAM and  $\Delta$ ENSO, respectively. The explained variance of the first REOF mode is 30%. The first REOF mode spatial pattern is similar to that of the first EOF mode but the first mode REOF PC shows a very similar variation to  $\Delta$ SAM (with a correlation coefficient of 0.89).  $\Delta$ ENSO also shows similar variations to the REOF PC but their correlation (0.62) is lower than for  $\Delta$ SAM, which is consistent with the previous study (Genthon et al., 2003). These results show that since 1979 SMB has been mainly modulated by SAM, producing a bi-polar pattern: acceleration of ice mass loss in the Pacific Sector and acceleration of gain in Atlantic and Indian Sectors. Similar result can also be obtained by regression analysis.  $\Delta$ SMB modulated by  $\Delta$ SAM can be predicted by a linear regression between the two at each grid point during the study period. Figure 3.5 shows the resulting prediction which is very close to the spatial pattern and amplitude shown in Figure 3.4a.



**Figure 3.4.** Spatial (a) and temporal (b) patterns of the first REOF mode calculated from the leading three EOF modes of AIS  $\Delta$ SMB. Red line in (b) shows  $\Delta$ SAM. For clarity,  $\Delta$ SAM and  $\Delta$ ENSO are displayed with reversed sign.



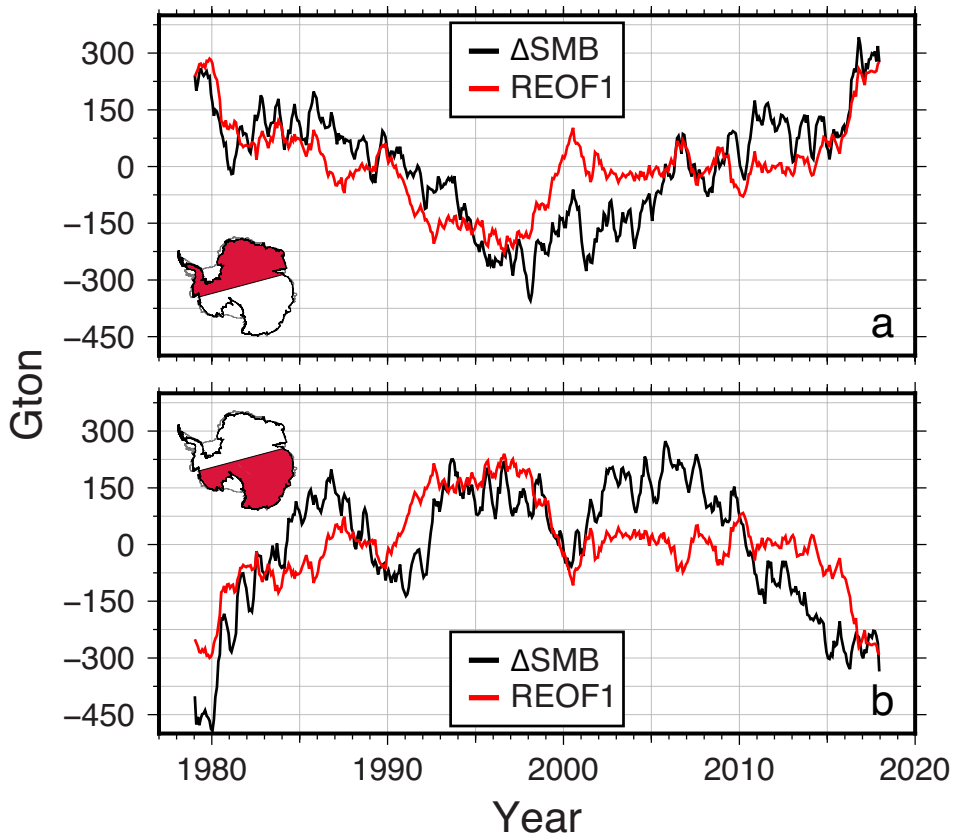
**Figure 3.5.** Prediction of  $\Delta$ SMB modulated by  $\Delta$ SAM using regression analysis.

Figure 3.6 shows total  $\Delta\text{SMB}$  (black) from ERA5 and reconstructed  $\Delta\text{SMB}$  modulated by SAM from the first REOF mode (red) over the two AIS regions considering the bi-polar pattern in Figure 3.4a. Black ( $\Delta\text{SMB}$ ) and red (reconstructed  $\Delta\text{SMB}$  from REOF1) show similar multi-decadal variations in both regions. The acceleration rate of  $\Delta\text{SMB}$  shown in the top panel is  $2.1\pm 0.1\text{Gton yr}^{-2}$ , and that of  $\Delta\text{SMB}$  affected by SAM is  $1.5\pm 0.1\text{Gton yr}^{-2}$ , which explains 72% of the multi-decadal variability. Similarly, in the region with the negative acceleration (bottom panel), 67% of the acceleration ( $-1.6\pm 0.1\text{Gton yr}^{-2}$  out of  $-2.4\pm 0.2\text{Gton yr}^{-2}$ ) is explained by SAM. This shows that there are large inter-annual and longer SMB variations over AIS, and among them, multi-decadal variations are affected by SAM.

### 3.4. Observation of AIS SMB

ERA5 model predictions of SMB variations can be validated using space and in-situ observations. ERA5 SMB predictions for 1979-2000 show pronounced multi-decadal ice mass loss acceleration of  $-5.7\pm 0.9\text{Gton yr}^{-2}$  (Figure 3.2) for the entire AIS. Similar evidence has been found in the ice core records (Medley & Thomas, 2018). A precipitation decrease since 1979 has been found in dozens of ice-cores collected throughout Antarctica (Thomas et al., 2017); AIS SMB acceleration due to the 1979-2000 precipitation decrease was  $-2.7\pm 3.8\text{Gton yr}^{-2}$ .

Satellite gravimetry (GRACE) observations of monthly surface mass change from April 2002 to June 2017, can be directly compared with model-based AIS SMB estimates. The previous study (Seo et al., 2015) compared GRACE data with ERA-Interim SMB over the period 2003-2013. Here we undertake a similar comparison, now using ERA5 from January 2003 to June 2017, together with CSR mascon solutions (Save et al., 2016). Similar to Figure 3.2a, linear trends from GRACE AIS mass change ( $\Delta\text{M}$ ) was removed, and the resulting time series is in Figure 3.7a.  $\Delta\text{M}$  shows higher frequency variability than  $\Delta\text{SMB}$ , due to GRACE noise and possibly errors in atmospheric pressure corrections (Seo et al., 2015). The acceleration rate in



**Figure 3.6.** Comparison of  $\Delta\text{SMB}$  (black) and reconstructed  $\Delta\text{SMB}$  (red) for the first REOF mode over the Pacific Sector (a) and Atlantic-Indian Sector (b).

$\Delta M$  ( $-8.6 \pm 2.1$  Gton  $\text{yr}^{-2}$ ) is also higher than that of  $\Delta \text{SMB}$  ( $-5.1 \pm 1.9$  Gton  $\text{yr}^{-2}$ ). This is likely because  $\Delta M$  includes both  $\Delta D$  (D after linear trend removal) and  $\Delta \text{SMB}$ . Satellite remote sensing has shown that acceleration due to increasing D throughout Antarctica is about  $-7.0$  Gton  $\text{yr}^{-2}$  (Rignot et al., 2019). After subtracting  $\Delta D$  from  $\Delta M$ , a GRACE value for  $\Delta \text{SMB}$  is obtained. This observation ( $\Delta M - \Delta D$ ) is about  $-1.6$  Gton  $\text{yr}^{-2}$ , much smaller than the ERA5 estimate of  $\Delta \text{SMB}$ . The disagreement is possibly due to atmospheric pressure error. In an earlier GRACE solution (CSR RL05), there was an apparent ice mass positive acceleration (Kim et al., 2016; Seo et al., 2015) associated with mis-modeled barometric pressure over AIS. CSR mascon solutions are also likely to suffer from apparent ice mass positive acceleration due to barometric pressure errors, as in previous GRACE data.

Because the synoptic scale of barometric pressure is distinct from relatively smaller spatial scale of ice discharge and SMB, the pressure error can be estimated by Empirical Orthogonal Function (EOF) analysis. For the correction of the barometric pressure error in  $\Delta M$ , EOF analysis was applied to the difference between  $\Delta M$  and  $\Delta \text{SMB}$ , as in the previous study (Seo et al., 2015). Before EOF analysis, both products are smoothed by a 600km Gaussian spatial filter to suppress artifacts due to differences in spatial resolution.

Figure 3.8 shows spatial patterns and their principal components (PC) of the three leading EOF modes. As in the previous study (Seo et al., 2015), mass loss acceleration signals appear over West Antarctica and the Antarctic Peninsula in the second mode. These are associated with  $\Delta D$ . In the third mode, a similar signal associated with  $\Delta D$  is observed around Totten glacier (Velicogna et al., 2014; Williams et al., 2014). Larger spatial patterns in the second and third modes compared to major glacier outlets in AIS are due to the 600km Gaussian smoothing. On the other hand, the first mode shows a spatial pattern with a single sign throughout Antarctica. Barometric pressure is known to have such a continent-wide synoptic spatial scale. We conclude that the continental scale first mode is likely associated with errors in barometric pressure. The first mode is subtracted from  $\Delta M$

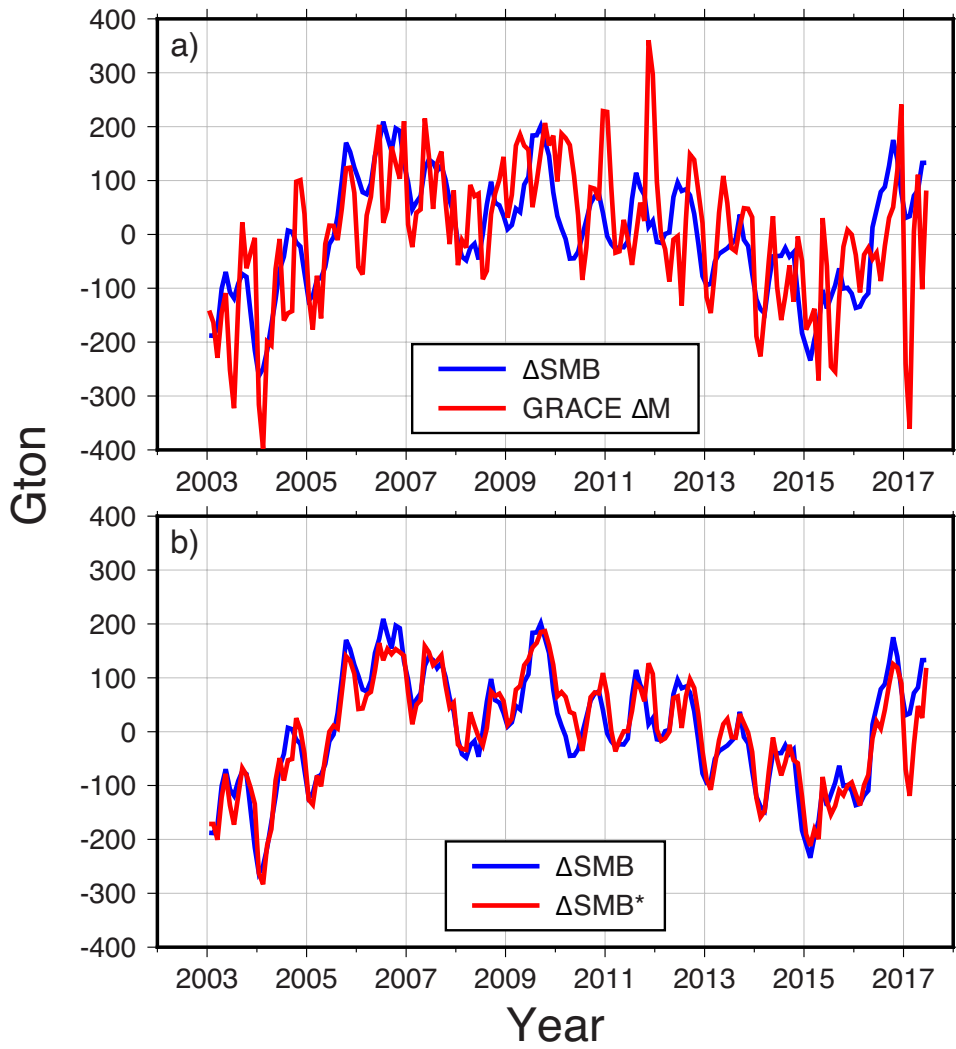


**Figure 3.7.** (a) Comparison between  $\Delta\text{SMB}$  (blue) and GRACE mass estimates  $\Delta\text{M}$  (red). (b) Similar to (a) but  $\Delta\text{SMB}^*$  is the estimated  $\Delta\text{SMB}$  from  $\Delta\text{M}$  after ice discharge and barometric pressure error corrections.

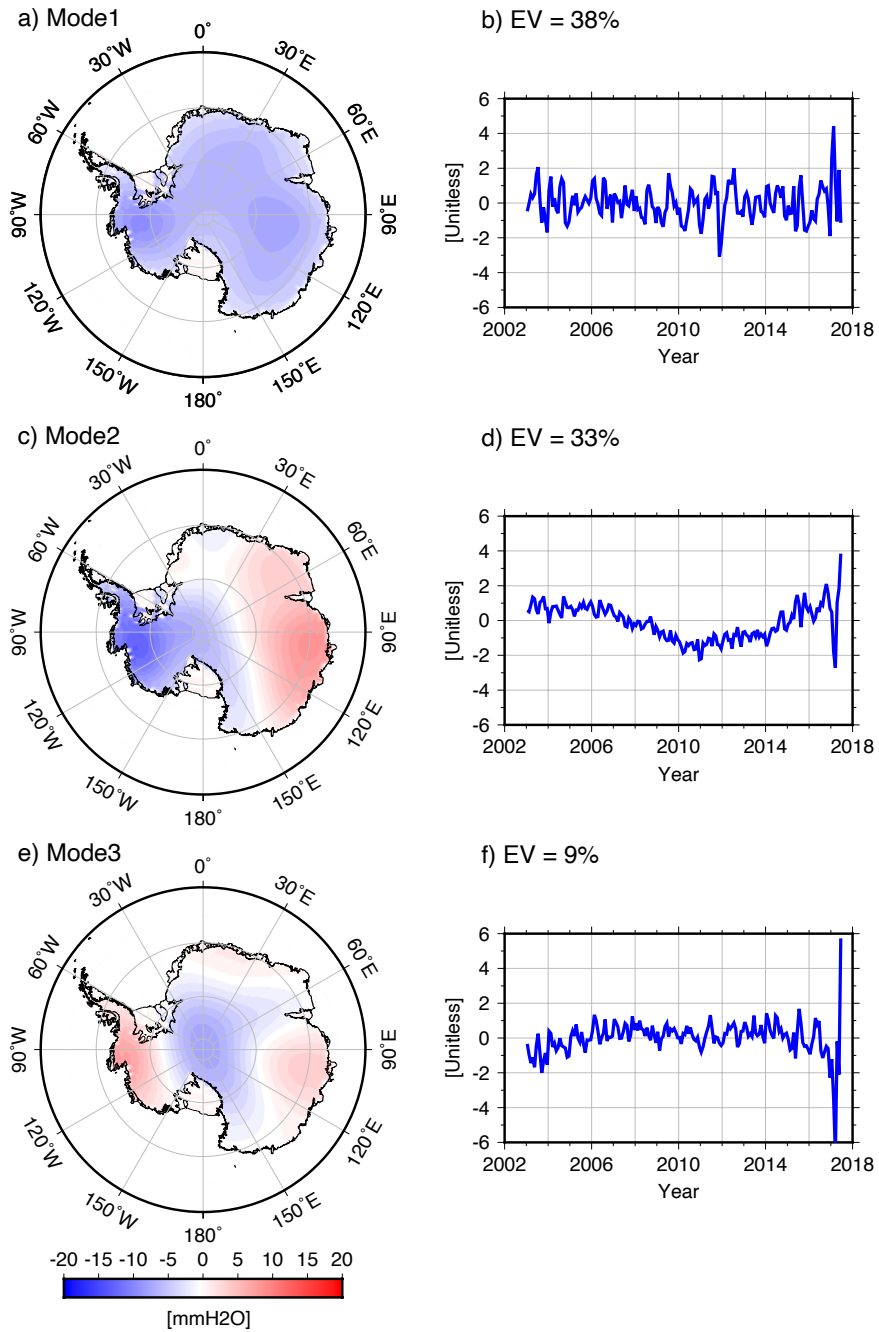


**Figure 3.8.** Spatial patterns (a, c, e) and their PCs (b, d, f) of leading three EOF modes calculated from  $\Delta M - \Delta SMB$ .

to correct this error.

$\Delta$ SMB based on GRACE observations ( $\Delta$ SMB\*) can be estimated after subtracting discharge acceleration rate and correcting for barometric pressure error. This  $\Delta$ SMB\* (from GRACE) and the ERA5 estimate of  $\Delta$ SMB are shown in Figure 3.7b. They agree well at inter-annual and longer periods, confirming the problem with barometric pressure in GRACE estimates, and more importantly indicating that  $\Delta$ SMB prediction from numerical models reasonably depicts AIS SMB variations.

### **3.5 Implications of SMB to present-day ice mass loss in AIS**

Recent efforts to understand AIS ice mass change and effects on sea level rise are largely based on satellite geodetic observations (Rignot et al., 2019; Schröder et al., 2019; Velicogna et al., 2014). We can use those observations to examine AIS mass loss associated with ice dynamics, which reflects processes such as ocean circulation, basal melting and grounding line migration (Dutrieux et al., 2014; Pritchard et al., 2012). Ice-dynamic variation time scales are likely much longer than those of SMB, and thus the current state is important in projecting future AIS mass loss and resulting sea level rise. Ice discharge (D), as a measure of ice dynamics, can be estimated from the difference between ice mass change and SMB.

A comprehensive AIS mass change estimate using multiple satellite geodetic observations and varied processing schemes was examined in IMBIE2 (Shepherd et al., 2018). The black line in Figure 3.9a shows that IMBIE2 AIS mass (M) loss has abruptly increased since 2007; negative trends are  $-47 \pm 1$  Gton  $\text{yr}^{-1}$  during 1992-2006 and  $-194 \pm 4$  Gton  $\text{yr}^{-1}$  during 2007-2017. The detrended IMBIE2 AIS mass change ( $\Delta$ M) in Figure 3.9b (black line) can be compared with ERA5  $\Delta$ SMB variations (blue line). Both  $\Delta$ M and  $\Delta$ SMB are obtained after removing linear trends in M (from IMBIE2) and SMB (from ERA5) during 1992-2017, respectively. The long-term  $\Delta$ SMB variation (blue line) is large enough to be comparable to the detrended

IMBIE2 AIS mass change ( $\Delta M$ ). Subtracting the  $\Delta \text{SMB}$  (blue) from  $\Delta M$  (black), we estimate AIS mass change associated with ice discharge,  $\Delta D$  (red), with the assumption that the contribution of inland meltwater to  $\Delta M$  is negligible (Seo et al., 2015). A thin red line shows a parabolic fit to  $\Delta D$  corresponding to an acceleration of  $-8.7 \pm 0.3 \text{ Gton yr}^{-2}$ . This estimated acceleration rate with small confidence interval indicates that since 1992, AIS ice discharge has accelerated at a steady rate, rather than abruptly. The sense of the sign is that ice discharge increases every year about 8.7 Gton. We conclude that the abrupt ice mass loss in 2007 (black line in Figure 3.9a) is a combined effect of  $\Delta D$  and  $\Delta \text{SMB}$ . Over the period 1993 to 2006, SMB mitigates ice mass loss acceleration due to  $D$ , and after that, SMB adds to acceleration in  $D$ , leading to an apparent abrupt increase in 2007. A similar interpretation can be found in ERA5 annual precipitation rate in Antarctica showing an increasing trend from 1994 to 2005 and a decreasing trend from 2006 to 2014 (Figure 3.10). The timing of trend change in precipitation rate (in 2005) is different from that of  $\Delta \text{SMB}$  (in 2007) because  $\Delta \text{SMB}$  is the time-integration of precipitation rate.

IMBIE2 reported that the trend in Antarctic ice mass loss during 2007-2017 has abruptly increased by  $\sim 147 \text{ Gton yr}^{-1}$  (which is equivalent to 0.41 mm/yr in global sea level change) compared to that during 1992-2006 (i.e., from  $-47 \text{ Gton yr}^{-1}$  during 1992-2006 to  $-194 \text{ Gton yr}^{-1}$  during 2007-2017). In this study, it is found that  $\sim 39 \text{ Gton yr}^{-1}$  (about 27%, or global sea level change of  $0.11 \text{ mm yr}^{-1}$ ) out of the  $147 \text{ Gton yr}^{-1}$  is attributed to SMB variation. Such a SMB effect is more significant in the West AIS, showing about 41% of the increase of ice mass loss between the two epochs (Figure 3.9c and 3.9d).

### 3.6 Conclusion

The long-term AIS SMB (accumulated precipitation) variations for 1979-2017 was examined using precipitation fields from the ERA5 reanalysis. Even though AIS precipitation rates do not exhibit a significant trend, SMB shows strong inter-annual

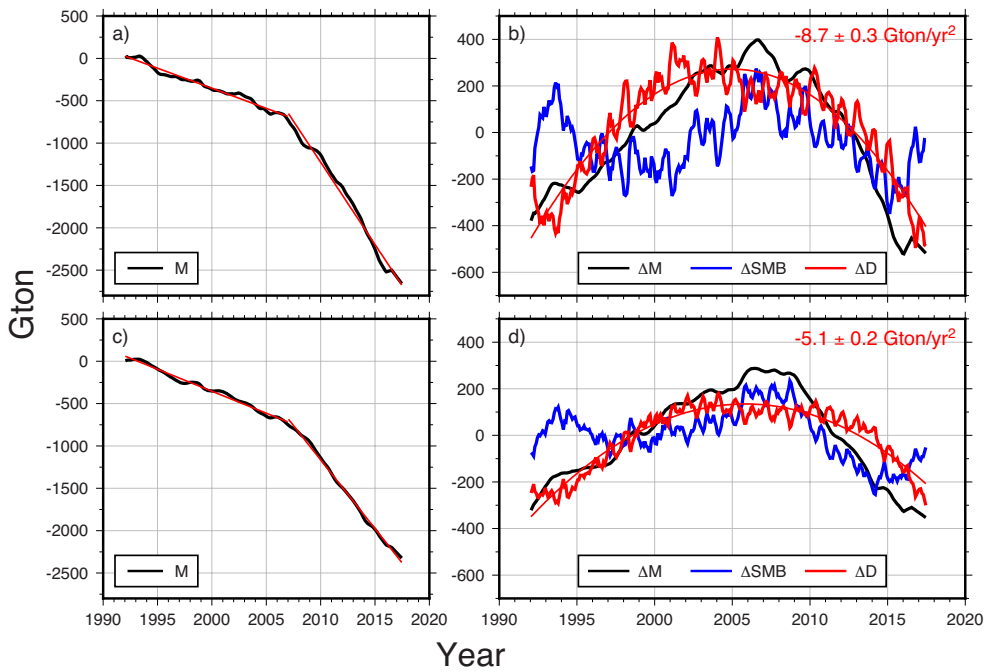


**Figure 3.9.** (a) AIS ice mass change from IMBIE2 estimates (black). Red lines represent linear trend fits before and after 2007. (b) Detrended variability of ice mass  $\Delta M$  (black),  $\Delta SMB$  (blue) and  $\Delta D$  (red). (c) and (d) are similar to (a) and (b) except for West Antarctica.

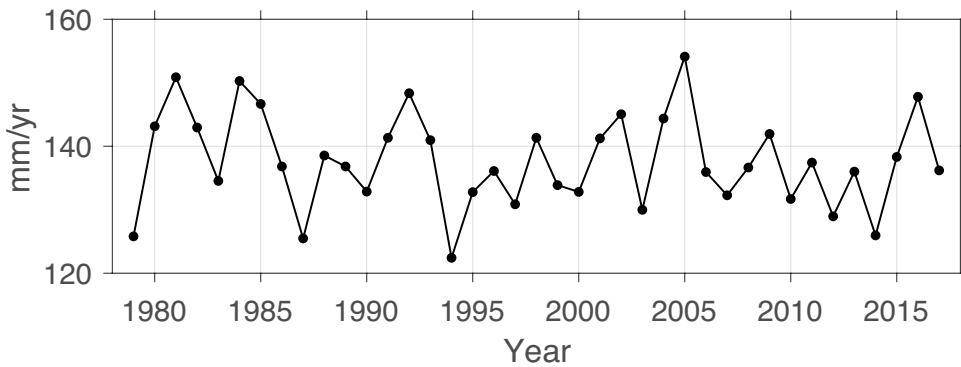


**Figure 3.10.** Changes in Antarctic annual mean precipitation (1979-2017) from ERA5 reanalysis.

and multi-decadal variations. This study found that multi-decadal SMB variations are related to SAM. AIS SMB modulated by SAM shows a distinct bi-polar pattern with negative acceleration in the Pacific Sector and positive acceleration in Atlantic and Indian Sectors. Model predictions of SMB variations are observed by satellite geodetic observation like GRACE. After correcting for SMB, a steady acceleration of ice discharge of  $-8.7 \pm 0.3$  Gton  $\text{yr}^{-2}$  was found for the period 1992-2017. The apparent abrupt change in 2007 is not associated with a change in ice dynamics but instead with SMB variations mostly in the West AIS.

# Chapter 4. Estimation of high-resolution Antarctic ice mass balance using satellite gravimetry and altimetry

## 4.1. Introduction

Mass loss from the Antarctic Ice Sheet (AIS) is one of the major contributors to global sea-level rise. From 1992 to 2017, loss of  $\sim 109$  Gton  $\text{yr}^{-1}$ , led to about  $0.3$  mm  $\text{yr}^{-1}$  in global sea-level rise (Shepherd et al., 2018). At the same rate, AIS mass loss would cause about  $23$  cm in global sea-level rise by the end of this century.

Most AIS mass loss is associated with glaciers in the Amundsen and Bellingshausen Sea Embayments in West Antarctica. Ice mass increases are found in Dronning Maud Land in East Antarctica and the Kamb Ice Stream in West Antarctica (Rignot et al., 2019). Mass loss or gain at individual glaciers is associated with varied processes in the atmosphere (e.g., Boening et al. (2012)), oceans (e.g., Dutrieux et al. (2014)), and in subglacial hydrology (e.g., Alley et al. (1994)). The complexity and variety of contributing mechanisms have hindered robust projections of future AIS mass changes and corresponding sea-level variations (Kopp et al., 2017). Sparse observations of glacier-scale ice mass balance are also a limitation.

The GRACE mission has provided observations of AIS mass change for nearly two decades (Tapley et al., 2019), but with poor spatial resolution (a few hundred km). GRACE spatial resolution is limited by spacecraft altitude and intersatellite distance, spatial filtering required to suppress noise (Wahr et al., 1998), and correlation error (Swenson & Wahr, 2006). These limitations result in smooth estimates containing spatial leakage error. An algorithm called forward modeling (FM) (e.g., Chen et al., (2015); Chen et al., (2007); Kim et al., (2019)) was developed to correct GRACE estimates for leakage error. FM iteratively adjusts an initial mass field until an updated field, when smoothed, agrees with low resolution processed GRACE data. Another algorithm, constrained linear deconvolution (CLD), can also

address the leakage problem (Seo et al., 2020) using well-known techniques associated with regularized linear inversion. Both FM and CLD have been used to suppress leakage error from land to oceans, but not leakage among terrestrial river or glacier basins (Seo et al., 2020).

Satellite radar and laser altimetry are able to observe ice surface elevation changes. While offering much finer spatial resolution than GRACE (Rémy & Parouty, 2009) there are limitations related to surface topography roughness, for example, in the Antarctic Peninsula (Shepherd et al., 2019). In addition, orbital inclinations may prevent observations at high latitudes. However, multi-mission altimetry data sets (Schröder et al., 2019) should provide improved results with higher spatial resolution to complement GRACE observations. In this study we present a revised application of CLD to combine high resolution altimetry observations with conventional GRACE estimates to obtain high resolution AIS mass changes, and compare the results with independent Input-Output budget estimates of glacial scale mass variations.

## **4.2. Data**

### **4.2.1 GRACE gravity data**

GRACE gravity data are provided as spherical harmonic (SH) coefficients at monthly intervals from April 2002 to July 2017. These are converted to surface mass loads at grid points. We estimate surface mass loads over the AIS using Release-06 GRACE solutions provided by the Center for Space Research (CSR). Degree-1 and degree-2, order-0 SH coefficients were replaced by estimates provided by the GRACE project as supplementary datasets in GRACE Technical Notes 13 (Landerer, 2019) and Technical Note 14 (Loomis et al., 2019), respectively. The north-south stripes and random noise were removed by a decorrelation filter (Swenson & Wahr, 2006) and 400km Gaussian smoothing (Wahr et al., 1998). Glacial isostatic adjustment (GIA) was removed using the average of multiple models (Caron & Ivins, 2019; Peltier et al., 2018; Purcell et al., 2016; Whitehouse et al., 2012). The resulting

GRACE data include mass changes over land and oceans. Total ocean mass variation is the negative of total land mass variation, and the spatial distribution of the ocean mass is adjusted by self-attraction and loading (SAL) effect (Adhikari et al., 2019; Jeon et al., 2018). We estimated the ocean mass signals using terrestrial mass loads obtained from conventional FM (Kim et al., 2019). The estimated ocean mass signal (after 400km Gaussian smoothing) was removed from the reduced GRACE data, leaving a residual due only to variations on land. The importance of this is described in section 4.2. Figure 4.1a shows a linear trend map of AIS mass change for 2003-2016 from the residual GRACE data. Trend values were sampled on a polar-stereographic 27 km grid to compare with altimetry data. Figure 4.1a shows that low GRACE spatial resolution causes large rates in West Antarctica to leak into the oceans. Spatial leakage would occur throughout Antarctica, between basins and from land to oceans, preventing an analysis of glacier-scale changes using GRACE data alone.

#### 4.2.2. Satellite altimetry data

We used monthly altimetry-based surface elevation changes from Schröder et al. (2019). These are merged observations from multi-mission altimeters at 10km grid intervals from 1978 to 2017. We used these altimeter data for the 2003-2016 period of the GRACE data. The merged observations combine ENVISAT (2002-2012), ICESat (2003-2009), and Cryosat-2 (2010-present) data. ENVISAT and ICESat are limited to latitudes below 81°S and 86°S, respectively. Cryosat-2 observes to 88°S. ICESat operated intermittently several times per year due to hardware limitations (Schutz et al., 2005). We used temporal interpolation to replace missing observations from 81°S - 86°S, creating a potential source of uncertainty.

Changes in surface elevations observed by satellite altimetry,  $H_s$ , include three different components:

$$H_s(t) = H_i(t) + H_c(t) + H_f(t) \quad (4.1)$$

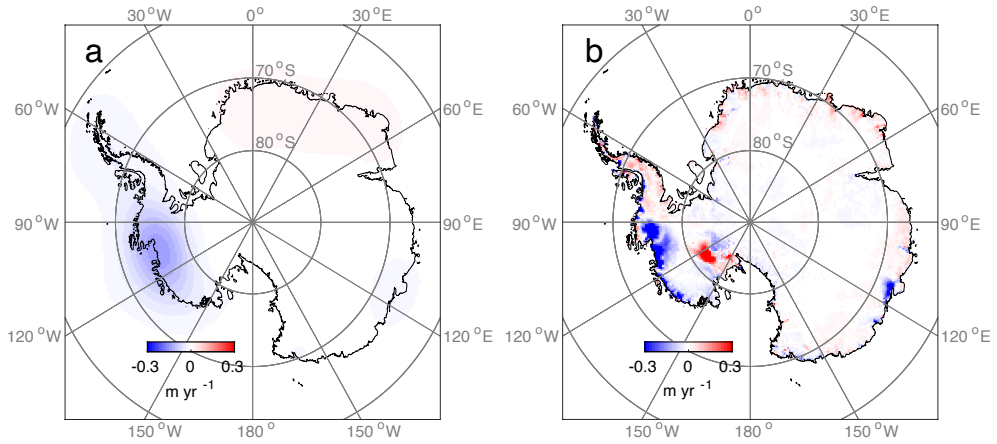


**Figure 4.1.** Linear trend maps of Antarctic ice mass change observed by GRACE (a) and satellite altimetry (b).

$H_i$  is elevation change due to ice dynamics, with decadal or longer time-scale variability (Rignot et al., 2019; Seo et al., 2015).  $H_c$  is crustal uplift rate associated with glacial isostatic adjustment (GIA) which should be linear in time.  $H_f$  denotes firn thickness changes that depend primarily on surface air temperature and surface mass balance (SMB) (Ligtenberg et al., 2011) varying at sub-annual to inter-annual or longer time-scales. Because AIS ice mass balance is determined by ice dynamics and surface mass balance (Lenaerts et al., 2019), changes in AIS ice mass load,  $M_A$ , include the two effects:

$$M_A(t) = \rho_i H_i(t) + SMB(t) = \rho_i (H_s(t) - H_c(t) - H_f(t)) + SMB(t) \quad (4.2)$$

in which  $\rho_i$  is the density of ice ( $=917 \text{ kg m}^{-3}$ ). To estimate  $H_i$  from  $H_s$ , it is necessary to remove effects of  $H_c$  and  $H_f$ . We used numerical model output for such corrections. Surface elevation changes due to GIA,  $H_c$ , were estimated using the same models as in GRACE processing (section 4.2.1). Firn thickness change,  $H_f$ , was obtained from IMAU-FDM (Ligtenberg et al., 2011), an empirical model forced by RACMO2.3p2 (Van Wessem et al., 2014). Compared to  $H_s$ , sub-annual to inter-annual variability in  $H_i$  is suppressed after removing  $H_f$  from  $H_s$ , so uncertainty from temporal interpolation of altimetry data (described above) is likely minimal. Remaining uncertainties associated with altimetry observations and firn thickness correction should be further suppressed when GRACE and altimetry data are combined in section 4.3.  $SMB(t)$  was taken from RACMO2.3p2, the same model used for  $H_f$ .

Altimetry ice mass change was estimated on a 27 km grid, considering spatial resolution of SMB and firn thickness models (Ligtenberg et al., 2011; Van Wessem et al., 2014). Figure 4.1b shows that the linear trend map of altimeter ice mass changes has higher spatial resolution than the GRACE map in Figure 4.1a. In West Antarctica, losses in Figure 4.1b are clearly associated with Pine Island and

Thwaite Glaciers. A positive mass rate for Siple Coast Ice Streams is not evident in Figure 4.1a, probably due to spatial leakage from a region with negative rates at higher latitudes. Figure 4.1b shows negative rates near Totten Glacier in East Antarctica while, as a result of low spatial resolution, lower rates in Figure 1b become distributed over a larger area around the glacier in Figure 4.1a.

The satellite altimetry map (Figure 4.1b) includes some regions with questionable trends. An example is a positive rate at the northern tip of the Antarctic Peninsula. Satellite imagery has shown mass loss in this area due to increased ice flow near Larsen A and B Ice Shelves, and West Graham Land (Rignot, 2004; Rignot et al., 2019; Scambos et al., 2004), and negative GRACE rates in this region are in agreement (Figure 4.1a), albeit with a low spatial resolution. A positive rate in Figure 4.1b is likely associated with uncertainties in altimetry observations over a region of high topographic relief (Schröder et al., 2019; Shepherd et al., 2019). Similar problems would be expected in other areas.

## 4.3. Methods

### 4.3.1 Forward Modeling (FM) solution

The FM method (e.g., Chen et al., (2015); Chen et al., (2007)) corrects for spatial leakage of signals from land into the oceans, but does not improve spatial resolution of resulting mass signals on land. However, we obtain an FM solution in order to compare it with results from the modified CLD approach in next section.

Here, FM is used with much finer spatial resolution relative to earlier applications (Chen et al., 2015; Chen et al., 2007). Let  $M_G$  be a vector containing smooth GRACE surface mass load changes in a given month after GRACE data reduction described in section 4.2.1, on a 27 km polar-stereographic grid as adopted for the altimetry data. The FM algorithm aims to find a new mass distribution ( $M_N$ ) close to  $M_G$ , after Gaussian smoothing (400 km). The iterative scheme begins with an initial mass load,  $M_1$ .  $M_1$  is set to on-land values of  $M_G$  (Chen et al., 2015).

$$M_1 = L \circ M_G \quad (4.3)$$

in which  $L$  is the land function:

$$L(x) = \begin{cases} 1, & \text{if } x \text{ is on land or grounded ice} \\ 0, & \text{if } x \text{ is on floating ice or oceans} \end{cases} \quad (4.4)$$

where  $x$  is a geographical location on the polar-stereographic grid. The symbol “ $\circ$ ” denotes the Hadamard product.  $L(x)$  was obtained using ice surface morphology from MODIS optical images as part of the MOA2014 project (Scambos et al., 2007). To reduce computational effort, we confine calculations to ocean areas within 800 km of grounded ice of Antarctica. This is large enough to include leakage into the oceans found in  $M_G$  (Figure 4.2). This 800km buffer zone is also used with the CLD method below.

After the first iteration, a misfit ( $U_1$ ) between  $M_G$  and  $M_1$  over land was evaluated:

$$U_1 = L \circ (M_G - GM_1) \quad (4.5)$$

where multiplication by  $G$  approximates convolution associated with 400 km Gaussian smoothing (Seo et al., 2020). Using  $G$  allows us to implement smoothing directly on gridded data instead of using spherical harmonics.

We modified the smoothed surface mass load ( $M_1$ ) by adding the misfit ( $U_1$ ), giving the updated mass load,  $M_2 = M_1 + U_1$ . Proceeding to  $M_N$  after the  $N^{\text{th}}$  iteration

$$M_N = M_{N-1} + U_{N-1} \quad (4.6)$$

$$\text{where } U_{N-1} = L \circ (M_G - GM_{N-1}). \quad (4.7)$$

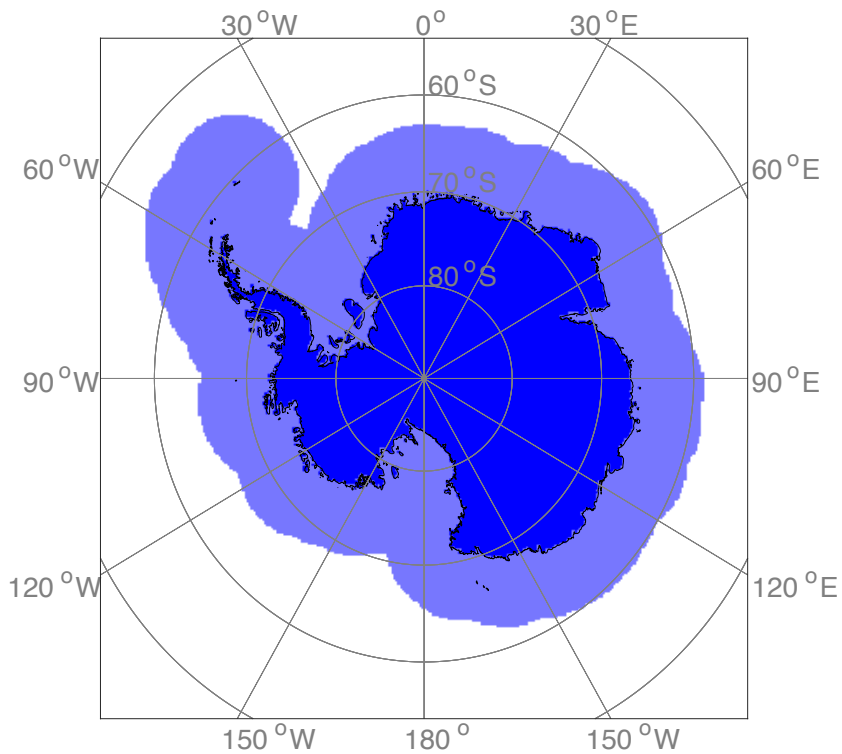


**Figure 4.2.** Spatial distributions of land (blue) and ocean (light blue) functions used in Equation (4.4). The land function is defined as the grounding line and island boundaries from the MOA2014 project (Scambos et al., 2007). The ocean function includes the 800km buffer zone from land boundaries.

The updated surface mass load after smoothing ( $GM_N$ ) converges to  $M_G$ . In this study, we ceased iteration when the sum of misfits ( $|\sum M_G - GM_N|$ ) over all land grid points was less than 0.1 Gton.

### 4.3.2 Joint estimation using constrained linear deconvolution

Our new method for combining GRACE and satellite altimetry data is a revised form of constrained linear deconvolution (CLD) (Seo et al., 2020). CLD corrects leakage (from land to oceans), using regularized least squares, but without iteration as in FM. Similar methods have been used to estimate surface mass distribution from gravitational potential (Forsberg et al., 2017) and to obtain smoothed mass field (Mu et al., 2017) from GRACE data.

We establish a linear relationship between mass loads to be estimated,  $\hat{m}$ , and smoothed mass loads,  $M_G$  from GRACE after 400 km Gaussian smoothing:

$$G\hat{m} = M_G + \epsilon \quad (4.8)$$

in which  $G$  is the Gaussian smoothing operator defined in section 4.3.1 and  $\epsilon$  is the misfit. We follow the procedures developed by Seo et al. (2020) to estimate  $\hat{m}$  and additionally use a priori mass loads,  $\langle m \rangle$ , obtained from altimetry observation. Including  $\langle m \rangle$ , Equation (4.8) yields:

$$G(\hat{m} - \langle m \rangle + \langle m \rangle) = M_G + \epsilon \quad (4.9)$$

which reduces to

$$G(\hat{m} - \langle m \rangle) = M_G - G\langle m \rangle + \epsilon \quad (4.10)$$

Equation (4.10) represents another linear relation between  $\hat{m} - \langle m \rangle$  and  $M_G - G\langle m \rangle$ , in place of  $\hat{m}$  and  $M_G$  in Equation (4.8). Typically,  $\hat{m} - \langle m \rangle$  in

Equation (4.10) can be estimated by generalized least squares:

$$\hat{m} - \langle m \rangle = (G^T P G)^{-1} G^T P (M_G - G \langle m \rangle) \quad (4.11)$$

in which  $P$  is a matrix whose diagonal elements are the inverse squares of GRACE's observational error (Section 4.3.3.1).  $\hat{m} - \langle m \rangle$  obtained in Equation (4.11), however, includes amplified noise because multiplication by  $(G^T P G)^{-1} G^T$  is equivalent to applying the inverse of a smoothing filter. To suppress the noise, a penalty that minimizes spatial gradients (Constable et al. 1987) is included in the cost function assuming that noise dominates higher spatial frequencies. A measure of spatial gradients (steepness) between the first surface mass load,  $\hat{m}_1$ , and others ( $\hat{m}_2, \hat{m}_3, \dots, \hat{m}_N$ ), is obtained by multiplying by the  $D_1$  matrix:

$$D_1 = \begin{bmatrix} -1/r_{12} & 1/r_{12} & 0 & \dots \\ -1/r_{13} & 0 & 1/r_{13} & \dots \\ \vdots & \vdots & \ddots & \dots \\ -1/r_{1N} & 0 & \dots & 1/r_{1N} \end{bmatrix} \quad (4.12)$$

in which  $r_{1n}$  ( $n = 2, 3, \dots, N$ ) is the distance between the first and  $n$ th mass load. Steepness between  $\hat{m}_1$  and ( $\hat{m}_2, \hat{m}_3, \dots, \hat{m}_N$ ) is  $D_1 \hat{m}$ . Similarly, the steepness between the  $k$ th mass load and all others is  $D_k \hat{m}$ . Considering all we define matrix  $D$  for total steepness:

$$W = \sum_{n=1}^N D_n^T D_n \quad (4.13)$$

Including the steepness penalty, we obtain the least square solutions

$$\hat{m} - \langle m \rangle = [(G^T P G) + \lambda W]^{-1} G^T P (M_G - G \langle m \rangle). \quad (4.14)$$

where  $\lambda$  is a regularization parameter. Equation (4.14) now yields a solution  $\hat{m}$ :

$$\hat{m} = \langle m \rangle + [(G^T P G) + \lambda W]^{-1} G^T P (M_G - G \langle m \rangle) \quad (4.15)$$

We additionally modified Equation (4.15) to suppress leakage from land to oceans with a constraint that ocean elements in  $\hat{m}$  are zeros. This constraint recovers land signals that have leaked to ocean grid points in  $M_G$ . This is valid because estimated ocean mass signals were removed to obtain residual GRACE data as explained in section 4.2.1. To realize this constraint, we use matrix  $H$  whose diagonal elements are ones for ocean elements and zeros for all others (Seo et al., 2020):

$$H \hat{m} = 0 \quad (4.16)$$

The land function,  $L$ , in Equation (4.4) was used to generate  $H$ .

Finally, by including Equation (4.16) in the cost function, we obtained two equations which must be solved simultaneously by combining them into the matrix form (see Chapter 3.10 in Menke (2012)):

$$\begin{bmatrix} \hat{m} \\ \hat{n} \end{bmatrix} = \begin{bmatrix} \langle m \rangle \\ 0 \end{bmatrix} + \begin{bmatrix} G^T P G + \lambda W & H^T \\ H & 0 \end{bmatrix}^{-1} \begin{bmatrix} G^T P (M_G - G \langle m \rangle) \\ h \end{bmatrix}. \quad (4.17)$$

The final solution of  $\hat{m}$  needs to be estimated by adjusting the regularization parameter,  $\lambda$ .  $\lambda$  can be obtained in either an empirical or statistical way (Mu et al., 2017; Xu, 1998). We first used ‘‘L-curve’’, which is one of the most widely used methods to estimate  $\lambda$ . The L-curve is a graph of the solution length and the size of prediction error obtained by different value of  $\lambda$ . By adjusting  $\lambda$ , ones can decide the optimal trade-off value that minimizes both quantities. Figure 4.3 shows the L-curve corresponding to Equation (4.17). The x- and y- axis represent the size of the prediction error and the solution, respectively. The graph depicts an L-shaped curve with smooth corners, indicating that an appropriate solution still needs to be chosen

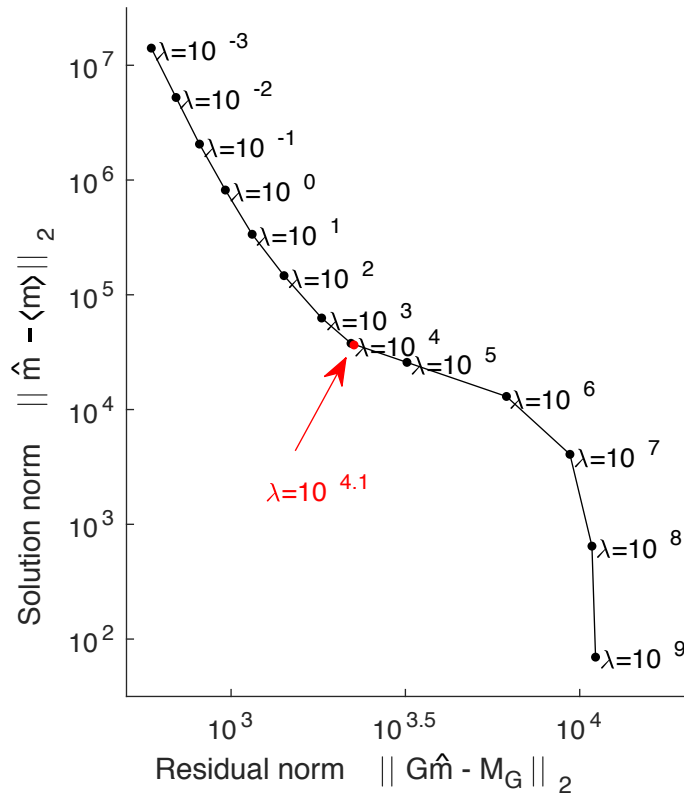


**Figure 4.3.** L-curve obtained by varying the regularization factor,  $\lambda$ . The red dot shows the position of  $\lambda = 10^{4.1}$  on the graph.

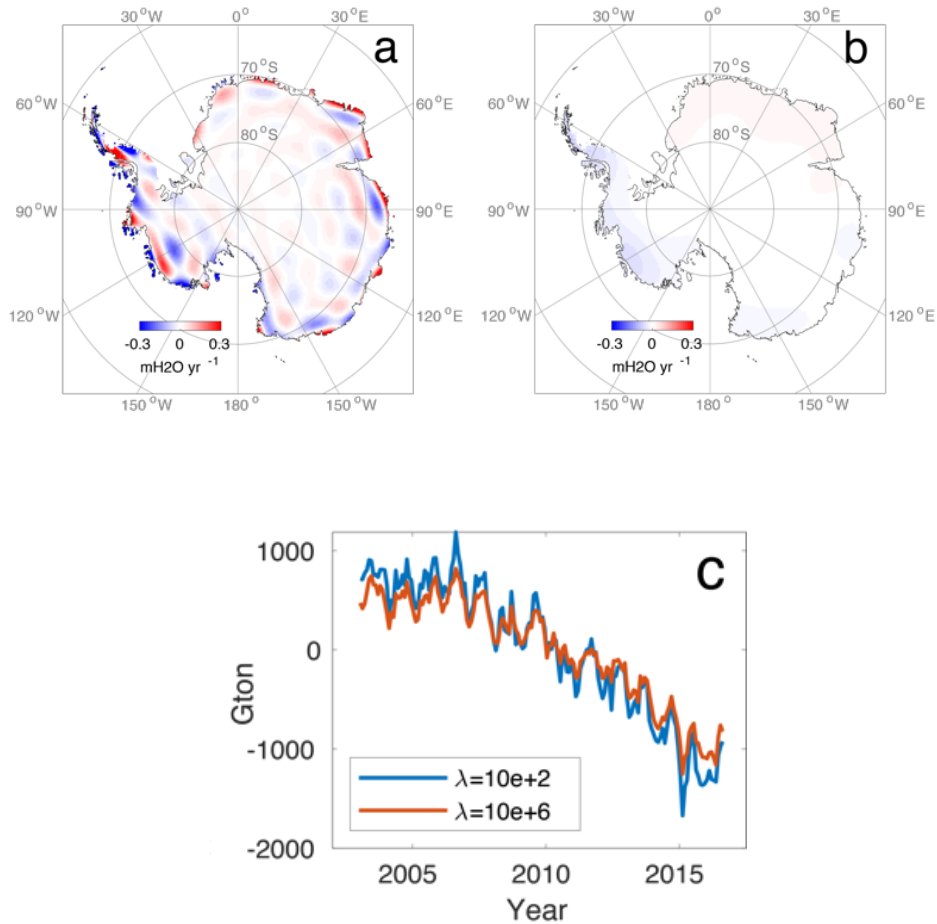
empirically between  $\lambda = 10^2 \sim 10^6$ .

Figure 4.4a and b show linear trend maps of ice mass loads estimated by Equation (4.17) when  $\lambda$  are  $10^2$  and  $10^6$ , respectively. In both cases, we removed the effect of a-priori mass loads to highlight the difference between two. If  $\lambda$  is small ( $\lambda = 10^2$ ), stronger signals are observed with evident errors remained in the spatial pattern of the estimated mass loads. On the other hand, spatial patterns of mass loads estimated by larger  $\lambda$  ( $\lambda = 10^6$ ) are over-blurred, making it difficult to identify the small spatial-scale mass variability. There is also a slight difference in the time-series of mass changes obtained by each calculation (Figure 4.4c). The time-series estimated using larger  $\lambda$  ( $\lambda = 10^6$ ) shows smaller variability compared to the time-series estimated based on smaller  $\lambda$  ( $\lambda = 10^2$ ), indicating that the spatial leakage problem of GRACE data is not sufficiently resolved when using a larger  $\lambda$ .

The L-curve with smooth corner provides a range of appropriate regularization factor, but cannot specify an exact value. Comparing  $\lambda$  estimated by other methods may help to determine the value. For example, we estimated leakage-corrected mass loads by FM in Section 4.3.1. By trial and error, we can obtain a regularization factor that minimizes root-mean-square (RMS) for the difference between forward modelled mass loads and estimated (from inversion) mass loads. The obtained  $\lambda$  here is  $10^{4.1}$ , which is also located at the corner of the L-curve (the red dot in Figure 4.3). Given the fact that  $\lambda$  should be chosen empirically, we estimate the CLD solution using  $\lambda = 10^{4.1}$  from the next chapter.

### 4.3.3. Uncertainties

Antarctic ice mass changes from GRACE and satellite altimetry include uncertainties caused by observational error and inaccurate model correction. And these uncertainties would propagate into FM and CLD estimates, respectively. In the following subsections, we introduce uncertainty estimation methods for GRACE, FM, altimetry, and CLD, respectively.



**Figure 4.4.** a, b: Linear trend maps of Antarctic ice mass loads estimated by different value of  $\lambda$  (a:  $\lambda = 10^2$ , b:  $\lambda = 10^6$ ). For clarity, linear trends of *a-priori* mass load were removed from each spatial pattern. c: Time-series of Antarctic ice mass change in each case.

#### 4.3.3.1. Uncertainty of GRACE observation

Together with geoid SH coefficients, the GRACE data center provides SH coefficients of its standard deviations. Using these data, we estimate the observational error of GRACE by Monte-Carlo simulation. We first calculated the average of monthly standard deviations from 2003 to 2016, which are denoted by  $\tilde{C}_{lm}$  and  $\tilde{S}_{lm}$ . Generated are 1000 random sets of SH coefficients with zero means and standard deviations of  $\tilde{C}_{lm}$  and  $\tilde{S}_{lm}$ . Each set of SHs was converted into surface mass densities ( $\varepsilon_G^1, \varepsilon_G^2, \dots, \varepsilon_G^{1000}$ ) after 400km Gaussian smoothing. Finally, we calculated the standard deviation of surface mass densities at each grid point and considered it as an observational error of GRACE data. Figure 4.5a shows the global error distribution, and its Antarctic part is highlighted in Figure 4.5b.

#### 4.3.3.2. Uncertainty of FM solution

The uncertainty of FM solution caused by GRACE's error was calculated from random errors obtained from the section 4.3.3.1. We added each set of random errors ( $\varepsilon_G^1, \varepsilon_G^2, \dots, \varepsilon_G^{1000}$ ) to the observed surface mass density ( $M_G$ ) at a month, assuming that the  $M_G$  is the signal. Then, we obtained FM solutions using  $M_G$  plus random errors. Finally, the standard deviation of FM solutions was defined as its uncertainty. Figure 4.6 shows the spatial distribution of uncertainties. The uncertainty increases particularly along coasts. This is because FM restores both signals and errors from oceans to land. The total error over the entire AIS is still very small, about 3.5 Gton.

Another error source in FM solution is residual GIA effect due to the uncertainty of GIA model used in GRACE data reduction. We empirically estimate the uncertainty of the GIA effect using four GIA models (Caron & Ivins, 2019; Peltier et al., 2018; Purcell et al., 2016; Whitehouse et al., 2012). We corrected GRACE data using each of the GIA models and obtained four different FM solutions. Then, the maximum difference of linear trends in ice mass change calculated by four FM solutions was considered the GIA error in FM solutions. The estimated error

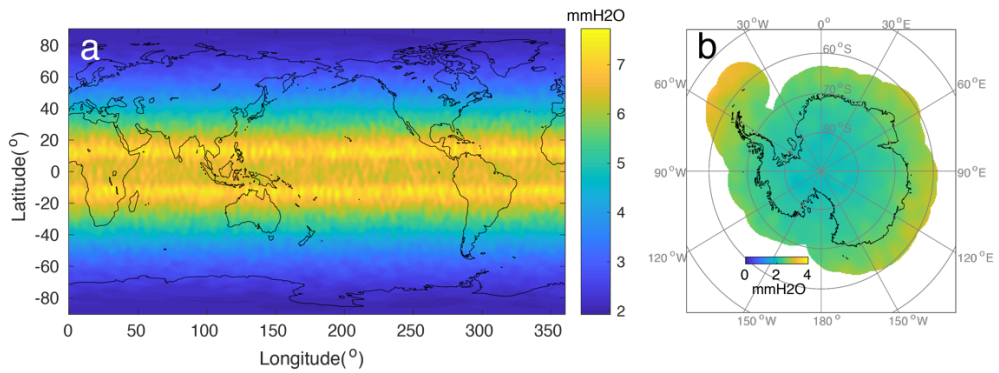


**Figure 4.5.** Spatial distribution of GRACE errors estimated around the world (a) and in Antarctica (b).

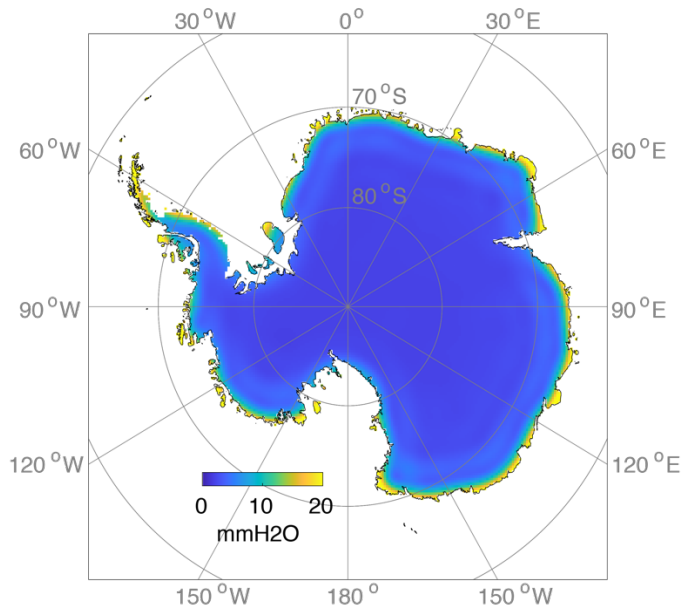


**Figure 4.6.** Spatial distribution of FM solution error.

over the AIS was about 26.3 Gton yr<sup>-1</sup>, confirming that GRACE’s Antarctic observation is largely dependent on GIA models (Whitehouse et al., 2019). The total error of the ice mass change from the FM solution was estimated by summing up random error and GIA error.

#### 4.3.3.3. Uncertainty of altimetry-based mass loads

The uncertainty of altimetry-based ice mass change was classified into observational error (i.e., random error), firm thickness error and GIA model error. Regarding the error of altimetry observation, we used the uncertainty data from Schröder et al. (2019), which is provided along with the surface elevation change data. We first calculated the average uncertainty of the elevation anomalies at each grid point over the total study period (2003-2016) and defined it as  $\sigma_s$ . During the volume-mass unit conversion (equation (4.2)), the uncertainty of the mass loads at each grid point ( $\sigma_{s\_mass}$ ) was calculated as follows:

$$\sigma_{s\_mass} = \rho_i \sigma_s \cdot \quad (4.18)$$

Because observational errors of satellite altimetry ( $\sigma_s$ ) is spatially correlated within a radius of 50km (Schröder et al., 2019), we modified the error to reflect such noise characteristics. First, we generated 1000 random errors with zero means and standard deviations of  $\sigma_{s\_mass}$  at each grid pixel. Because the correlated noise would be amplified when summing up, it is necessary to apply a scale factor to the errors. Given the spatial resolution (27km) of our data processing, the area of a circle with a radius of 50km corresponds to 10.8 grid pixels of our data. Therefore, we generated 1000 random errors with zero means and standard deviations of  $\sigma_{s\_mass}$  at each grid pixel and multiplied the random errors by scale factor  $\sqrt{10.8}$ . The estimated 1000 sets of noises,  $(\varepsilon_S^1, \varepsilon_S^2, \dots, \varepsilon_S^{1000})$ , are added into the mass loads in a given month, thereby obtaining  $m_S^1, m_S^2, \dots, m_S^{1000}$ . The total uncertainty over the entire AIS estimated in this way is about 178.4 Gton. The spatial distribution of the modified

$\sigma_{s\_mass}$  is shown in Figure 4.7a.

Regarding the uncertainty of the firm thickness model, we used the uncertainty data ( $\sigma_f$ ) from Ligtenberg et al. (2011), provided along with the model data. The contribution of model uncertainty to altimetry-based mass loads was calculated as follows:

$$\sigma_{f\_mass} = \rho_i \sigma_f. \quad (4.19)$$

Figure 4.7b shows the spatial map of  $\sigma_{f\_mass}$ . We also generated 1000 sets of random numbers with zero means and standard deviations of  $\sigma_{f\_mass}$ , ( $\varepsilon_f^1, \varepsilon_f^2, \dots, \varepsilon_f^{1000}$ ). Over the entire AIS, the uncertainty caused by the firm thickness model was estimated to be about 6.3 Gton.

The total random error at each grid pixel can be obtained by the 1000 sets of random errors generated above,

$$[\varepsilon_A^1, \varepsilon_A^2, \dots, \varepsilon_A^{1000}] = [\varepsilon_S^1, \varepsilon_S^2, \dots, \varepsilon_S^{1000}] + [\varepsilon_f^1, \varepsilon_f^2, \dots, \varepsilon_f^{1000}] \quad (4.20)$$

The spatial distribution of the standard deviations of ( $\varepsilon_A^1, \varepsilon_A^2, \dots, \varepsilon_A^{1000}$ ),  $\sigma_A$ , is shown in Figure 4.7c. The spatial patterns and amplitudes are similar to those of  $\sigma_{s\_mass}$ , indicating that most random errors are caused by altimetry data.

We also estimated the systematic errors induced by inaccurate GIA correction using a similar method to the previous section. We used four GIA models to convert the observed elevation changes to mass changes according to equation (4.2). Then we calculated the maximum difference in linear trends of estimated mass changes. The GIA error was about 8.6 Gton yr<sup>-1</sup> over Antarctica.

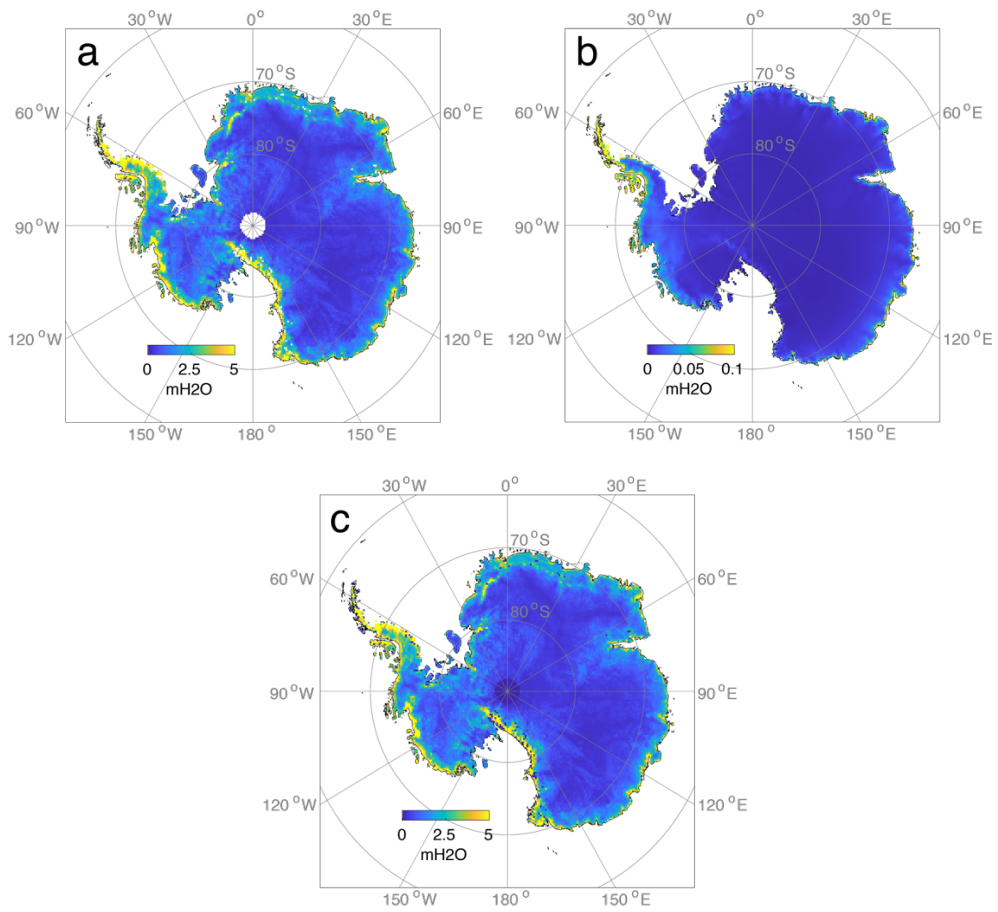


**Figure 4.7.** Spatial distribution of  $\sigma_{s\_mass}$  (a),  $\sigma_{f\_mass}$  (b), and  $\sigma_A$  (c).

#### 4.3.3.4. Uncertainty of CLD solution

The CLD solution ( $\hat{m}$ ) obtained by equation (4.17) is affected by both GRACE and altimetry errors. To estimate the error propagations to the CLD solution, we also used an empirical method by Monte-Carlo simulations as similarly performed in the previous sections. We added GRACE's random errors ( $\varepsilon_G^1, \varepsilon_G^2, \dots, \varepsilon_G^{1000}$ ) to  $M_G$  of a given month. Similarly,  $\langle m \rangle$  at the same month of  $M_G$  was contaminated by the random errors from altimetry ( $\varepsilon_A^1, \varepsilon_A^2, \dots, \varepsilon_A^{1000}$ ). Using contaminated mass loads of  $M_G$  and  $\langle m \rangle$ , we estimated 1000 different CLD solutions ( $\hat{m}_1, \hat{m}_2, \dots, \hat{m}_{1000}$ ) by equation (4.17). Finally, the standard deviation of the CLD solution was defined as its uncertainty. Figure 4.8 shows estimated uncertainties in each grid pixel.

The CLD error is much smaller than the altimetry error shown in Figure 4.7 due to error reduction in the linear deconvolution process. Altimetry observation,  $\langle m \rangle$ , includes both true variations of ice mass loads and errors in 27km spatial resolution. The error in  $\langle m \rangle$  is much larger than that in  $M_G$ , GRACE observation.  $M_G$  also includes the same true ice mass variations in much lower spatial resolutions, about 400km. Therefore,  $M_G - G\langle m \rangle$ , the rightmost term of the equation (4.17), includes mostly the Gaussian smoothed but opposite sign of error in  $\langle m \rangle$ . The smoothed effect, however, is recovered during the linear deconvolution, and thus the large error in  $\langle m \rangle$  can be effectively canceled in the CLD solutions. For example, the accumulated uncertainty over the entire AIS is only about 9.4Gton.

We also estimated systematic errors by inaccurate GIA models. Similar to previous sections, we obtained CLD solutions using the data corrected by four different GIA models, and the maximum difference in linear trends between CLD solutions was defined as a systematic error. Over the entire AIS, the systematic error cause by GIA model was about 28.3 Gton yr<sup>-1</sup>.

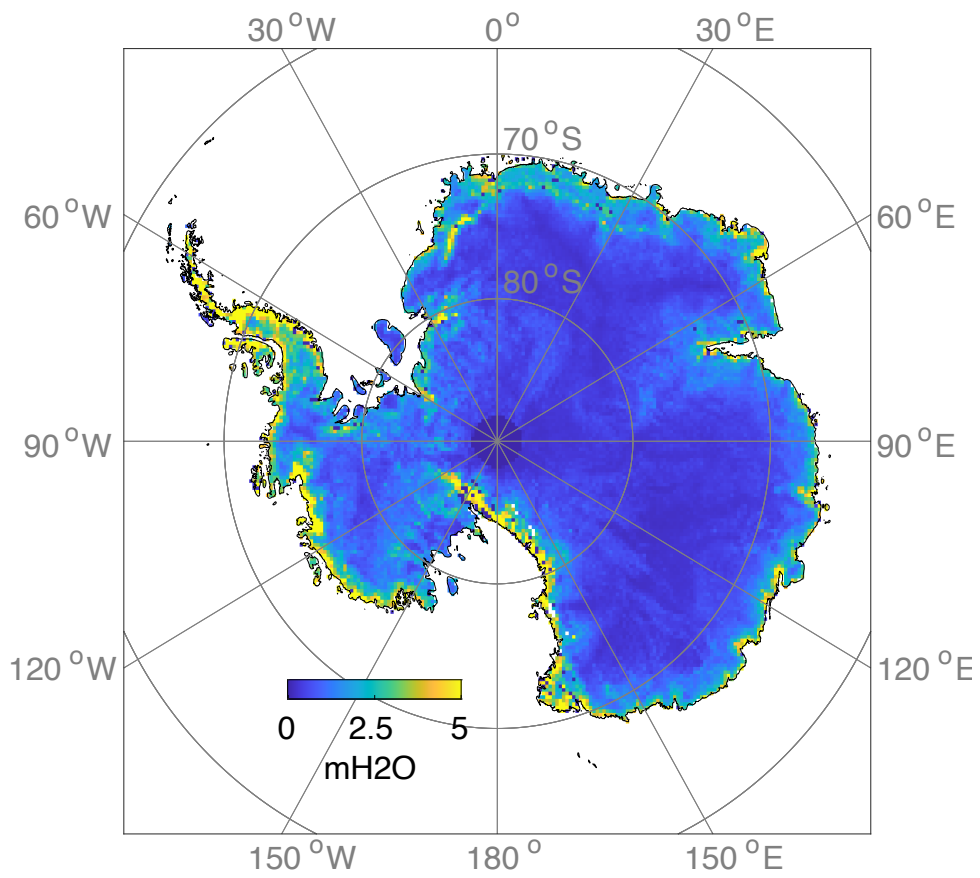


**Figure 4.8.** Uncertainties of the CLD solution over Antarctica.

#### 4.4. High resolution Antarctic ice mass loads

Figure 4.9 shows time-series of total ice mass changes for the AIS obtained by FM and CLD methods. A similar time-series from satellite altimetry is also presented. Both FM and CLD results are constrained to agree with smoothed GRACE data, so provide nearly identical AIS loss rates;  $-144.8 \pm 26.4 \text{ Gton yr}^{-1}$  from FM and  $-146.2 \pm 28.7 \text{ Gton yr}^{-1}$  from CLD. The altimetry-only rate is very different ( $-106.9 \pm 15.6 \text{ Gton yr}^{-1}$ ).

FM and CLD rate maps show significant differences between Figures 4.10a and 4.10b. The FM rate map (Figure 4.10a) shows effects of Gaussian smoothing, lacking signals at glacier scales. The CLD map (Figure 4.10b) shows Thwaites, Pine Island and Totten ice loss consistent with radar (McMillan et al., 2014; Rignot et al., 2019), and SMB variations (Van Wessem et al., 2014). The CLD map (Figure 4.10b) shows stronger negative linear trends at glacier outlets where increased ocean temperatures are important (Li et al., 2016; Pritchard et al., 2012). The CLD rate map also provides a more detailed view of ice mass gains in Whillans and Kamb Ice Streams, West Antarctica, associated with reduced (stagnated) glacial flow (Joughin et al., 2005; Retzlaff & Bentley, 1993). Mass gains are evident in Dronning Maud Land, East Antarctica, due to increased snowfall (Boening et al., 2012). Although the two rate maps in Figure 4.10 are very different, they are very close to one another and to GRACE observations when smoothed to GRACE resolution (Figures 4.11a and b).

GRACE mascon solutions, (defined at grid points with higher spatial resolution and leakage correction) are also available. Figure 4.12a-c shows spatial maps of AIS's loss rates from CSR, NASA Jet Propulsion Laboratory (JPL), and Goddard Space Flight Center (GSFC) mascons, respectively. Spatial resolution is improved relative to the FM solution, but maps are smoother than CLD estimates (Figure 4.10b).

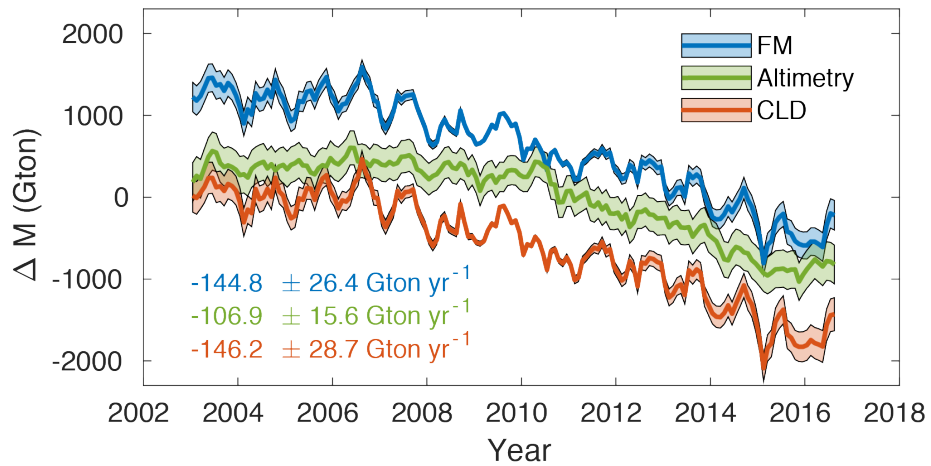


**Figure 4.9.** Time-series of Antarctic total mass variability estimated by FM (blue), Altimetry (green), and revised CLD (red). Linear trends and their confidence intervals are indicated in the same color as graphs.

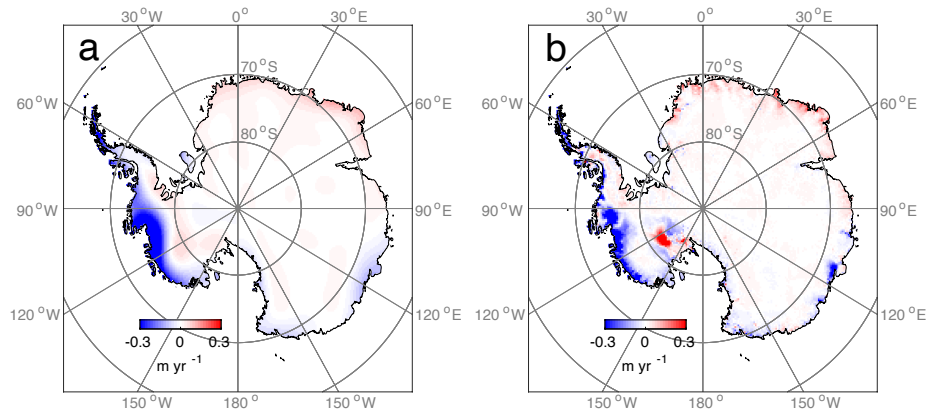


**Figure 4.10.** Linear trend maps of ice mass loads estimated by FM (a) and the revised CLD (b).

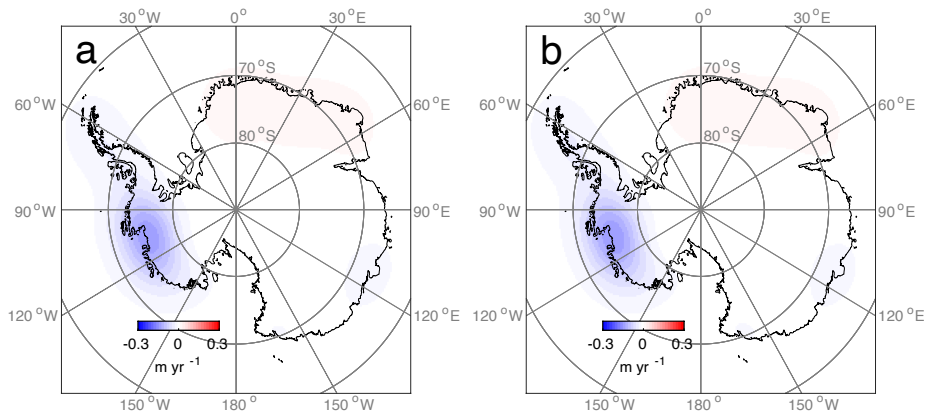


**Figure 4.11.** Similar to Figure 4.10 except that mass fields are smoothed by 400km Gaussian filter.

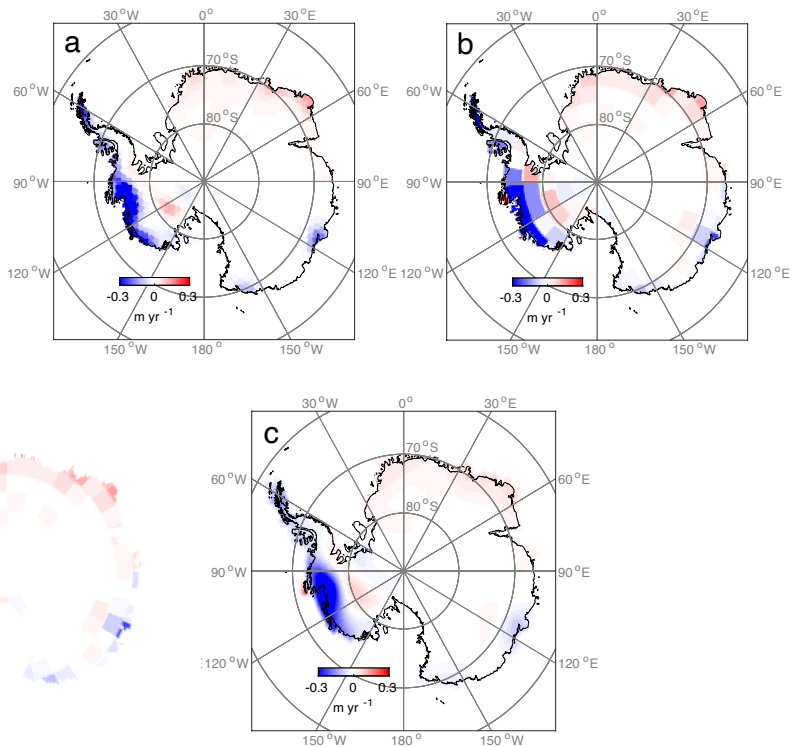


**Figure 4.12.** Linear trend maps of Antarctic ice mass change from CSR (a), JPL (b), and GSFC (c) mascon solutions.

## 4.5. AIS glacier mass balance

We estimated monthly ice mass variations at individual Antarctic glaciers using both FM and CLD methods and compared them with estimates from the Input-output method (IOM). In the past, it has been difficult to compare GRACE with glacier scale ice mass change from IOM because GRACE spatial resolution is so poor.

Ice mass changes ( $\Delta M$ ), from the IOM combine SMB from the ice sheet interior with ice discharge ( $\int D$ ) across grounding lines via:

$$\Delta M = SMB - \int D. \quad (4.21)$$

Rignot et al. (2019) estimated annual (1979-2017) discharge ( $D$ ) for individual Antarctic glaciers using surface velocity observations from satellite imagery and revised ice thickness data at grounding lines. Multiple reanalysis models provide estimates of continent-wide Antarctic SMB. In this study, we use RACMO2.3p2, as in section 4.2.2.  $\Delta M$  from IOM can be compared with our time-variable mass fields by partitioning the total ice sheet into glacier-scale areas. Glacier boundaries are taken from the MEaSURES-2 project (Mouginot et al., 2017; Rignot et al., 2013), as used by Rignot et al. (2019).

Pine Island and Thwaites Glaciers are in West Antarctica and are the two largest Antarctic contributors to ongoing sea-level rise over the last decades (Rignot et al., 2019). Jutulstraumen Glacier is in Dronning Maud Land in East Antarctica, where snowfall accumulation has abruptly increased since 2009 (Boening et al., 2012) and a positive mass rate is expected. The time-series of ice mass at three glaciers from FM (blue), satellite altimetry-only (green), CLD (red), and IOM (black) are shown together in Figure 4.13a-c, respectively. We calculated linear trends of four time-series and using a second-order polynomial fit ( $a_0 + a_1 t + \frac{1}{2} a_2 t^2$ ), where  $a_1$  is the linear rate we used. Estimated trends are shown with the same colors in the figure.

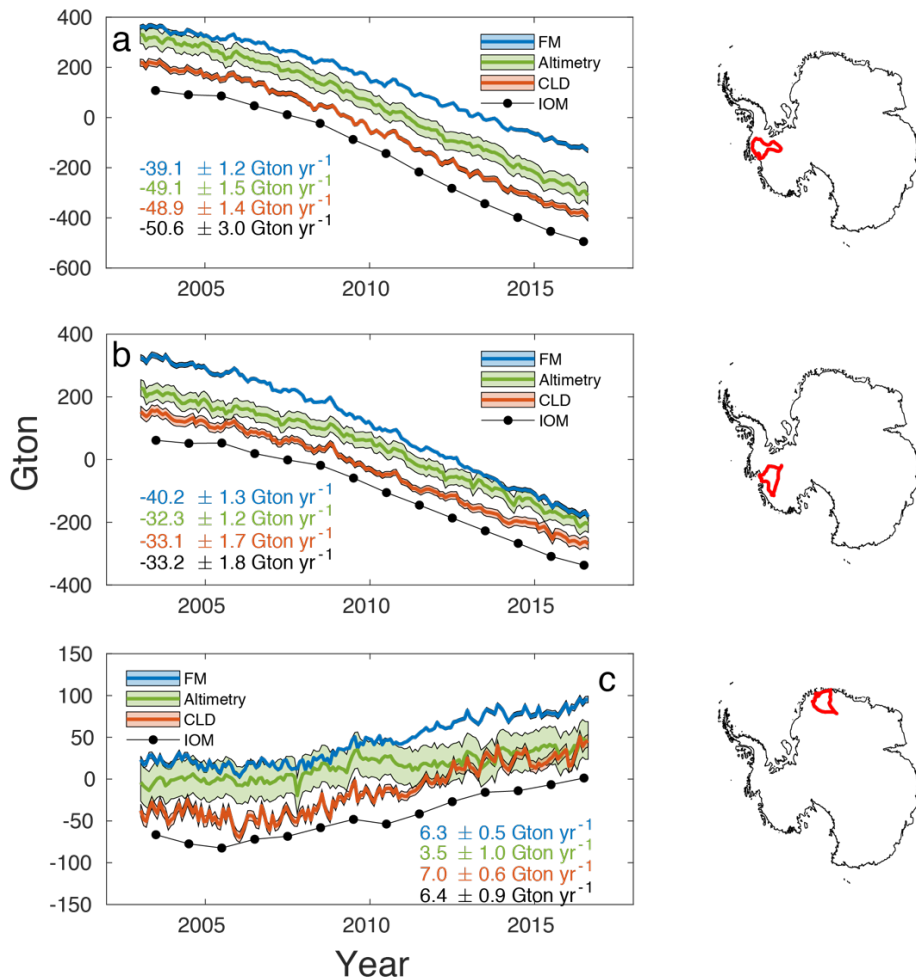


**Figure 4.13.** Comparison of ice mass variability at (a) Pine Island, (b) Thwaites, and (c) Jutulstraumen Glaciers estimated from FM (blue), Altimetry (green), CLD (red), and IOM (black). Linear trends and corresponding uncertainties (with 95% confidence intervals) are in the same colors on each panel.

For Pine Island Glacier (Figure 4.13a), the FM (blue) rate is  $-39.1 \text{ Gton yr}^{-1}$ , about 23% smaller than the IOM rate (black dotted),  $-50.6 \text{ Gton yr}^{-1}$ . The Thwaites Glacier (Figure 4.13b) FM rate is  $-40.2 \text{ Gton yr}^{-1}$ , larger than the IOM value,  $-33.2 \text{ Gton yr}^{-1}$ . Despite magnitude differences, FM provides consistently negative rates in agreement with IOM. FM signals are smooth, so blend signals from the two glaciers, and in addition, Thwaites is adjacent to Haynes, Pope, Smith, and Kohler Glaciers, all of which experienced a sharp decrease in ice thickness near the grounding line over the last three decades (Konrad et al., 2017). The FM solution would likely include spatial leakage from those glaciers. Mass change estimates from satellite altimetry (green) and CLD (red) agree well with IOM estimates for both Thwaites and Pine Island glaciers, confirming the consistency among multiple geodetic techniques.

In the Jutulstraumen Glacier, FM and CLD estimates are in agreement with IOM (Figure 4.13c), although they reflect differing spatial resolution. The mass increase in the Jutulstraumen basin is concentrated in a narrow area (the stoss side of wind direction) due to the interaction of atmospheric circulation and rough topography (Lenaerts et al., 2013). Because the glacier basin (red line on the right side of Figure 4.13c) is large compared to the area of large snow accumulation, mass balance in this region would be less affected by basin-to-basin leakage in the FM estimate. On the other hand, satellite altimetry alone underestimates ice mass increase compared to other three methods, possibly the result of errors associated with rough topography, or errors in the firn density model. Our CLD estimate based upon the same altimetry data, overcomes apparent shortcomings of altimetry in this region by requiring agreement with GRACE data.

We extend the analysis to glacial basins for the entire AIS basins excluding those with areas smaller than  $1000 \text{ km}^2$ . Mass rates from FM, satellite altimetry, CLD, and IOM, are computed. Three scatter plots are produced using IOM on the horizontal axis in Figure 4.14. Estimates from FM (Figure 4.14a), satellite altimetry (Figure 4.14b), and CLD (Figure 4.14c) for smaller glaciers (upper right-hand corner)

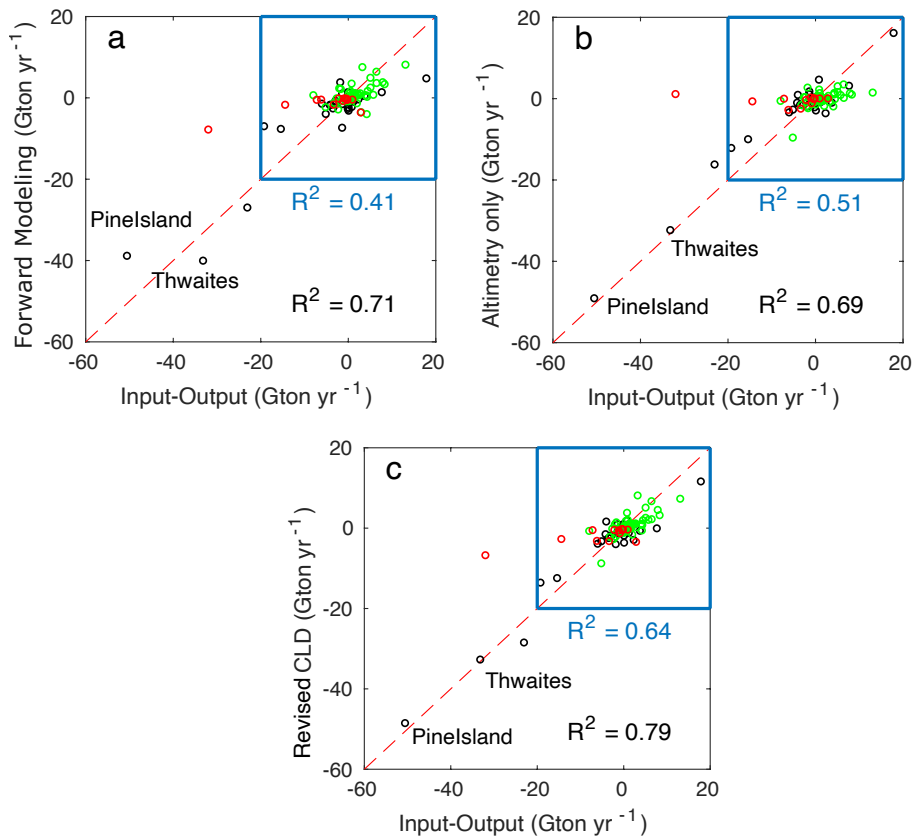


**Figure 4.14.** Comparison of linear changes in ice mass estimated from the IOM (x-axis) and three methods (y-axis).

show progressively increasing coefficients of determination  $R^2$ . Including all AIS glaciers exceeding 1000 km<sup>2</sup>,  $R^2$  increases slightly from 0.69 (Altimetry) to 0.71 (FM) to 0.79 (CLD). The modest improvement with CLD by including the largest glaciers reflects the fact that mass rates from all three methods and IOM are reasonably well determined for these larger areas.

Similar improvements are also found in glacier basins within West Antarctica (black circles in Figure 4.14) and East Antarctica (green circles). In West Antarctica,  $R^2$  values for FM and altimetry are 0.84 and 0.94, respectively.  $R^2$  using CLD is 0.94, similar to altimetry. In East Antarctica, CLD gives a much larger value (0.51) compared with FM (0.34) and altimetry (0.24). However, FM provides a larger  $R^2$  (0.61) than CLD (0.58) and altimetry (0.06) for the Antarctic Peninsula (red circles). A slightly lower  $R^2$  for CLD is likely due to poor satellite altimetry observations (used as the a priori) in the Antarctic Peninsula (Schröder et al., 2019). Disagreements between our CLD and IOM estimates are also partly associated with uncertainties in IOM, based on ice discharge and SMB. SMB is obtained from numerical models, and ice discharge is estimated by both observation of ice flow velocity and ice thickness at grounding lines (Rignot et al., 2019).

## 4.6. Conclusions

It has been difficult to estimate ice mass changes for AIS glacier basins from conventional GRACE data due to leakage error. The CLD method provides improved spatial resolution by using GRACE to constrain satellite altimetry data as an a priori. As a result, the glacial-scale ice mass changes can be estimated more accurately by CLD (see Appendix). CLD estimates provide higher spatial resolution and suppress spatial leakage. Ice mass change anomalies occurring at glacial scales agree well with those from the IOM method (based on radar remote sensing and regional climate models). GRACE estimates are important constraints because they provide spatial pattern of ice mass change at monthly time scales. The IOM method

only provides an annual flux estimate at glaciers outlets.

The CLD method may be supplemented with other in-situ and remote sensing data such as GNSS loading information and results from new altimetry missions (e.g., ICESat-2). Detailed understanding of glacial scale ice mass variations revealed by the CLD approach should be important in future glacier mass balance and sea level projections.

# **Chapter 5. Estimation of GIA effect beneath the Antarctic Glacier using multiple remote sensing and climate models**

## **5.1 Introduction**

Solid earth under the Antarctic glaciers has been uplifted due to the viscoelastic response of the upper mantle by deglaciation. This effect is known as glacial isostatic adjustment (GIA) and estimated to have rates from several to tens of mm per year over the Antarctic Ice Sheet (AIS). An accurate understanding of the GIA effect is essential for observing the present-day AIS mass change. For example, GRACE & GRACE-FO gravity satellites (2002-present) observe mass changes caused by both ice and solid earth. To separate the ice mass variability from the observation, the solid earth mass change must be corrected using appropriate GIA models (Tapley et al., 2019).

Despite its importance, the Antarctic GIA is still poorly understood due to the limited in-situ observations. Since most surface of the Antarctica is covered with thick ice, the physical properties or motion of bedrock cannot be directly observed. Observation networks (e.g., Global Navigation Satellite System (GNSS)) are only deployed at exposed bedrock areas, limiting the identification of the overall spatial pattern of the Antarctic GIA. Indirect estimation of bedrock elevation changes using ice surface elevation and ice thickness observations is also very challenging due to the viscous internal deformation and basal sliding of glaciers. Accordingly, current understanding of GIA effect heavily relies on numerical models, which simulate the relaxation time of isostatic adjustment (reflecting the mantle's viscosity) with the historical ice coverages and its melting history (Roy & Peltier, 2015). However, the GIA effect suggested by various models are not consistent with each other (Whitehouse et al., 2019), leading to highly scattered estimates in Antarctic mass loss rates, about 40 Gtons yr<sup>-1</sup> (Shepherd et al., 2012)).

The Kamb Ice Stream, adjacent to the Ross Ice Shelf in West Antarctica, is

a region where a number of GIA models estimate the highest uplift rates over Antarctica (Figure 5.1). For example, a GIA model of Peltier et al. (2018) estimates that the apparent average mass rate associated with GIA in the KIS is about  $6.3 \text{ Gton yr}^{-1}$ . The high uplift in the KIS is probably because it reflects the large deglaciation history and the low mantle viscosity in West Antarctica. However, the estimation is largely uncertain due to limited observational evidences (Peltier et al., 2015; Whitehouse et al., 2019).

The KIS was stagnated about 160 years ago (Retzlaff & Bentley, 1993), and there is no present-day glacial flow at the downstream trunk (Rignot et al., 2017). The amount of ice discharge at the grounding line is negligible, and only the surface mass balance (SMB: time integration of snowfall and sublimation) contributes to the mass increase in this region (Rignot et al., 2019). The glacial-scale SMBs in AIS have been well understood by global climate reanalysis models (e.g., ECMWF ERA5 (Hersbach et al., 2019)) and regional climate models (e.g., RACMO (Van Wessem et al., 2014) and MAR (Agosta et al., 2019)). In addition, recent development of inversion with GRACE including satellite altimetry data as a priori allows to estimate glacial-scale mass variability in AIS. Since GRACE detects the ice and sub-ice mass variability at once, it may be possible to estimate the mass change due to solid earth under the KIS when comparing GRACE data with SMB estimates. Based on this idea, we investigate the mass changes induced by the solid earth's uplift under the KIS during the period of 2003-2016.

## 5.2 Data & Method

### 5.2.1 Method

The mass change in Antarctica is occurred to firn ( $\Delta\sigma_f$ ) and ice layer ( $\Delta\sigma_i$ ), and bedrock ( $\Delta\sigma_r$ ). GRACE ( $\Delta\sigma_{GRACE}$ ) observation provides a sum of the mass changes in the three layers:

$$\Delta\sigma_{GRACE} = \Delta\sigma_i + \Delta\sigma_f + \Delta\sigma_r \quad (5.1)$$

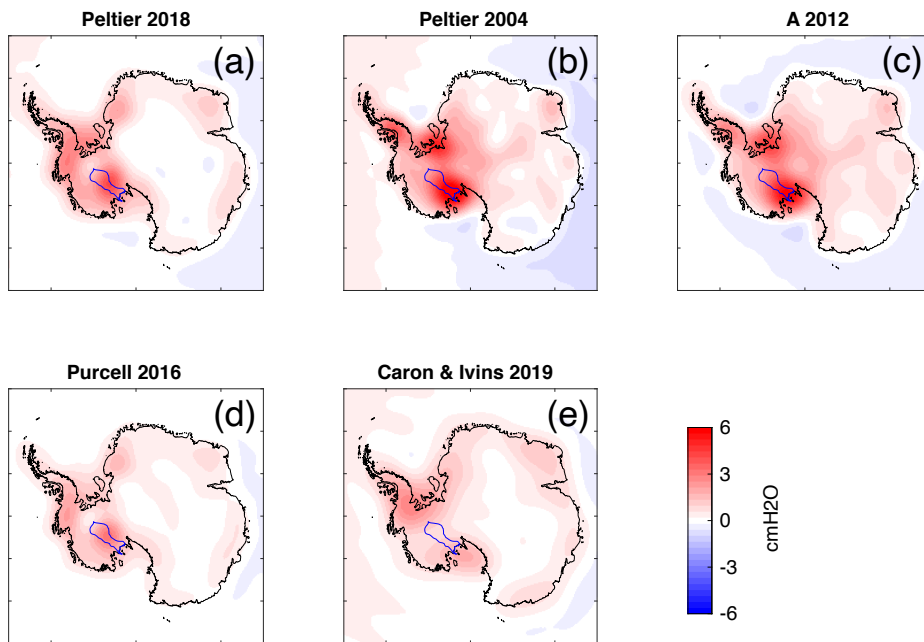


**Figure 5.1.** Apparent surface mass variability due to GIA effects estimated by multiple GIA models; (a) Peltier et al. (2018) (a), Peltier (2004) (b), A et al. (2012) (c), Purcell et al. (2016) (d), and Caron and Ivins (2019) (e). Blue lines are boundary of the KIS (see Chapter 5.2.2).

In KIS, where ice flow is stagnant,  $\Delta\sigma_i$  is negligible and  $\Delta\sigma_f$  is explained by SMB. Accordingly, equation (5.1) is simplified as follows:

$$\Delta\sigma_{GRACE} = \Delta\sigma_r + \Delta SMB. \quad (5.2)$$

By removing *SMB* from GRACE observation, the mass change induced by GIA ( $\Delta\sigma_r$ ) would be estimated.

Current numerical models simulate SMB with spatial resolutions of several tens of km (Chapter 5.2.3), which resolution is high enough to examine SMB variability ( $\Delta SMB$ ) at glacial scale. However, GRACE has been limited in the examination of glacial scale ice mass changes due to the inherent low spatial resolution (a few hundred km). Simply subtracting  $\Delta SMB$  from  $\Delta\sigma_{GRACE}$  will yield a highly inaccurate  $\Delta\sigma_r$  in a glacial basin due to the low spatial resolution of GRACE. To constrain the mass changes ( $\Delta\sigma_{GRACE}$ ) within KIS, GRACE data needs to be re-processed to higher-resolution as suggested in Chapter 4. This issue will be briefly addressed again in the following sections.

### 5.2.2 Basin boundary

NASA Making Earth System Data Records for Use in Research Environments (MEaSUREs) Program (Rignot et al., 2017) provides high-resolution boundary of individual Antarctic glaciers based on the observation of glacial velocity fields by satellites. However, we find that the boundary of KIS defined by the MEaSUREs (blue line of Figure 5.2) does not include parts of the southern tributary flowing into the downstream trunk. Therefore, we revise the basin boundary of KIS to include all of the ice stream catchments. The red line of Figure 5.2 shows the new boundary.

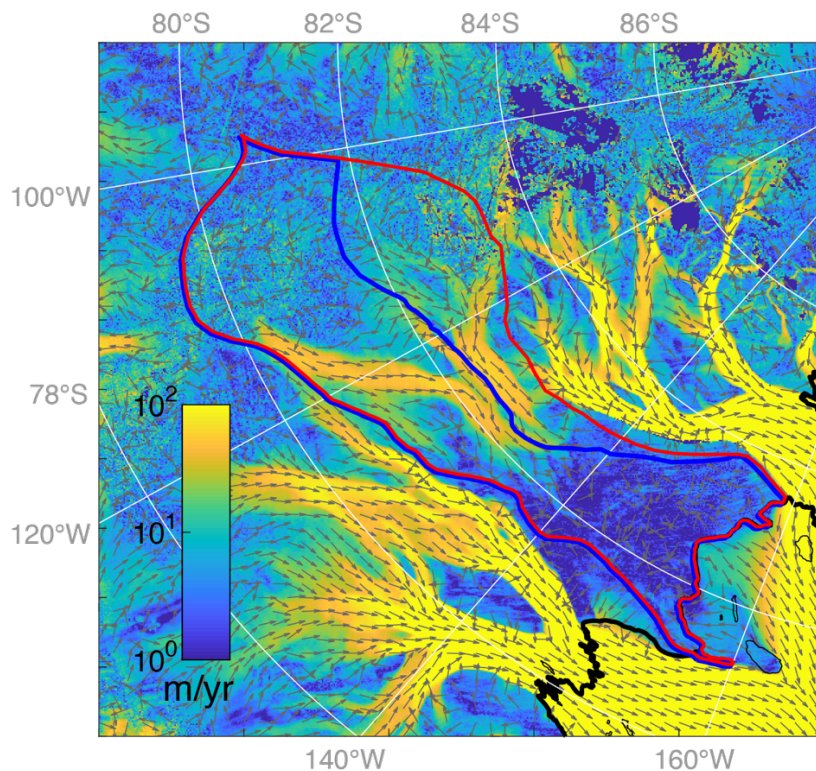


**Figure 5.2.** Glacier flow speeds (color shading) and their directions (gray arrows) near KIS provided by MEASUREs2 project (Rignot et al., 2017). The blue line is the boundary of the KIS provided by the same repository, and the red line is the new boundary defined in this study (Chapter 5.2.2). Black line is grounding line from Modis Mosaic of Antarctica (MOA) 2014 (Scambos et al., 2007).

### 5.2.3 SMB models

To estimate the ice mass variability (2003-2016) induced by SMB, we used state-of-the-art climate models: European Centre for Medium-Range Weather Forecasts reanalysis 5 (ERA5) (Hersbach et al., 2019), Regional Atmospheric Climate Model (RACMO) 2.3p2 (Van Wessem et al., 2014), and Modèle Atmosphérique Régional (MAR) v3.6.4 (Agosta et al., 2019). ERA5 is an updated version of the previous ERA-Interim global reanalysis model (Dee et al., 2011) and has a spatial resolution of 31km. RACMO2.3p2 is a regional climate model with a spatial resolution of 27 km and is forced by the ERA-Interim. MAR is another regional climate model simulated with a spatial resolution of 35 km and provides three types of data, which is forced by ERA-Interim, MERRA2, and JRA-55 global reanalysis, respectively. Considering the three sub-models of MAR as independent data, we have a total of five different SMB models. To reduce the influence of different spatial resolutions on the estimated mass change, ERA5 and MAR were re-sampled with 27km grid intervals, the spatial resolution of RACMO2.3p2.

### 5.2.4 Mass densities from GRACE data

GRACE gravity satellite observes the temporal variation of the gravitational potential, and the data are provided as spherical harmonic (SH) coefficients. Using the linear relationship between mass and gravitational potential, the observed potential field is converted into surface mass densities (Wahr et al., 1998). We used CSR RL06 level 2 monthly (2003-2016) SH product as GRACE observation. Degree 1, and degree 2 and order 0 coefficients were replaced with estimates in supplementary datasets in GRACE Technical Notes 13 (Landerer, 2019) and 14 (Loomis et al., 2019), respectively. Spatial aliasing errors were removed by sequential application of decorrelation filter (Swenson & Wahr, 2006) and Gaussian filter with a radius of 400km (Wahr et al., 1998). Unlike the conventional processing schemes, we did not apply any GIA correction to include its effect in GRACE data (Chapter 5.2.1).

### 5.2.5 Mass densities from satellite altimetry data

We estimate mass densities from satellite altimetry, which will be used in Chapter 5.2.6 for joint estimation with GRACE data. We used multi-mission satellite altimetry data from 2003 to 2016 calculated by Schröder et al. (2019). Nominally, satellite altimetry observations provide surface elevation changes ( $\Delta H_{alt}$ ) caused by ice ( $\Delta H_i$ ) and firn thickness variability ( $\Delta H_f$ ), and vertical displacement of bedrock ( $\Delta H_r$ ):

$$\Delta H_{alt} = \Delta H_i + \Delta H_r + \Delta H_f. \quad (5.3)$$

The thickness observation can be converted to mass variations,  $\Delta\sigma_{alt}$ :

$$\Delta\sigma_{alt} = \rho_i\Delta H_i + \rho_r\Delta H_r + \rho_f\Delta H_f = \rho_i\Delta H_i + \rho_r\Delta H_r + \Delta SMB \quad (5.4)$$

where  $\rho_i$ ,  $\rho_r$ , and  $\rho_f$  are density of ice (917 kg m<sup>-3</sup>), bedrock (unknown), and firn layer (unknown), respectively, and  $\Delta SMB$  is SMB variations. Since the satellite altimeter does not distinguish the elevation changes in each layer, the typical volume-mass conversion process requires additional numerical models that describe the bedrock elevation and firn thickness variability.

$\Delta H_i$  and  $\Delta H_f$  are negatively correlated because the bottom-most firn layer is continuously converted to the ice layer during the densification process. On the other hand, the intermittent snowfall accumulations compensate for the thickness loss at the bottom of the firn layer. Therefore,  $\rho_f$  varies during the acquisition of new firn by snowfall and the loss of old firn to ice. The time-varying firn thickness (1979-2016) is provided by IMAU-FDM (Ligtenberg et al., 2011), which is empirically simulated using RACMO2.3p2 model. We used the data from 2003 to 2016 to calculate the firn thickness changes during our study period. We removed the linear trend of firn thickness change during 1979-2002 from the data during 2003-2016,

and used the residuals as  $\Delta H_f$ . Here we assumed that the period from 1979 to 2002 is long enough to equilibrate the acquisition (due to snow accumulation) and loss (due to firn compaction and downward ice flow) in the firn layer over the KIS basin, and that the imbalance over the subsequent period have changed the firn thickness. By subtracting  $\Delta H_f$  from  $\Delta H_{alt}$  and adding back the effect of SMB, we obtained a new mass density:

$$\Delta\sigma_{alt}^* = \rho_* (\Delta H_{alt} - \Delta H_f) + \Delta SMB_a = \rho_* (\Delta H_i + \Delta H_r) + \Delta SMB. \quad (5.5)$$

$\Delta SMB$  used here is the SMB anomaly (2003-2016) from RACMO2.3p2 after removing the linear trend estimated from the SMB during 1979-2002 as we have done with the firn density model.  $\rho_*$  is a density corresponding to the total volume change of the bedrock and ice layer. Strictly,  $\rho_*$  should be an intermediate value of bedrock and ice density. But here we assumed the density of ice ( $\rho_i$ ) as  $\rho_*$ :

$$\Delta\sigma_{alt}^* = \rho_i (\Delta H_{alt} - \Delta H_f) + \Delta SMB_a = \rho_i (\Delta H_i + \Delta H_r) + \Delta SMB_a. \quad (5.6)$$

This assumption causes the estimated mass density ( $\Delta\sigma_{alt}^*$ ) differs from actual mass density ( $\Delta\sigma_{alt}$ ) by the amount of,  $\Delta\sigma_{alt} - \Delta\sigma_{alt}^* = (\rho_r - \rho_i)\Delta H_r$ . In the next section, we will show that the difference becomes negligible after the joint estimation of GRACE and altimetry data.

### 5.2.6 High-resolution GRACE data and its sensitivity to GIA estimates

A recent study (Kim et al., in prep) has reported that the spatial resolution of GRACE observations in AIS can be greatly improved ( $\sim 27$ km) by a revised method of constrained linear deconvolution (Seo et al., 2020) (revised CLD). The revised CLD estimates high-resolution surface mass loads from GRACE data by using

satellite altimetry data (after volume-mass conversion) as a-priori. The linear equation of the revised CLD is (Kim et al., in prep)

$$\begin{bmatrix} \hat{m} \\ \hat{h} \end{bmatrix} = \begin{bmatrix} \Delta\sigma_{alt}^* \\ 0 \end{bmatrix} + \begin{bmatrix} G^T P G + \lambda W & H^T \\ H & 0 \end{bmatrix}^{-1} \begin{bmatrix} G^T P (\Delta\sigma_{GRACE} - G\Delta\sigma_{alt}^*) \\ h \end{bmatrix} \quad (5.7)$$

where  $G$ ,  $\lambda$ ,  $P$ , and  $W$  are Gaussian smoothing matrix, regularization factor, diagonal weighting matrix, and steepness (smoothness) matrix, respectively.  $H$  is a matrix whose diagonal elements are ones in the ocean and zeros in the inland area.  $h$  is a zero vector, and  $\hat{h}$  is a null vector.  $\hat{m}$  is a vector of model parameters to be estimated, high-resolution surface mass loads. The definitions for each term are the same as shown in section 4.3.2.

In the above section 5.2.5, we recognized that  $\Delta\sigma_{alt}^*$  (as used the first term in the right-hand side of the equation (5.7)) from satellite altimetry includes error associated with using the same ice density for volumetric variations of ice layer and solid earth uplift of GIA. Therefore, spatial scales of the expected errors would be similarly large scale of GIA effect, distinctly different from smaller spatial scale of ice variations. The error can be understood by  $\Delta\sigma_{GRACE} - G\Delta\sigma_{alt}^*$  in the second term of the right-hand side of the equation (5.7) while the error in  $\Delta\sigma_{GRACE} - G\Delta\sigma_{alt}^*$  is smoothed by the Gaussian kernel and opposite sign to the error in  $\Delta\sigma_{alt}^*$ . Because the smoothing effect of the error in  $\Delta\sigma_{GRACE} - G\Delta\sigma_{alt}^*$  is mostly diminished via constrained linear deconvolution using the kernel of the inverse matrix, the error will be mostly canceled in from the equation (5.7).

To examine the error reduction, we generated new surface mass loads,  $\Delta\sigma_{alt}^{**}$ , by removing expected surface mass loads estimated by a GIA model of Peltier et al. (2018) from  $\Delta\sigma_{alt}^*$ . We then used  $\Delta\sigma_{alt}^{**}$  instead of  $\Delta\sigma_{alt}^*$  in the revised CLD, defining  $\hat{m}_2$  as the estimated mass loads using  $\Delta\sigma_{alt}^{**}$ . Because effect associated with GIA was removed from  $\Delta\sigma_{alt}^*$ ,  $\Delta\sigma_{alt}^{**}$  includes the similar error generated by using the same density of the uplift bedrock to that of the ice layer as in equation (5.6). Figure 5.3a

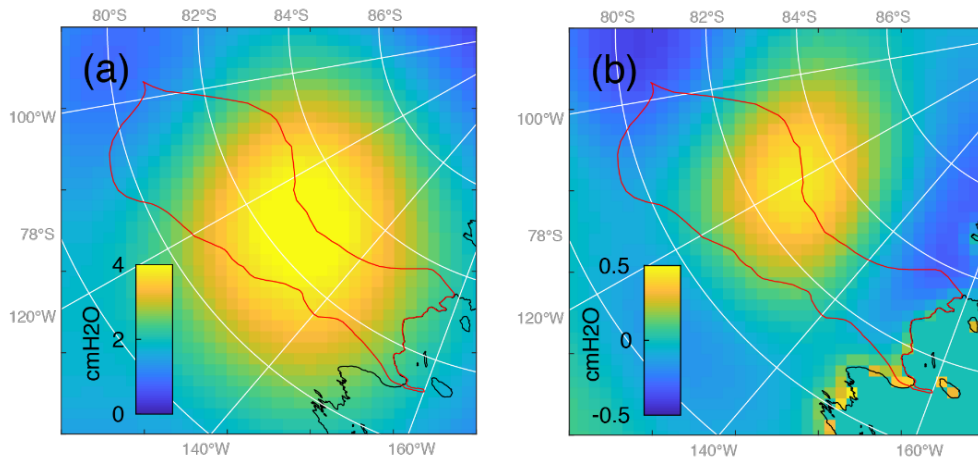
shows the spatial pattern of the linear trend difference between  $\Delta\sigma_{alt}^*$  and  $\Delta\sigma_{alt}^{**}$ , which is the same as the mass loads estimated by the GIA model of Peltier et al. (2018). The maximum value is about 4.2 cmH<sub>2</sub>O yr<sup>-1</sup>, located in the midstream of the KIS. The average value within the KIS basin is about 3.0 cmH<sub>2</sub>O yr<sup>-1</sup>, which is equivalent to 6.3 Gton yr<sup>-1</sup> over the entire basin.

Figure 5.3b shows the spatial pattern of linear trend difference between  $\hat{m}$  and  $\hat{m}_2$ , which are estimated by the observations of  $\Delta\sigma_{alt}^*$  and  $\Delta\sigma_{alt}^{**}$ , respectively. Most anomalies shown in Figure 5.3a are largely suppressed: total anomaly is about 0.2 Gton yr<sup>-1</sup>, much smaller than Figure 5.3a. This test demonstrates that it is possible to estimate variations of surface loads from combined observation of ice mass variations and solid earth uplift in glacial scale by suppressing uncertainty associated with unknown effect of bed rock uplift rate and its density.

## 5.3 Result & Discussion

### 5.3.1 Estimated mass rates

Figure 5.4a shows a linear trend map of mass changes near the KIS estimated by the revised CLD (The trend map of the entire AIS is shown in Figure 5.5). The increasing trend is dominant within the basin boundaries of KIS, with an average rate of about  $+11.2 \pm 0.4$  cmH<sub>2</sub>O yr<sup>-1</sup>. The maximum value of the trend is about  $+49.3 \pm 0.3$  cmH<sub>2</sub>O yr<sup>-1</sup> and is located in the midstream where glacial flow remains. As previously noted, the total mass change of KIS is affected by SMB and GIA effect. On a smaller spatial scale, the upstream glacial flow (Figure 5.2) supplies ice to the downstream, forming high increasing mass trends on the stagnant area. Such mass exchanges are only occurred within the basin, and thus do not affect the total mass change over the basin. Slight decreasing trends are shown in the upstream pixels, with a minimum rate of about  $-2.6 \pm 0.3$  cmH<sub>2</sub>O yr<sup>-1</sup>. This is probably because the amount of ice transferred to the downstream during the study period was larger than the SMB accumulation.



**Figure 5.3.** (a) Map of differences between  $\Delta\sigma_{alt}^*$  and  $\Delta\sigma_{alt}^{**}$ . (b) Map of differences between two mass rates after the joint estimation. Red lines denote basin boundary of KIS (Chapter 5.2.1). Note that the color scales of the two images are different.

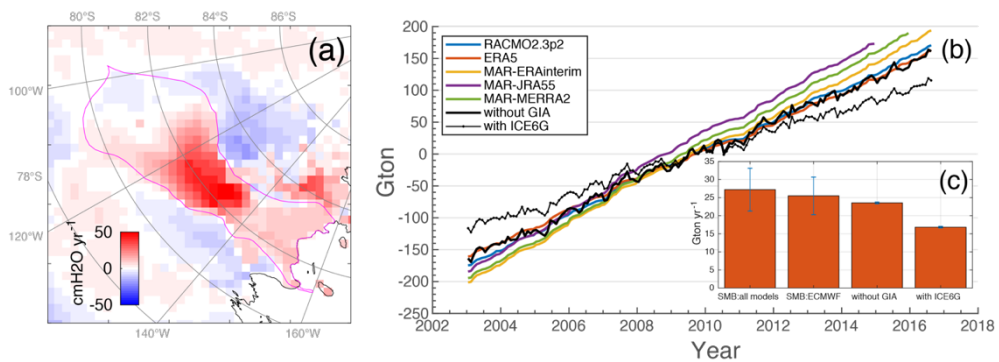


**Figure 5.4.** (a) Linear trend map of estimated mass changes near KIS. The magenta line is the boundary of the KIS. (b) Time-series of mass changes in KIS estimated by SMB models and the revised CLD. (c) Comparison of linear trends in mass variability shown in (b); the average of five SMB models (SMB: all models), the average of three ECMWF models (SMB: ECMWF), the revised CLD without GIA model (without GIA), and the revised CLD with a GIA model of Peltier et al. (2018).

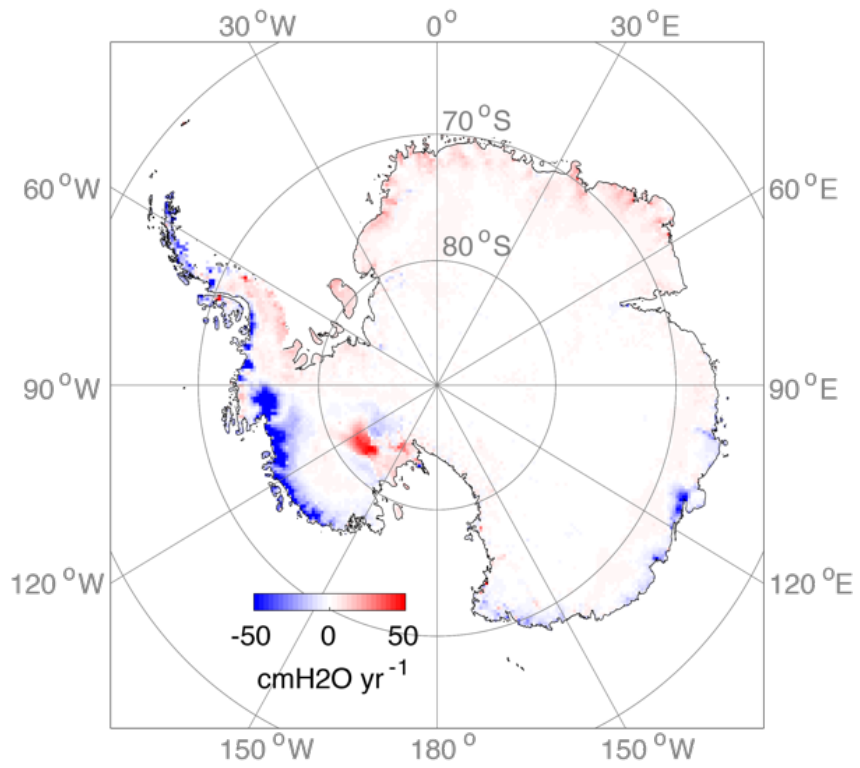


**Figure 5.5.** Similar to Figure 5.4(a) except for the entire Antarctic Ice Sheet.

### 5.3.2 GIA mass rate beneath the KIS

Figure 5.4b compares time-series of mass changes from SMB and revised CLD. For SMBs, the highest increasing trend is shown in the MAR forced by JRA-55 (purple line), which is  $+30.0 \pm 0.2$  Gton  $\text{yr}^{-1}$ . The lowest increasing trend is shown in the ERA5 reanalysis (red line), which is about  $+23.2 \pm 0.1$  Gton  $\text{yr}^{-1}$ . The average trend calculated by five SMB models is about  $+27.2$  Gton  $\text{yr}^{-1}$ , with the confidence interval (two standard deviations) of 5.9 Gton  $\text{yr}^{-1}$  (the first column in Figure 5.4c). Previous studies (Bromwich et al., 2011; Palerme et al., 2017) evaluated multiple reanalysis models and found that the ECMWF reanalysis is superior to other models in AIS. The average trend for SMBs calculated by three ECMWF-based models (RACMO, MAR forced by ERA-Interim, ERA5) is about  $+25.4$  Gton  $\text{yr}^{-1}$ , with the confidence interval of 5.2 Gton  $\text{yr}^{-1}$  (the second column in Figure 5.4c).

The black solid line of Figure 5.4b shows the mass change of the KIS estimated by the revised CLD without correcting GIA effect. The linear trend is about  $+23.5 \pm 0.2$  Gton  $\text{yr}^{-1}$  (the third column in Figure 5.4c), similar to the SMB trend by ERA5 ( $+23.2 \pm 0.1$  Gton  $\text{yr}^{-1}$ ) or RACMO ( $+24.9 \pm 0.1$  Gton  $\text{yr}^{-1}$ ). Subtracting the SMB from the total mass change (from the revised CLD), we can estimate the contribution of GIA (Equation (5.2)). Given the five SMB models, the possible mass rates induced by the GIA range from  $-9.8$  to  $+2.4$  Gton  $\text{yr}^{-1}$ . Using the three ECMWF SMB models, the GIA mass rates range from  $-7.3$  to  $+3.5$  Gton  $\text{yr}^{-1}$ . The rates are much closer to zero when ERA5 ( $+0.3$  Gton  $\text{yr}^{-1}$ ) and RACMO ( $-1.4$  Gton  $\text{yr}^{-1}$ ) are used.

The GIA model from Peltier et al. (2018) is the most widely used for the correction of GRACE data. If the GIA model reasonably depicts the GIA effect over KIS, the ice mass change estimated by the revised CLD incorporating the GIA model should be similar to the SMB changes according to Equation (5.2). The black dotted line of Figure 5.4b is the ice mass change estimated by the revised CLD incorporating the GIA model. The linear trend is about  $+16.8 \pm 0.2$  Gton  $\text{yr}^{-1}$  (the fourth column in Figure 5.4c), much smaller than the trend of all SMB models. The

GIA mass rate beneath the KIS indicated by Peltier et al. (2018) is about 6.7 Gton yr<sup>-1</sup>, which is larger than our estimates in this study. Similarly, GIA mass rates from other models are generally over-estimated, which are +8.9 Gton yr<sup>-1</sup> (A et al., 2012), +10.2 Gton yr<sup>-1</sup> (Peltier, 2004), +4.8 Gton yr<sup>-1</sup> (Purcell et al., 2016), and +3.0 Gton yr<sup>-1</sup> (Caron & Ivins, 2019), respectively.

## 4. Conclusion

We estimated the GIA mass rate under the KIS using multiple SMB models, high-resolution mass change estimates, and new basin boundary data. The estimated GIA mass rate ranges from -9.8 to +3.5 Gton yr<sup>-1</sup>. When ERA5 and RACMO SMB models were used, the rates were estimated to +0.3 Gton yr<sup>-1</sup> and -1.4 Gton yr<sup>-1</sup>, respectively. These rates were much smaller than that from the most widely used GIA model (Peltier et al., 2018), 6.7 Gton yr<sup>-1</sup>. The large difference in GIA mass rate between estimated here and the model is likely due to the uncertainty of the GIA model. The historical ice coverage used in Peltier et al. (2018) model was simulated by an ice sheet coupled climate model forced by a small number of paleoclimate proxy records and GNSS observations. Therefore, current GIA predictions particularly over Antarctica would be problematic.

This study was examined only on the KIS region, where ice flows are stagnant. It is clear that the evaluation of the limited region cannot represent the entire uncertainty of the model. KIS only accounts for 1.8% of the total area of AIS. To extend this study to the entire AIS, accurate ice discharge observations are necessary. Glacier flow rates at AIS's surface have been observed by satellite radar imagery (Rignot et al., 2019). However, glacier flow at fluxgate, an area where glaciers pass through the grounding line, is highly inaccurate due to limited observations and numerical models (Fretwell et al., 2013; Morlighem et al., 2020). Improving them through continuous efforts will help to produce a robust estimate of the Antarctic GIA.

## Chapter 6. Sea-level projections

In this dissertation, Antarctic SMB and glacial scale ice mass change along with suppressing residual GIA effect were examined. Those findings are all important to project future sea level changes. Antarctic ice mass changes ( $\Delta M$ ) includes evident high frequency variabilities and most of them are associated with  $\Delta SMB$  variations as shown in Chapter 3. On the other hand, the estimated ice discharge by subtracting  $\Delta SMB$  from  $\Delta M$  only showed multi-decadal accelerations with a significant linear trend (Figure 3.9). Using the estimated ice discharge, we can effectively project future ice mass change because it is expected that multi-decadal and longer variabilities are dominant in the change of ice discharge. In Chapter 4, the glacial-scale mass variability was estimated by increasing the spatial resolution of GRACE observation. Using the high-resolution mass change data, each contribution of the future sea-level rise from individual glaciers in Antarctica can be separated. Finally, we showed that the GIA model by Caron and Ivins (2019) is the best among currently available models (Chapter 5), which is significant information to understand the contemporary ice mass loss and its projection.

We first investigate different projections of future sea-level changes by using variations of ice discharge ( $\Delta D$ ) and ice mass ( $\Delta M$ ), separately. The ice discharge was estimated by subtracting  $\Delta SMB$  (from RACMO2.3p2) from the  $\Delta M$  (from the revised CLD), where  $\Delta SMB$  was obtained by removing the linear trend of 1979-2002 in the SMB variations. For  $\Delta M$ , we first reduced the GIA effect using the output from Peltier et al. (2018), which is currently most widely used. Later, we include the GIA model of Caron and Ivins (2019), the possibly best GIA model based on the Chapter 5. Two different projections of future sea-level changes driven by Antarctic ice mass loss are compared using long-term components (linear trend and acceleration during 2003-2016) of  $\Delta M$  and  $\Delta D$ .

The blue line in Figure 6.1a shows a time-series of  $\Delta M$ . The linear trend and acceleration are estimated as  $-152.5 \pm 7.2$  Gton yr<sup>-1</sup> and  $-18.1 \pm 4.1$  Gton yr<sup>-2</sup>,

respectively. The red line is the time-series of  $\Delta D$  showing that the high-frequency amplitudes are largely suppressed after removing  $\Delta SMB$  (Chapter 3). The linear trend and acceleration are reduced by 15% ( $-129.5 \pm 5.7 \text{ Gton yr}^{-1}$ ) and 39% ( $-11.0 \pm 3.2 \text{ Gton yr}^{-2}$ ), respectively. Confidence intervals of linear trend and acceleration estimates are also reduced by 21% and 22%, respectively. Figure 6.1b shows projections of future sea-level changes based on estimates of  $\Delta M$  and  $\Delta D$ . If the  $\Delta M$  is used for the projection (blue), the sea-level change in 2100 is about  $+24.4 \pm 4.8 \text{ cm}$ , consistent with previous estimates by ice dynamics modeling simulated with the RCP8.5 scenario (DeConto et al., 2021). On the other hand, the sea-level projection by  $\Delta D$  is about  $+16.0 \pm 3.8 \text{ cm}$ , 34% lower, and 21% less scattered than the projections using  $\Delta M$ .

A similar comparison is carried out for individual glaciers in Antarctica. The Thwaites and Pine Island Glaciers, which show the fastest ice mass loss rates among Antarctic glaciers, are selected as the target areas. Figure 6.2 shows future sea-level changes projected by mass loss rates at each glacier. The sea-level change in 2100 estimated by Thwaites's  $\Delta M$  is about  $+2.9 \pm 0.3 \text{ cm}$  (blue line in Figure 6.2a), but it reduces to  $+1.7 \pm 0.2 \text{ cm}$  (red line in Figure 6.2a) when considering  $\Delta D$ . Similarly, the sea-level change in 2100 by Pine Island Glacier is estimated to  $+4.4 \pm 0.4 \text{ cm}$  when using  $\Delta M$  but the value reduces to  $+2.9 \pm 0.2 \text{ cm}$  when considering  $\Delta D$ .

Subsequently, we tested the impact of the GIA model on GRACE data correction. Figure 6.3 shows another sea-level projection of the two glaciers estimated by  $\Delta D$  with the GIA model from Caron and Ivins (2019). The sea-level change in 2100 caused by the two glaciers is  $1.6 \pm 0.2 \text{ cm}$  (Thwaites Glacier, blue),  $2.8 \pm 0.2 \text{ cm}$  (Pine Island Glacier, red), which are not much different from the use of the GIA model from Peltier et al. (2018) (red lines in Figure 6.2). This is because the GIA mass rates presented by the two GIA models are similar to each other except for the KIS region (Figure 5.1). For the same reason, the sea-level change in 2100 by the entire AIS is about  $15.9 \pm 3.7 \text{ cm}$  (not shown in the figure), slightly different from the case when the GIA model from Peltier et al. (2018) is used ( $16.0 \pm 3.8 \text{ cm}$ ).

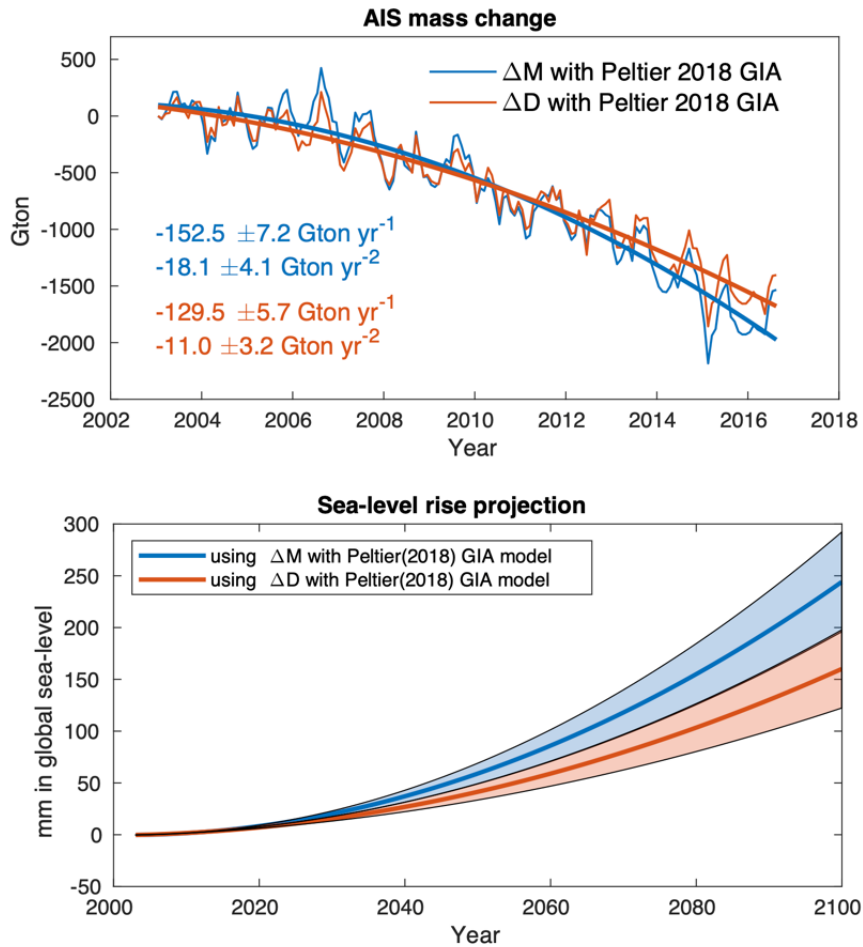


**Figure 6.1.** (a) Antarctic ice mass change (thin blue line) and ice discharge (thin red line) estimates. Thick blue and red lines show quadratic polynomial fits of the two time series. Linear trends and accelerations of each time-series are presented in the panel. The errors are estimated with 95% confidence intervals. (b) Future sea-level changes associated with Antarctic ice mass loss projected by using long-term components (linear trend and acceleration) of ice mass change (blue) and ice discharge (red).

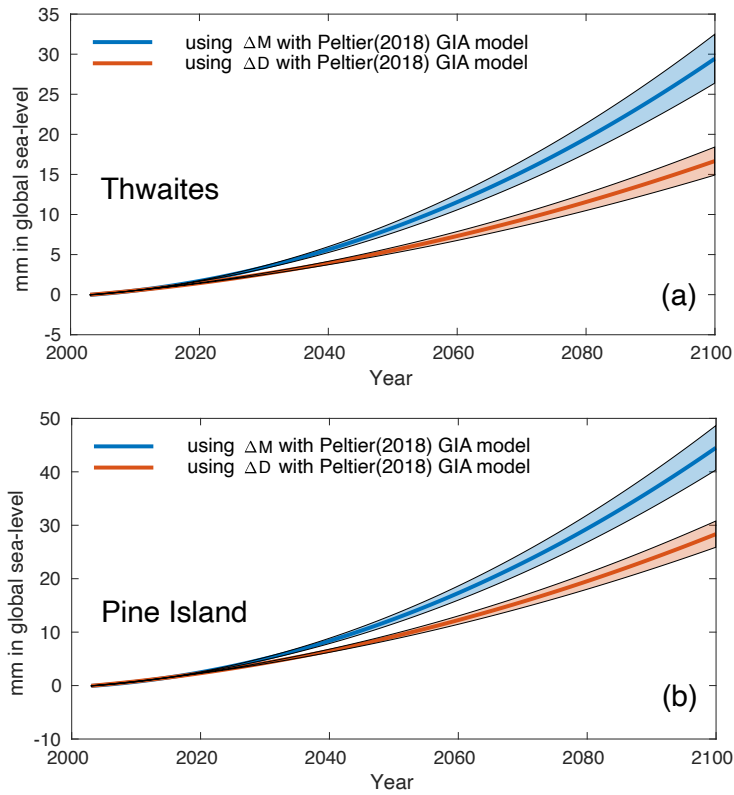


**Figure 6.2.** Future sea-level rise projected by mass loss in the Thwaites (a) and Pine Island (b) Glaciers.

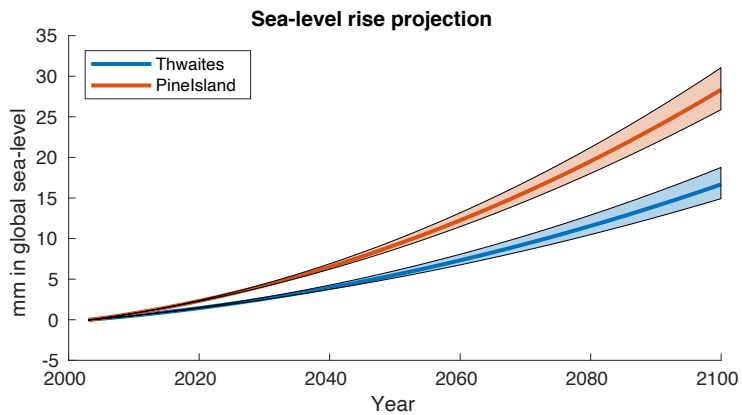


**Figure 6.3.** Future sea-level rise projected by  $\Delta D$  in the Thwaites (blue) and Pine Island (red) Glaciers. GIA model from Caron and Ivins (2019) is used for  $\Delta D$  estimates.

## Chapter 7. Conclusion

This dissertation aimed to understand the causes of the current Antarctic ice mass changes ( $\Delta M$ ), improve the spatial resolution of  $\Delta M$  and reduce the uncertainty associated with GIA. This study about Antarctic  $\Delta M$  is eventually important for future sea-level projection. The major findings of this study are as follows:

1. Precipitation accumulation anomaly (e.g., SMB) over Antarctica has contributed to the ice mass loss acceleration significantly during the last four decades (Chapter 3). It is found that such SMB variability has been largely attributed to the Southern Annular Mode. The SMB accounts for the annual to inter-annual variability of Antarctic ice mass change. In particular, inter-annual variation in SMB can explain an abrupt ice mass loss in Antarctica at 2007. The ice discharge estimated by subtracting the SMB from ice mass change shows a steady increase.

2. This study developed the revised CLD method which provides improved mass change data by using GRACE to constrain satellite altimetry data as an *a priori* (Chapter 4). The CLD estimates provides higher spatial resolution ( $\sim 27\text{km}$ ) than GRACE (hundreds of km) and suppress spatial leakage. The ice mass change anomalies occurring at glacial scales agree well with those from the Input-Output method.

3. A comparison of the mass change between SMB models and the revised CLD suggests that the GIA mass rate beneath the KIS should be negligible. Most GIA models, however, estimate the largest GIA rate over the KIS region in Antarctica. A GIA model of Caron and Ivins (2019) shows the minimum rate ( $3.0 \text{ Gton yr}^{-1}$ ) among other GIA models.

4. The future sea-level rise in 2100 projected by the current rate of ice mass change (about 24 cm) would be overestimated. The sea-level rise projection based on Antarctic ice discharge is about 16cm. Of these, the Thwaites and Pine Island Glaciers would contribute about 1.6 cm and 2.8 cm, respectively.

This dissertation includes several implications that should be addressed in

future studies. First, the SMB study shows that the Antarctic precipitation has not increased over the past 40 years despite global climate warming (Chapter 3). This is probably because the SAM has played a superior role in the changes in precipitation during the same period. On the other hand, a number of existing climate prediction models have suggested an increase in precipitation during the historical period. Since predictions from falsely constrained climate models may include high uncertainty, further studies should be made to improve accuracy of climate models to reflect the present-day SMB variability.

The revised CLD was used to combine GRACE and satellite altimetry data to generate high-resolution Antarctic ice mass change data (Chapter 4). It is expected that the method would not be limited to the application of Antarctic ice mass change. If any a priori information is available at study area, the revised CLD could be used to improve the spatial resolution of GRACE observations over those regions such as the Greenland Ice Sheet or alpine glaciers.

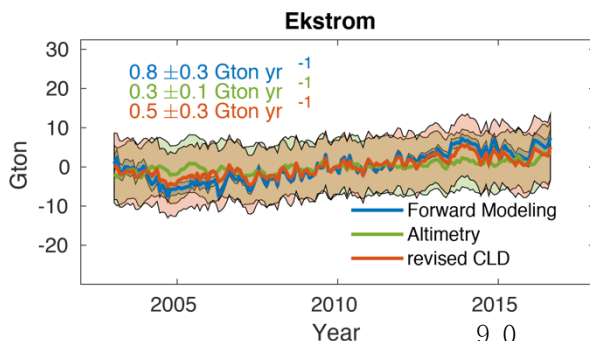
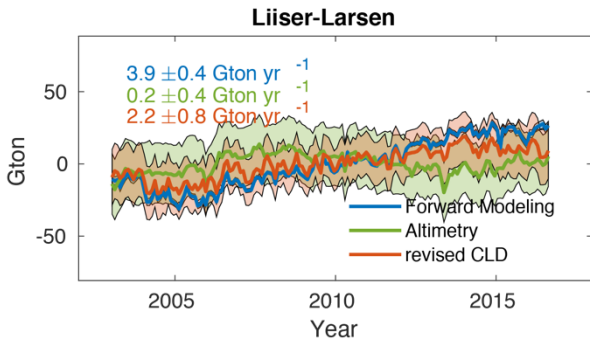
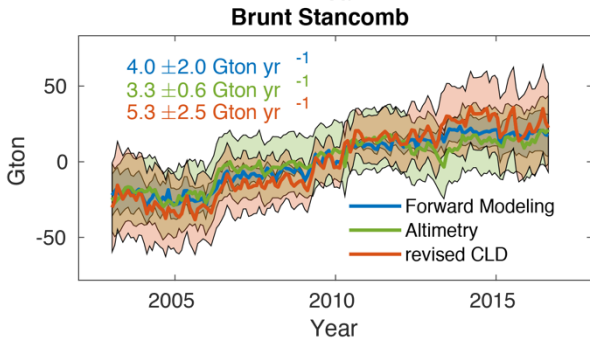
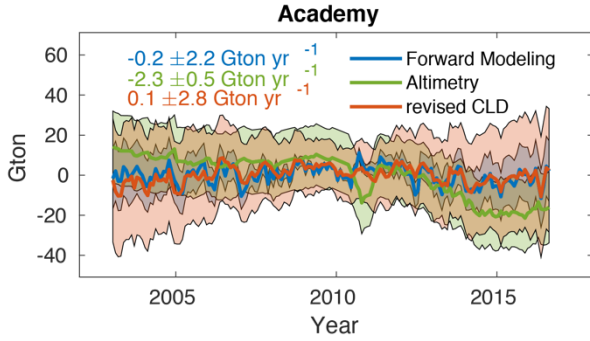
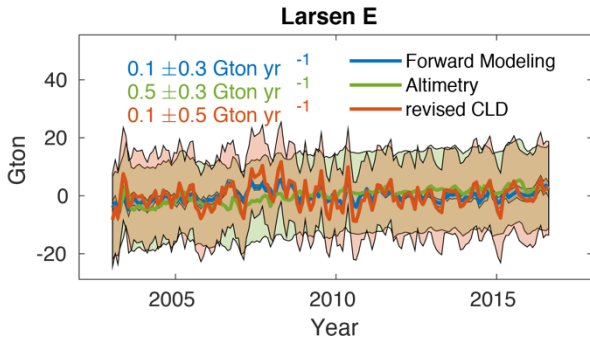
Validation of GIA models with high-resolution Antarctic ice mass change (Chapter 5) suggests that a number of GIA models would overestimate the solid earth's uplift rate beneath the KIS. Even though this examination was only carried out in a single ice stream region, the method can be extended to other glaciers to understand the Antarctic GIA effect if accurate estimations of glacier mass changes using the Input and Output method are available.

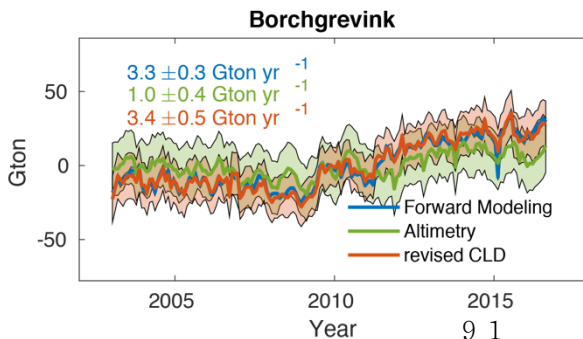
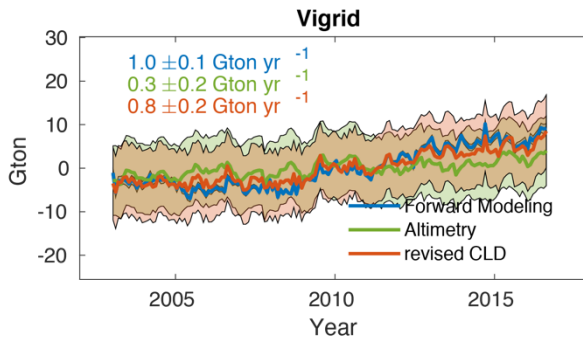
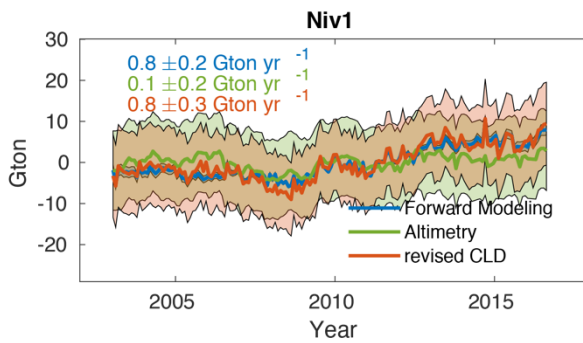
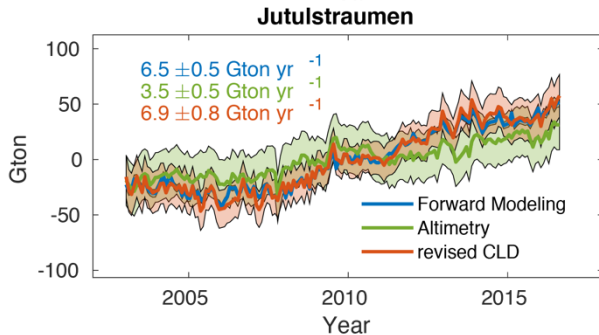
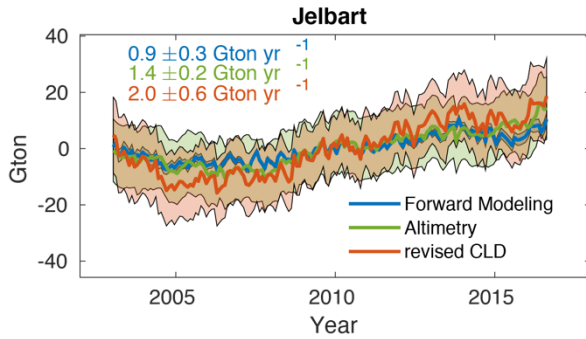
Those findings and new methods developed here are important to project future sea-level change empirically. Correcting SMB contributions from high-resolution ice mass change, glacier scale ice discharge variations were estimated. Because ice discharge variations have multi-decadal and longer variations, such variation are important to understand future ice mass change and consequently sea-level variations. The sea-level change projection based on the contemporary ice discharge variations underestimates the future sea-level rise compared to that based on the ice mass change (Chapter 6). This is because the current ice mass change includes apparent ice mass loss acceleration due to the decrease in Antarctic

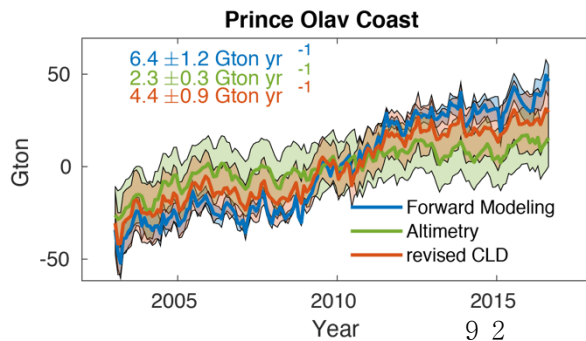
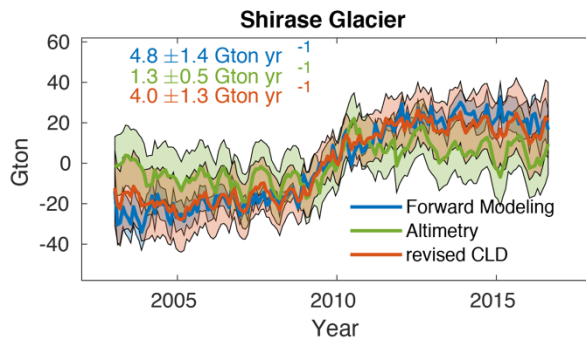
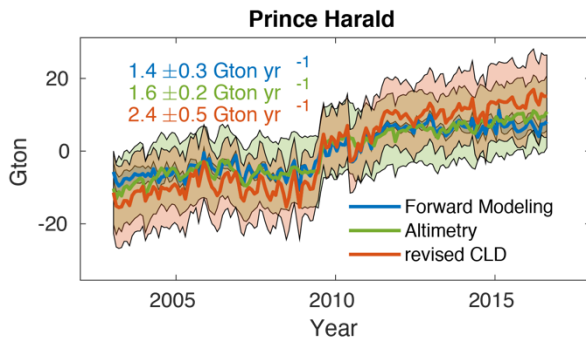
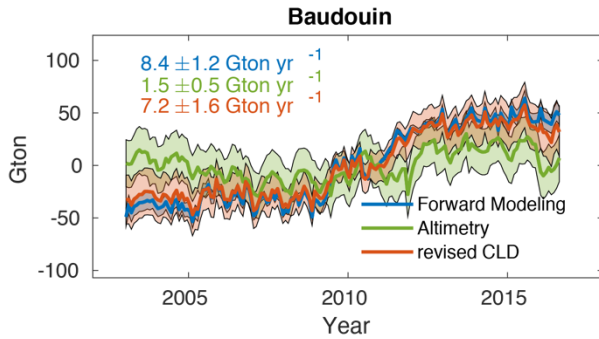
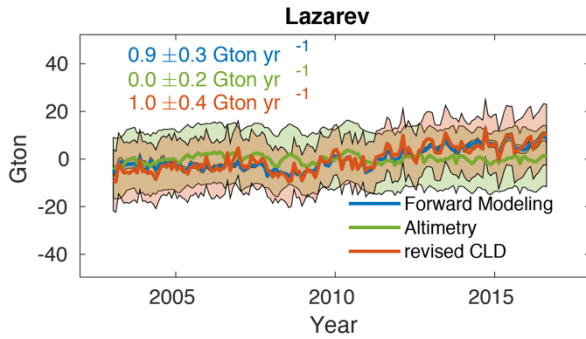
precipitation in recent decades (Chapter 3). Such SMB effect would not continue for the next decades because, as mentioned earlier, climate models predict that the Antarctic precipitation would gradually increase due to climate warming. The increase in SMB will add more ice to Antarctic Ice Sheet, which further suppresses the global sea-level rise. As a result, considering the future SMB effect, our projections proposed in Chapter 6 using only ice discharge variabilities might still overestimate the contribution of Antarctic ice mass change to future sea-level rise.

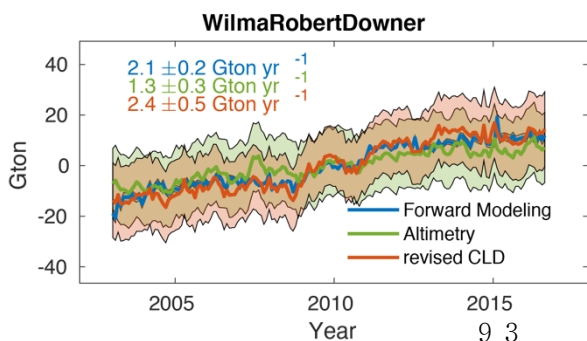
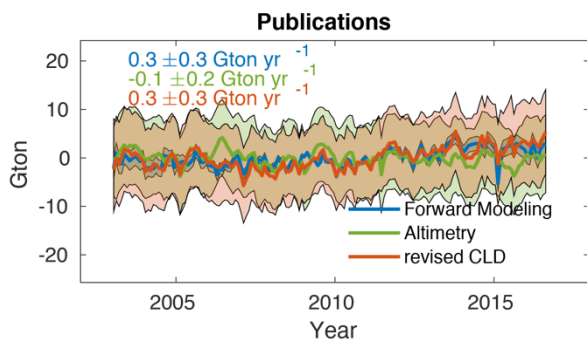
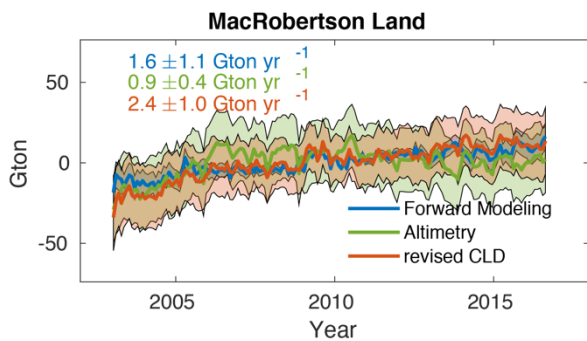
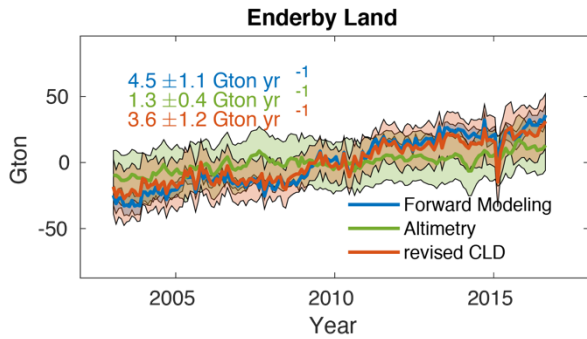
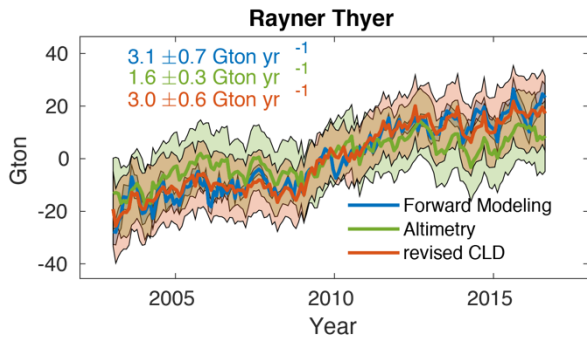
## **Appendix**

The following figures show mass changes of Antarctic glaciers jointly estimated by satellite gravimetry and altimetry. For comparison, the mass variations observed alone by satellite gravimetry and altimetry are presented together. The basin boundaries of Antarctic glaciers are obtained from Mouginot et al. (2017). Given the effective spatial resolution of estimated mass anomalies, only glaciers larger than 8000 km<sup>2</sup> (corresponding to 10 grid pixels in 27km spatial resolution) were considered.

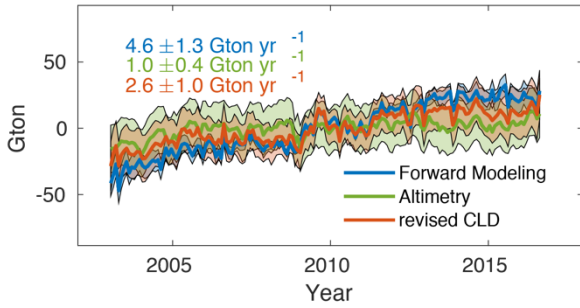




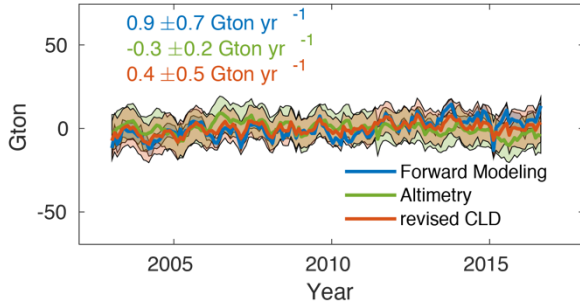




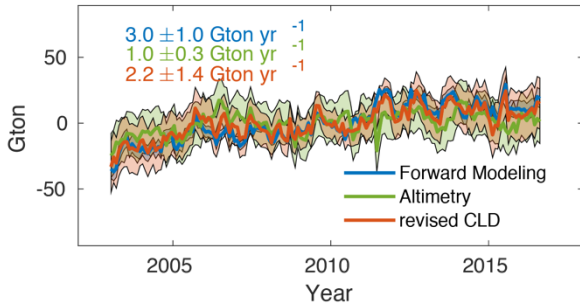
### Mawson Coast



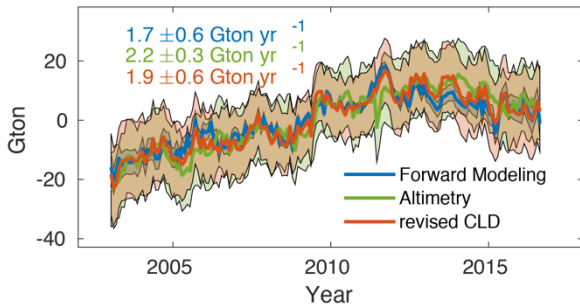
### Ingrid Christensen Coast



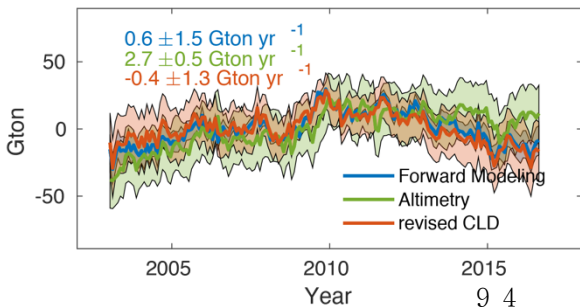
### Leopold and Astrid Coast

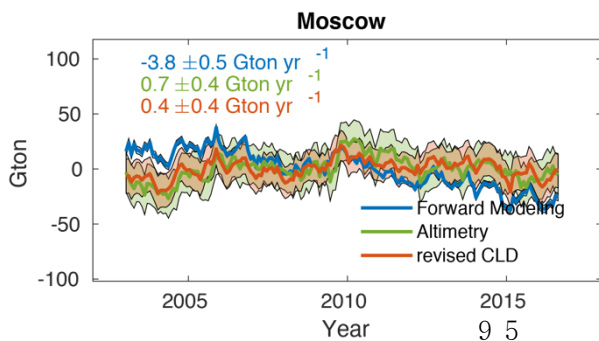
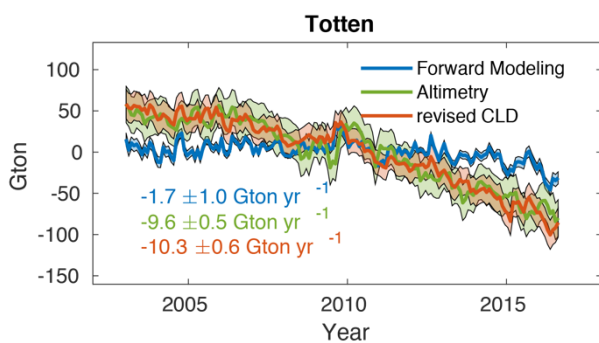
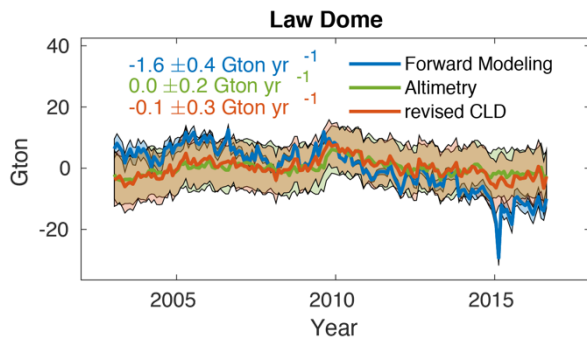
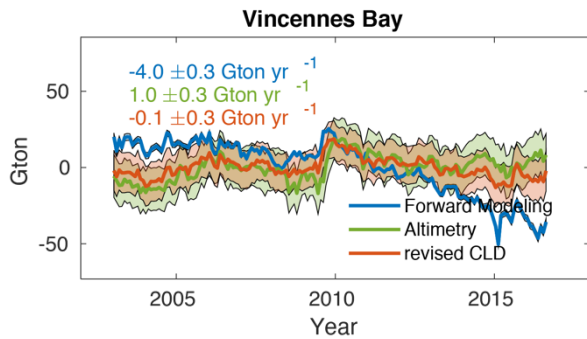
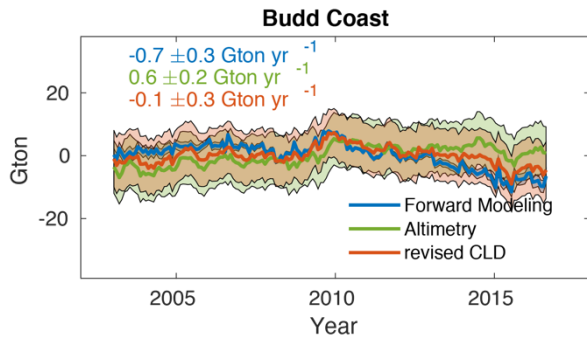


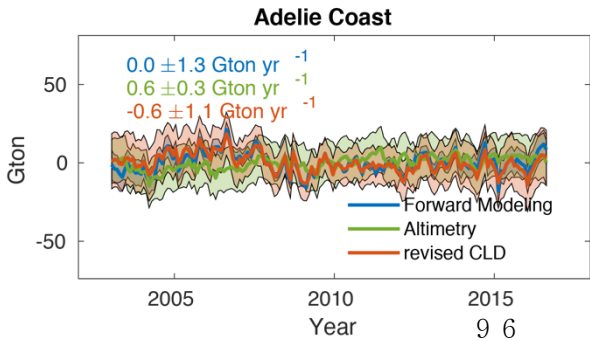
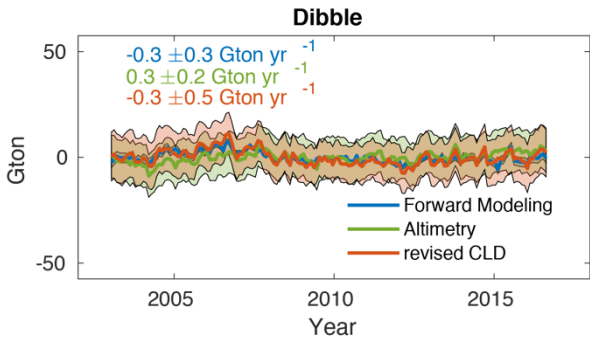
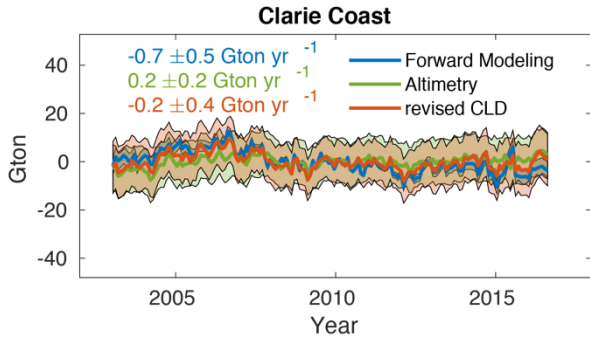
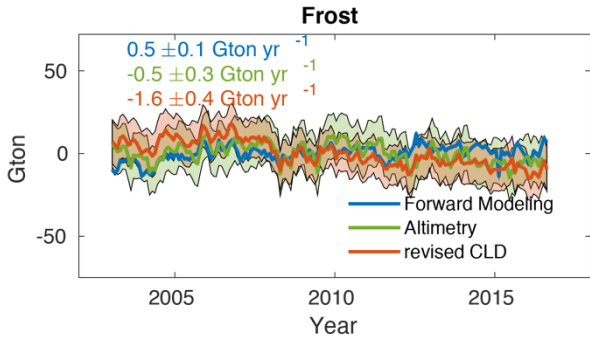
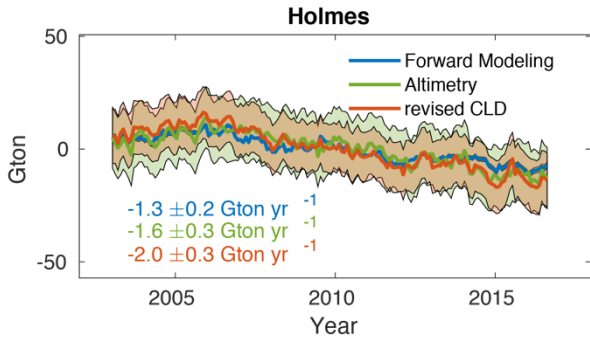
### Wilhelm II Coast

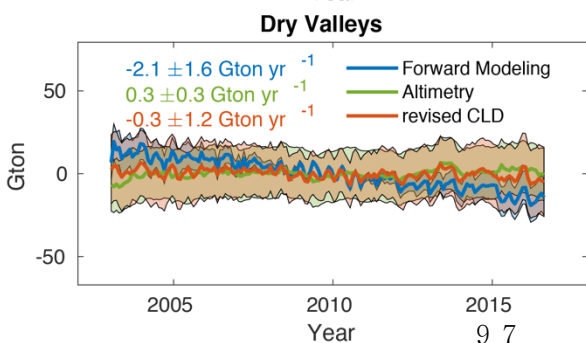
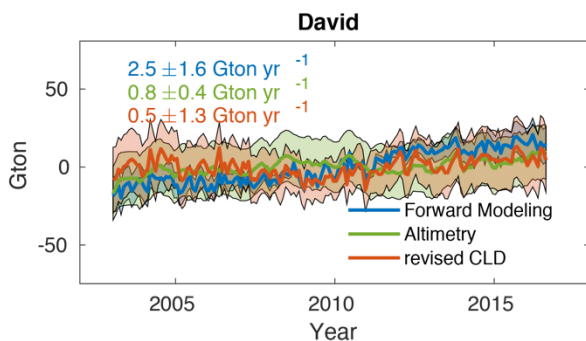
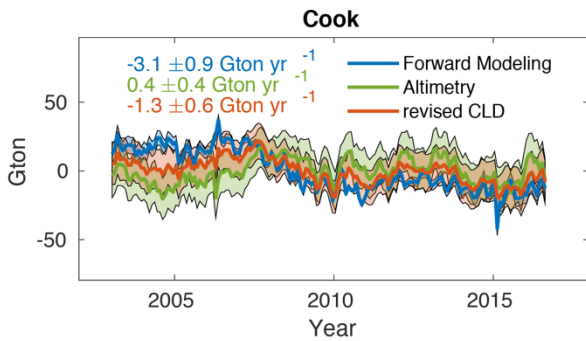
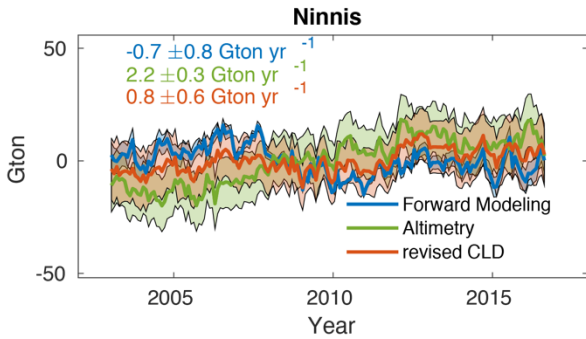
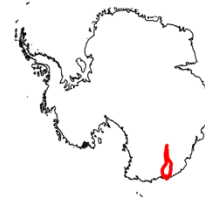
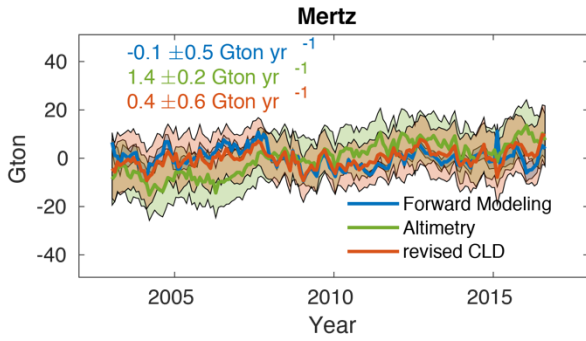


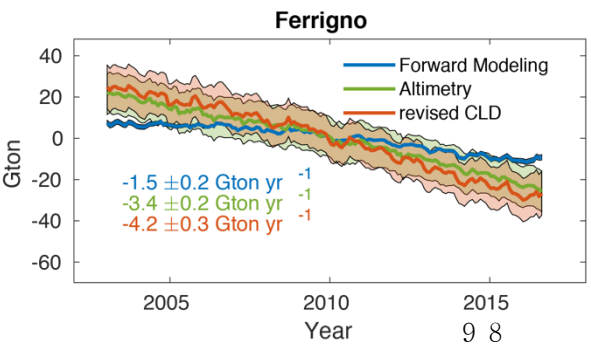
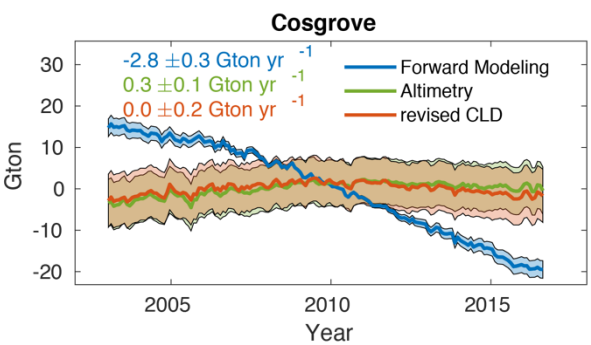
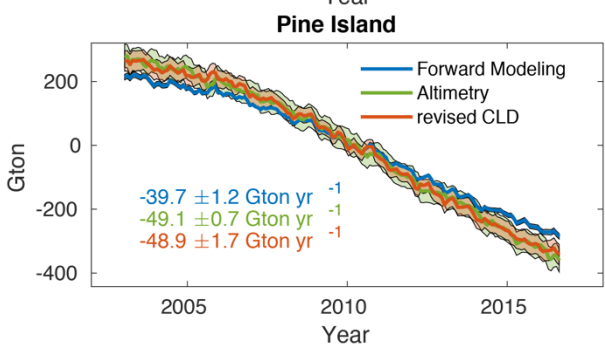
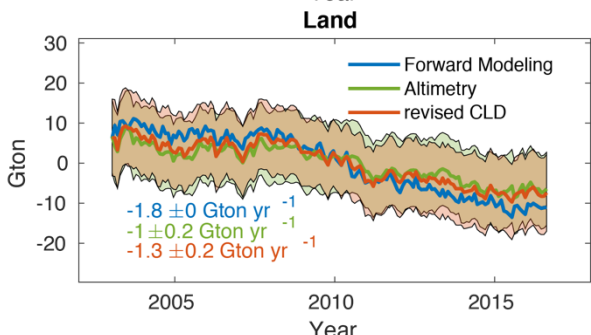
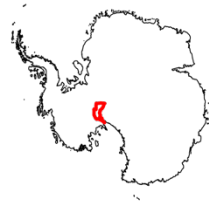
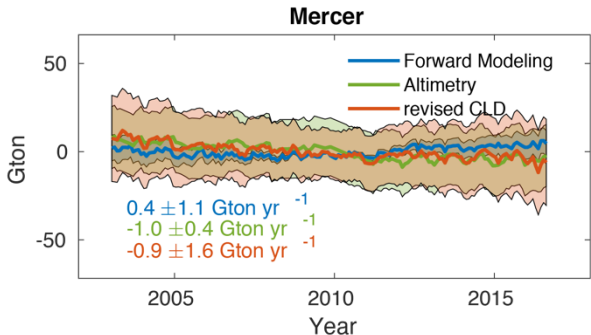
### Denman Scott

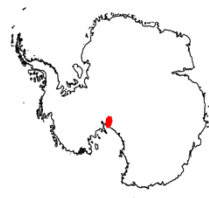
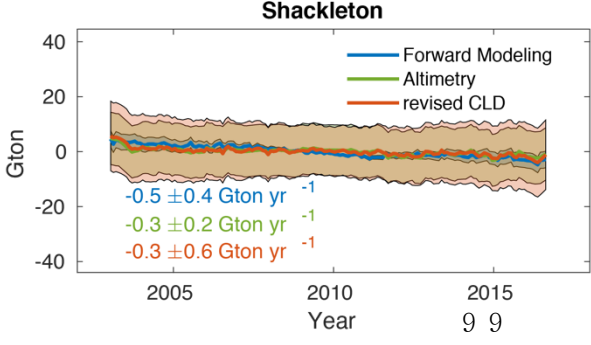
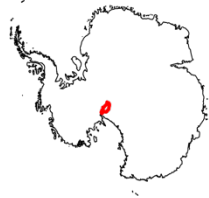
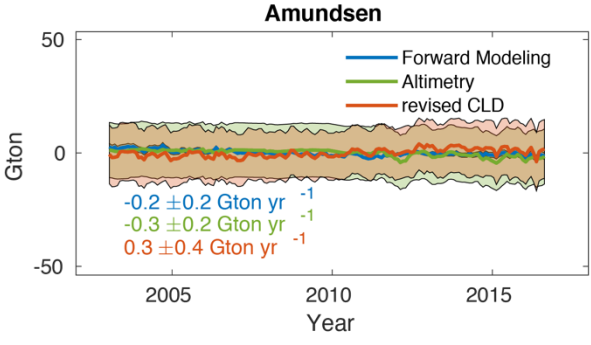
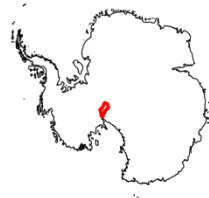
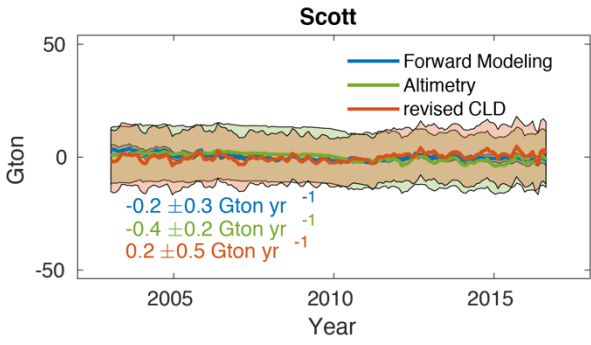
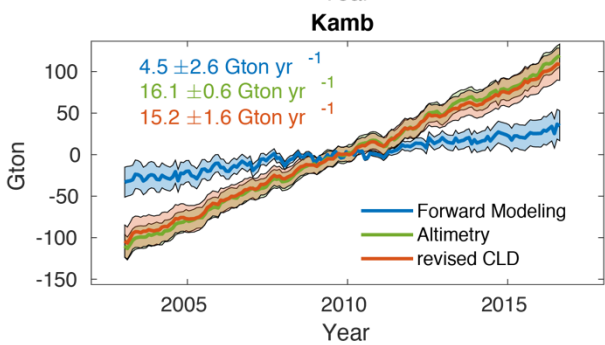
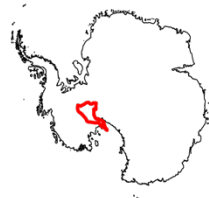
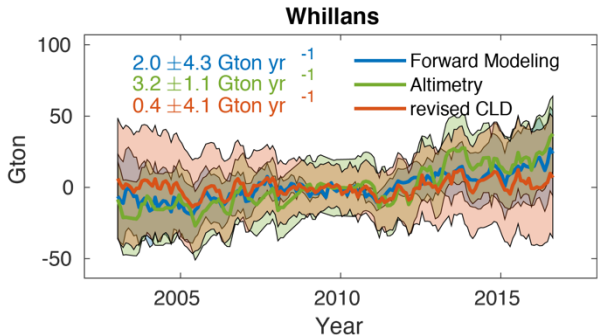


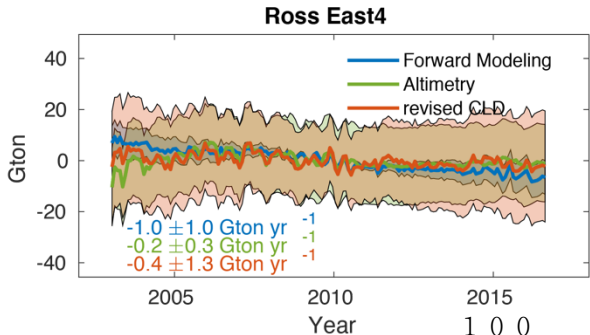
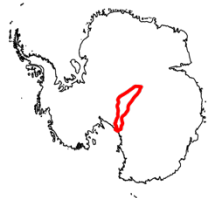
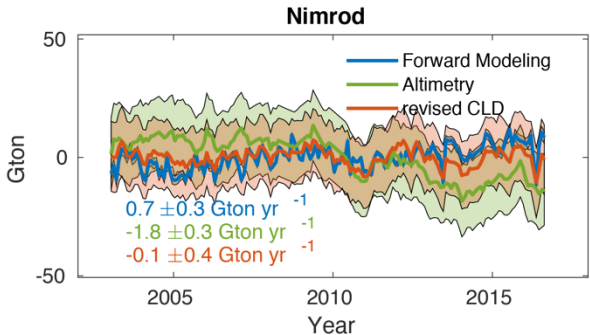
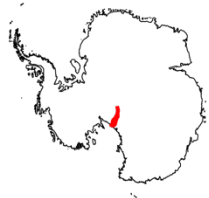
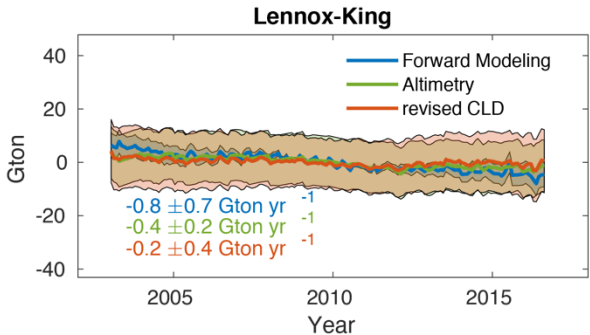
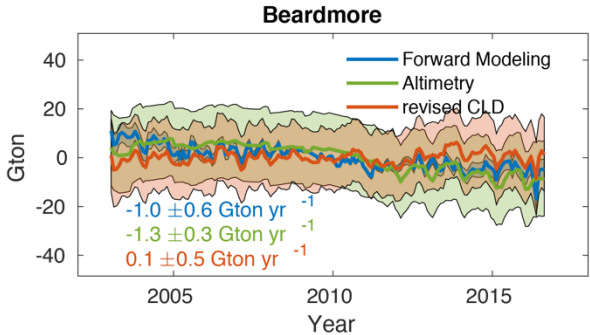
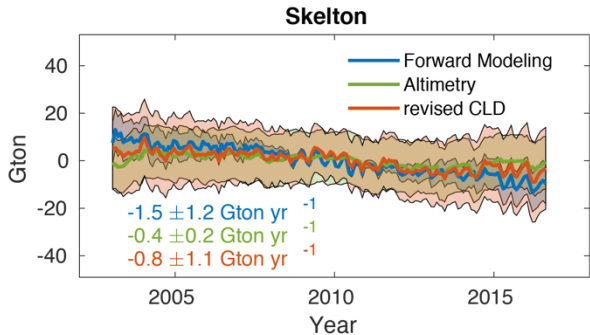


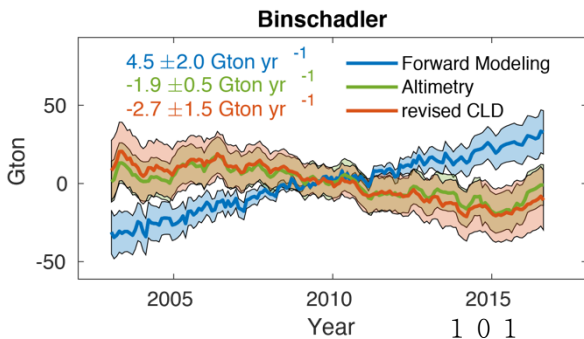
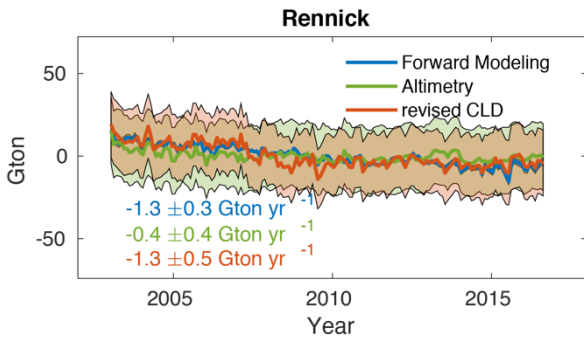
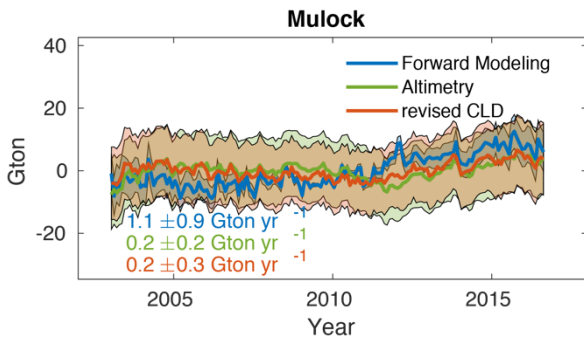
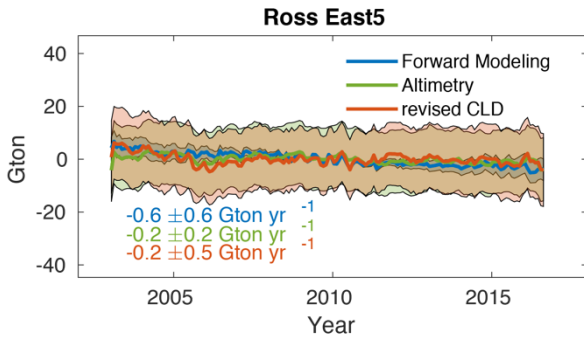
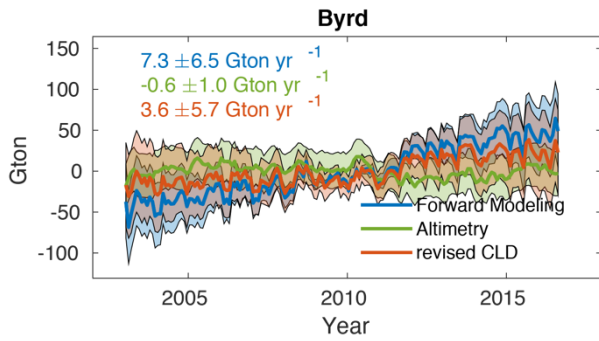


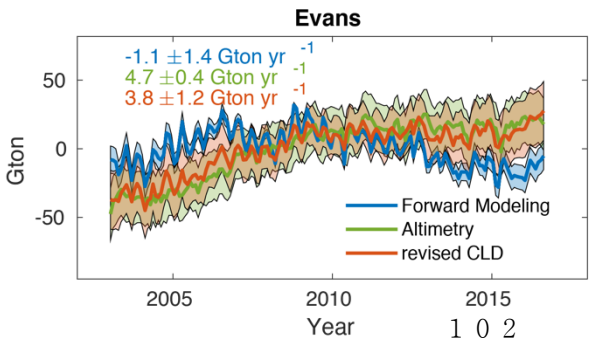
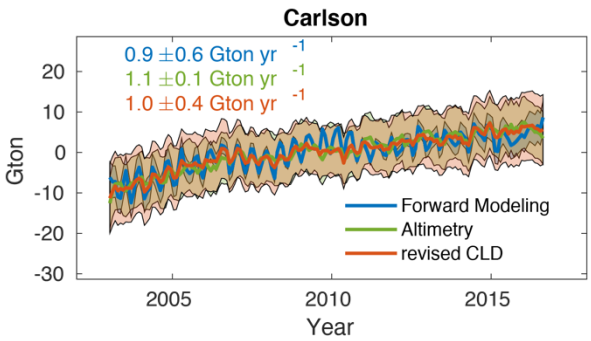
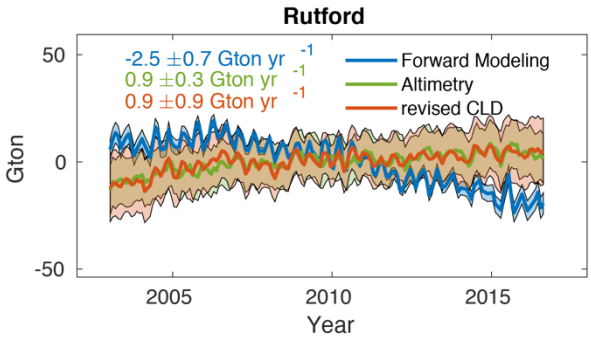
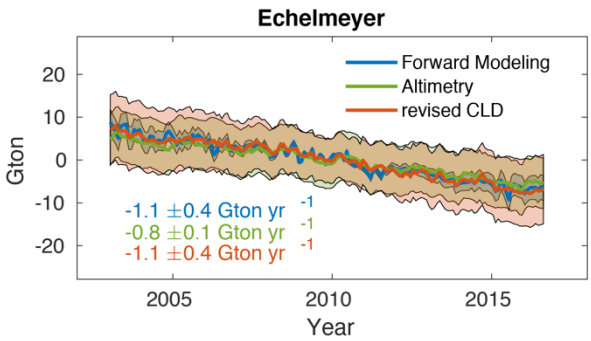
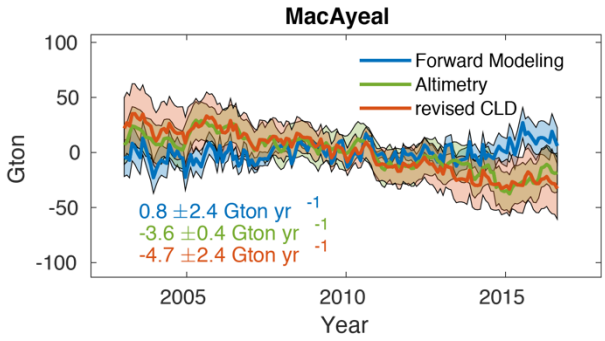


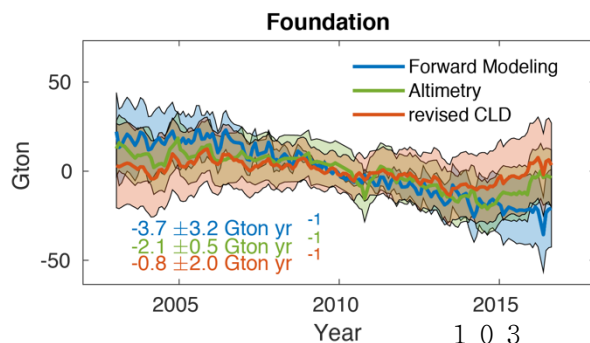
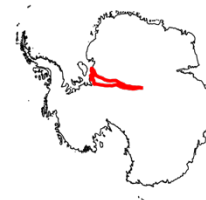
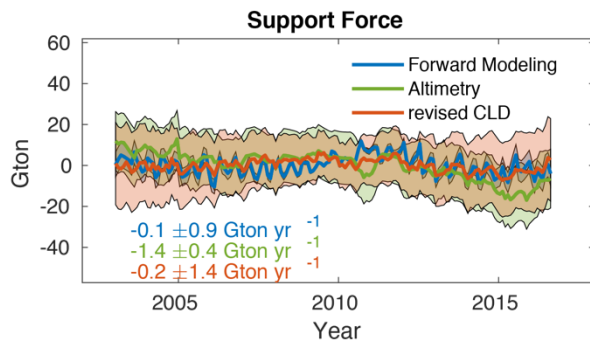
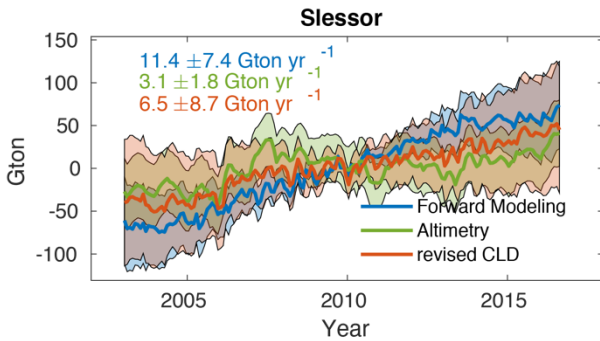
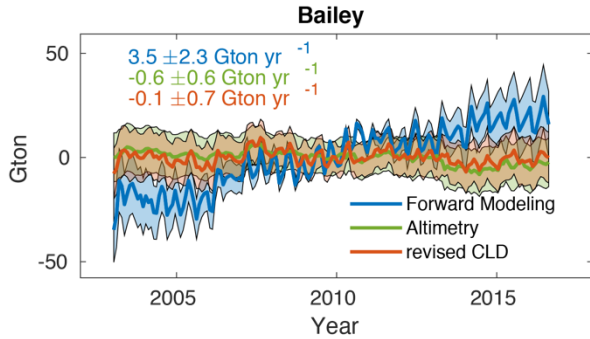
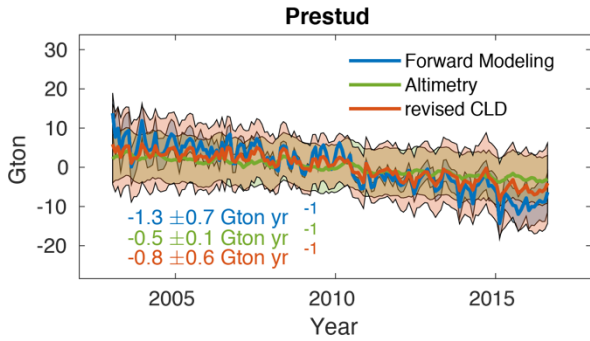


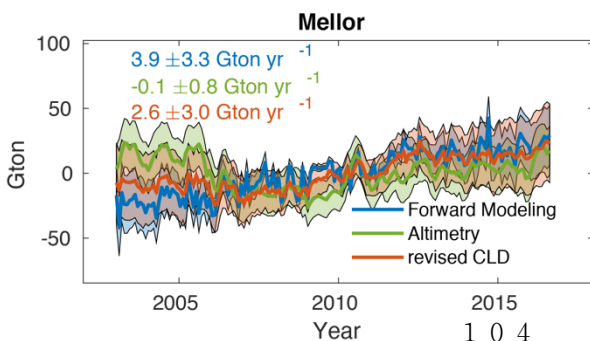
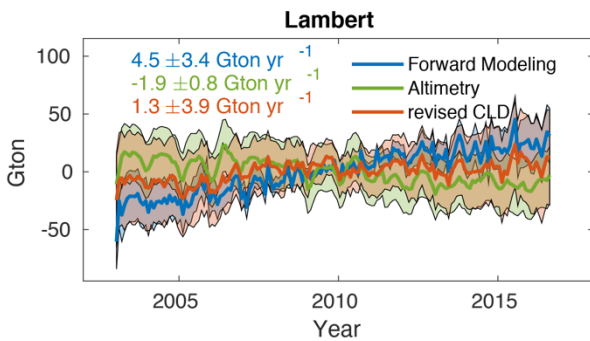
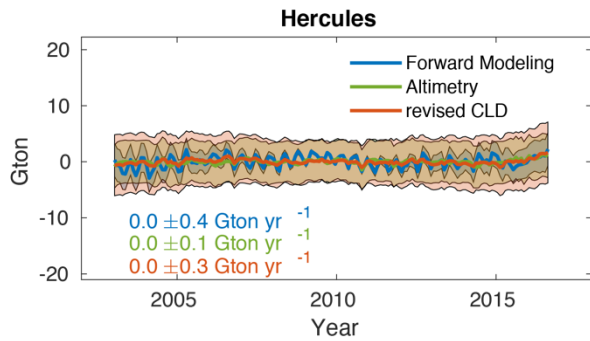
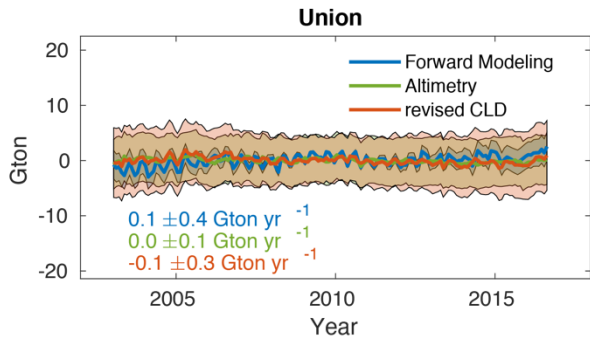
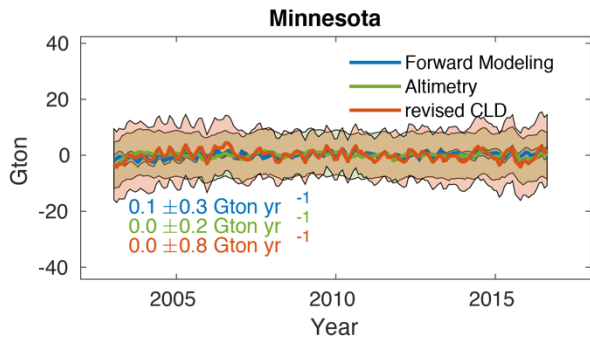


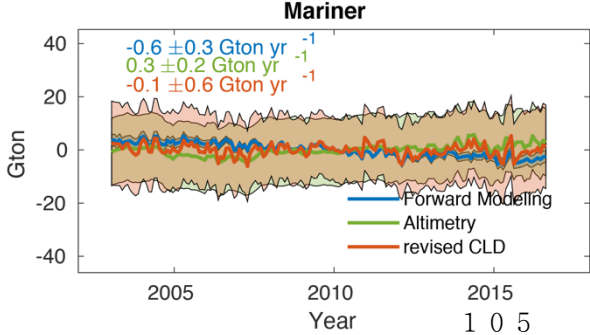
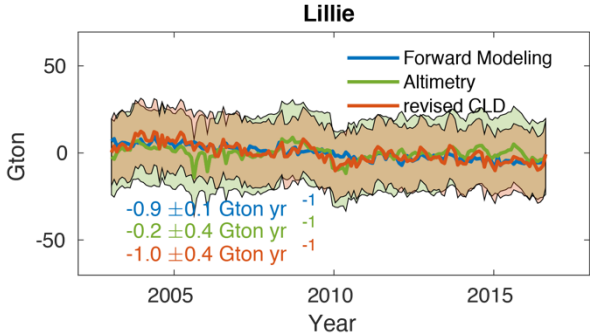
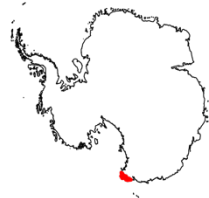
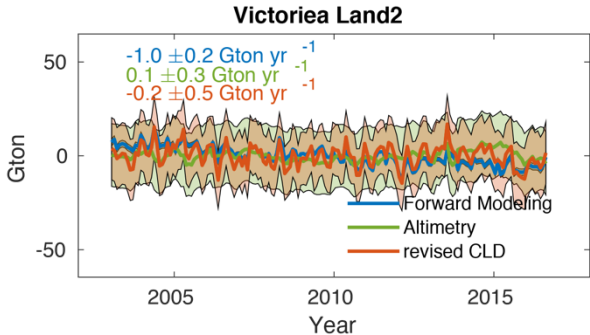
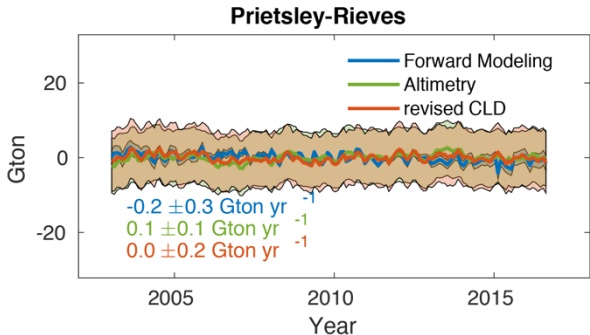
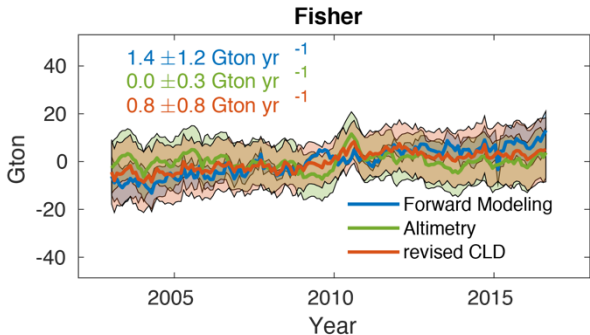


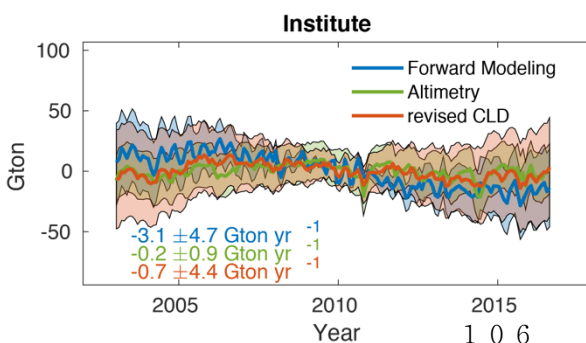
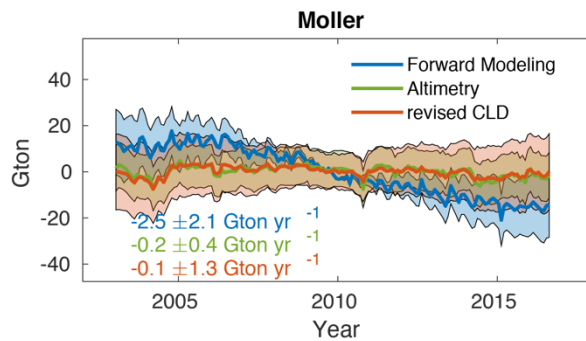
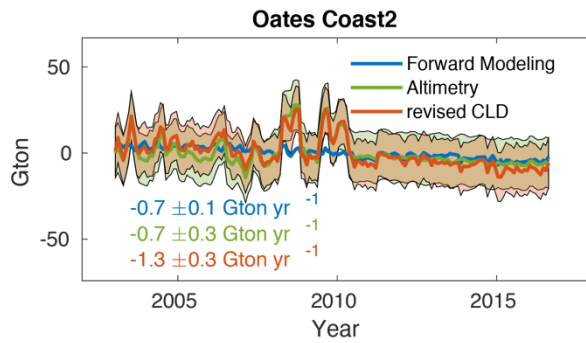
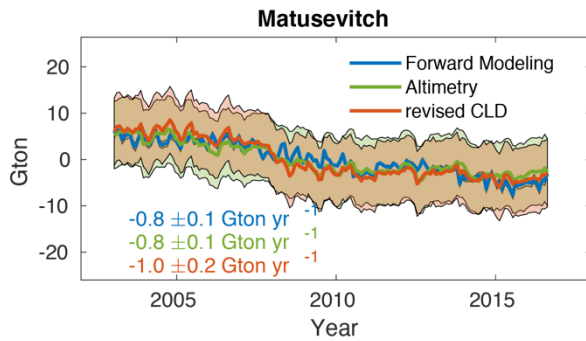
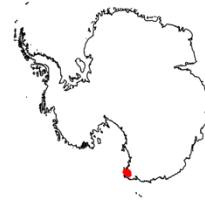
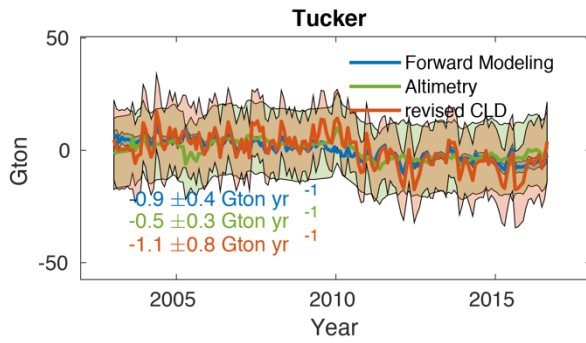


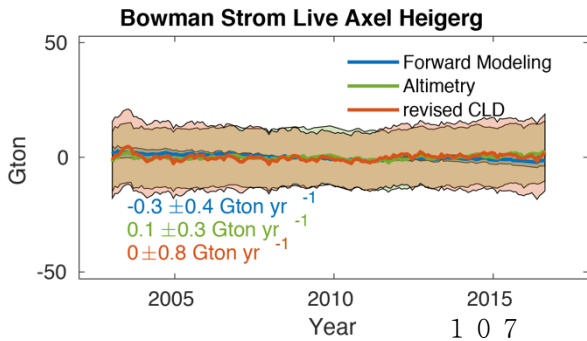
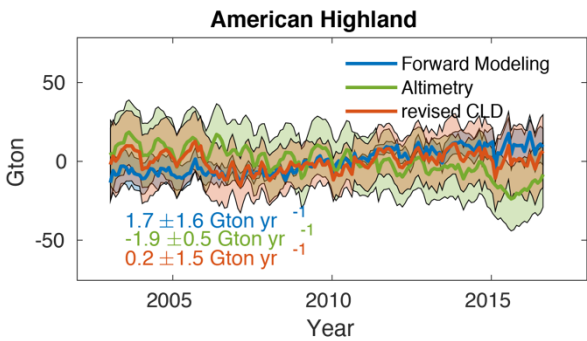
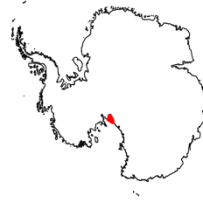
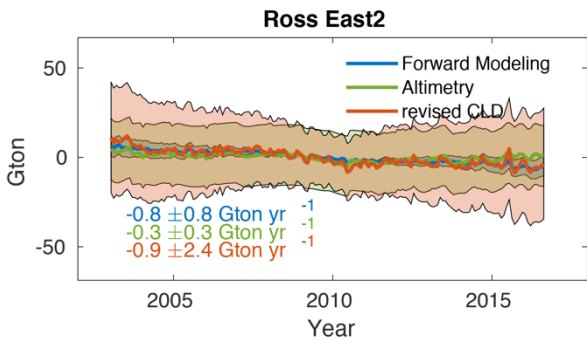
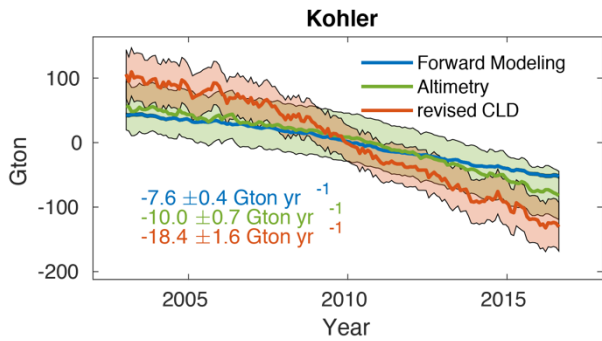
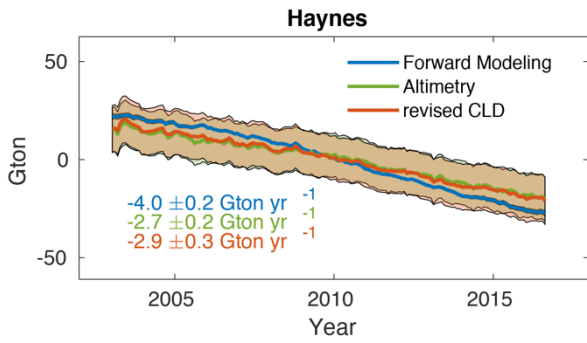


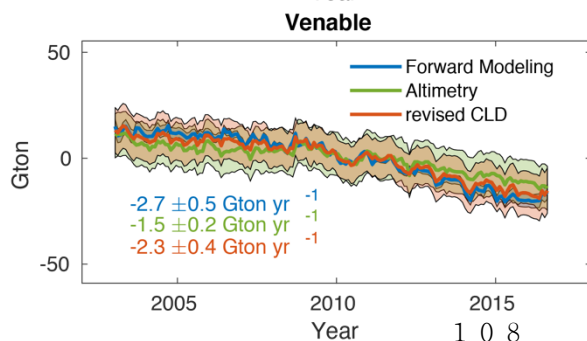
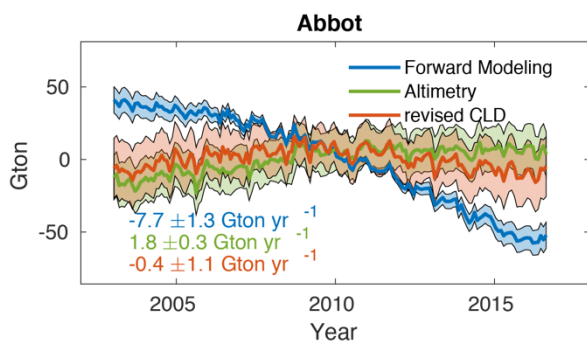
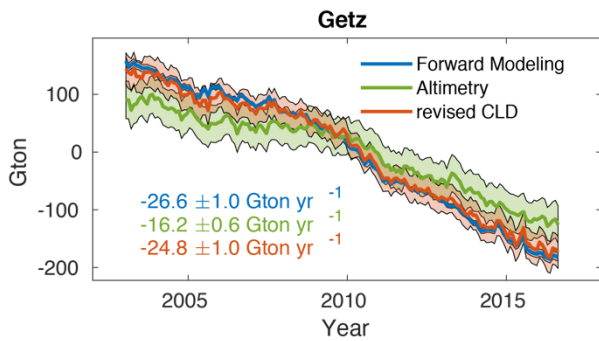
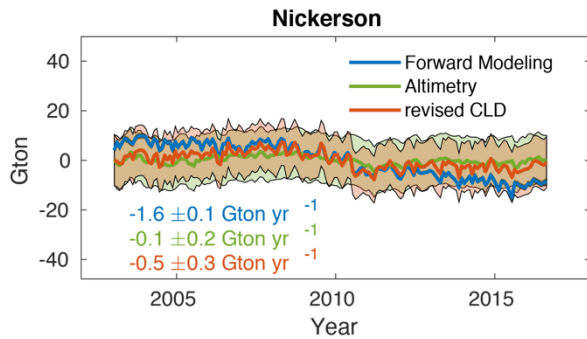
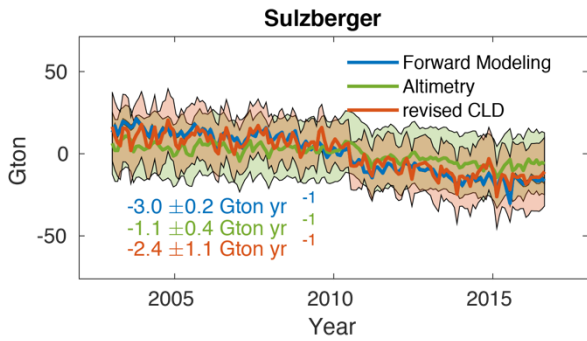


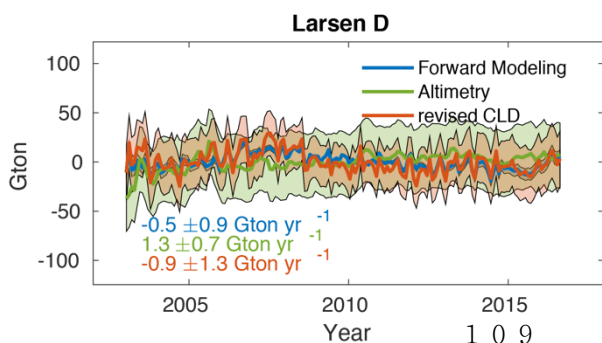
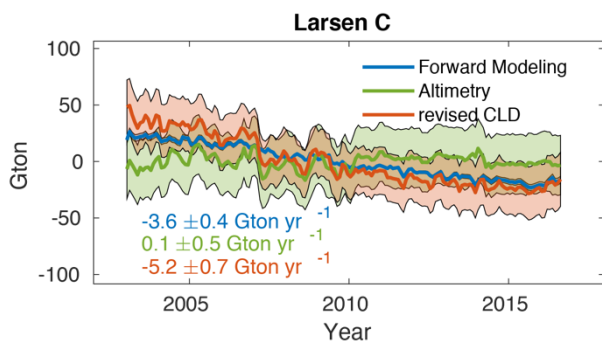
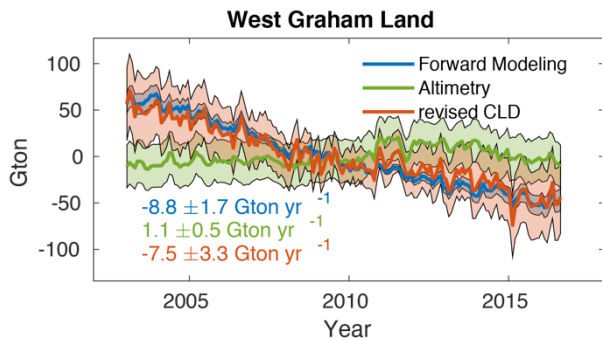
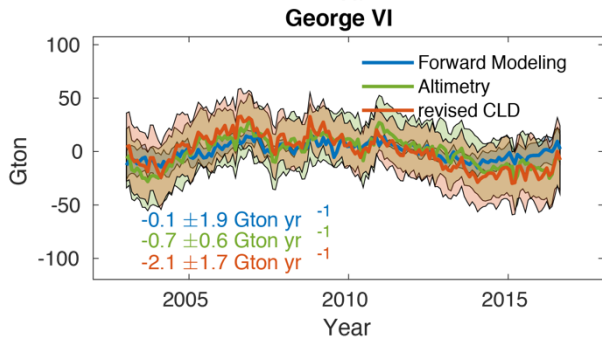
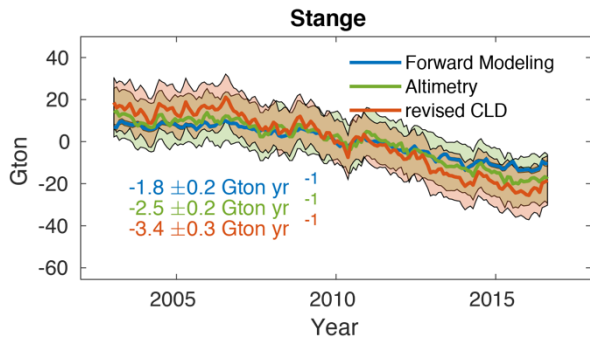




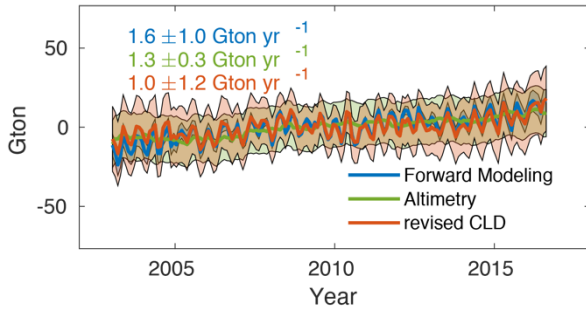




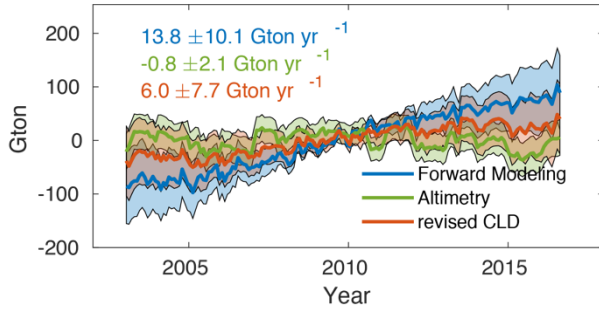




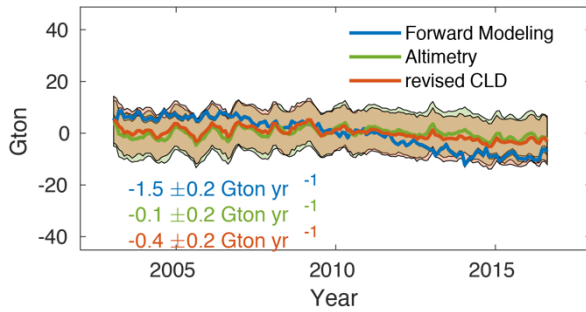
### D Orville Coast



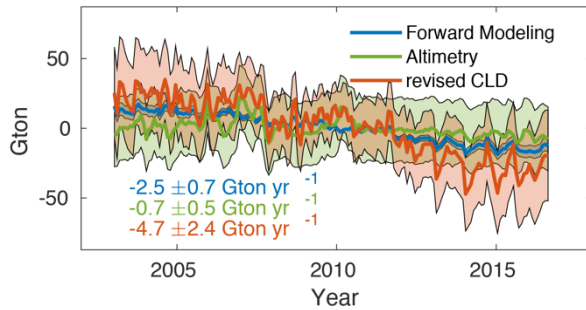
### Recovery



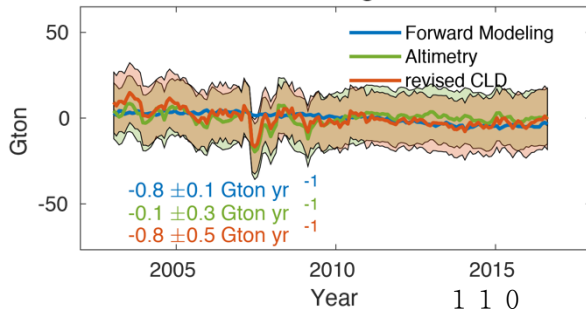
### Bach

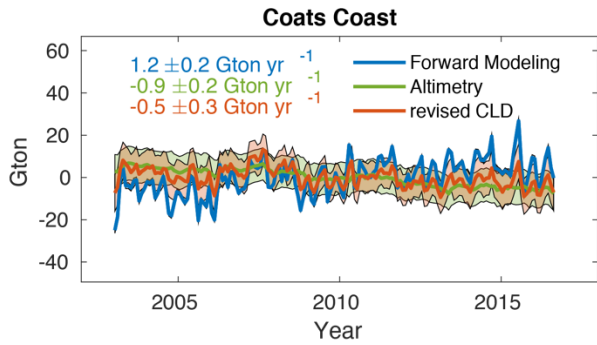
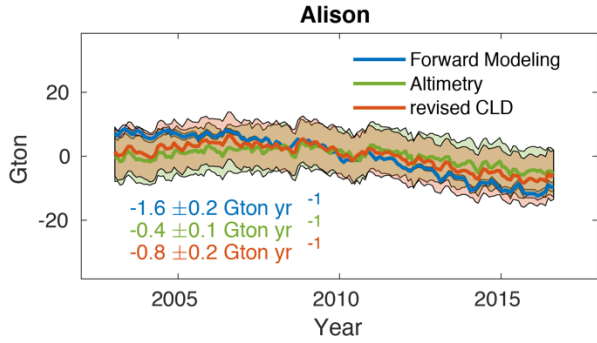
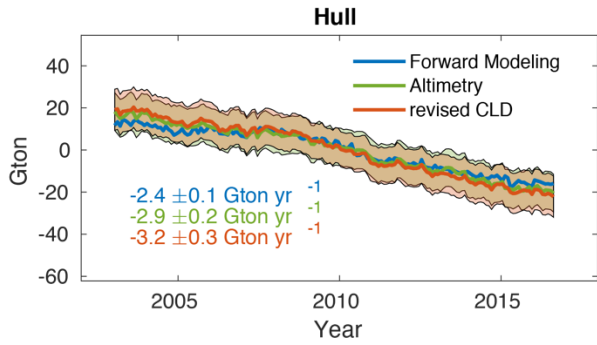
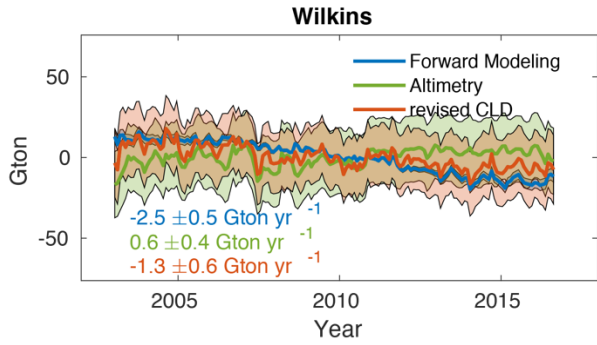


### Wilkins Island4



### Wilkins George VI





## References

- A, G., Wahr, J., & Zhong, S. (2012). Computations of the viscoelastic response of a 3-D compressible Earth to surface loading: an application to Glacial Isostatic Adjustment in Antarctica and Canada. *Geophysical Journal International*, *192*(2), 557-572.
- Adhikari, S., Ivins, E. R., Frederikse, T., Landerer, F. W., & Caron, L. (2019). Sea-level fingerprints emergent from GRACE mission data. *Earth System Science Data*, *11*(2), 629-646.
- Agosta, C., Amory, C., Kittel, C., Orsi, A., Favier, V., Gallée, H., et al. (2019). Estimation of the Antarctic surface mass balance using the regional climate model MAR (1979–2015) and identification of dominant processes. *The Cryosphere*, *13*(1), 281-296.
- al., S. e. (2018). Mass balance of the Antarctic Ice Sheet from 1992 to 2017. *Nature*, *558*(7709), 219-222. <https://www.ncbi.nlm.nih.gov/pubmed/29899482>
- Alley, R. B., Anandakrishnan, S., Bentley, C. R., & Lord, N. (1994). A water-piracy hypothesis for the stagnation of Ice Stream C, Antarctica. *Annals of Glaciology*, *20*(1), 187-194.
- Boening, C., Lebrock, M., Landerer, F., & Stephens, G. (2012). Snowfall-driven mass change on the East Antarctic ice sheet. *Geophysical Research Letters*, *39*(21).
- Bromwich, D. H., Nicolas, J. P., & Monaghan, A. J. (2011). An Assessment of Precipitation Changes over Antarctica and the Southern Ocean since 1989 in Contemporary Global Reanalyses\*. *Journal of Climate*, *24*(16), 4189-4209.
- Bromwich, D. H., Rogers, A. N., Kållberg, P., Cullather, R. I., White, J. W. C., & Kreutz, K. J. (2000). ECMWF Analyses and Reanalyses Depiction of ENSO Signal in Antarctic Precipitation\*. *Journal of Climate*, *13*(8), 1406-1420.
- Caron, L., & Ivins, E. R. (2019). A baseline Antarctic GIA correction for space gravimetry. *Earth and Planetary Science Letters*, *531*.
- Cazenave et al. (2018). Global sea-level budget 1993–present. *Earth System Science Data*, *10*(3), 1551-1590.
- Chen, J. L., Wilson, C. R., Blankenship, D., & Tapley, B. D. (2009). Accelerated

- Antarctic ice loss from satellite gravity measurements. *Nature Geoscience*, 2(12), 859-862. <Go to ISI>://WOS:000272239400019
- Chen, J. L., Wilson, C. R., Li, J., & Zhang, Z. (2015). Reducing leakage error in GRACE-observed long-term ice mass change: a case study in West Antarctica. *Journal of Geodesy*, 89(9), 925-940.
- Chen, J. L., Wilson, C. R., Tapley, B. D., Blankenship, D. D., & Ivins, E. R. (2007). Patagonia Icefield melting observed by Gravity Recovery and Climate Experiment (GRACE). *Geophysical Research Letters*, 34(22).
- Chen, J. L., Wilson, C. R., Tapley, B. D., & Grand, S. (2007). GRACE detects coseismic and postseismic deformation from the Sumatra-Andaman earthquake. *Geophysical Research Letters*, 34(13).
- DeConto, R. M., Pollard, D., Alley, R. B., Velicogna, I., Gasson, E., Gomez, N., et al. (2021). The Paris Climate Agreement and future sea-level rise from Antarctica. *Nature*, 593(7857), 83-89. <https://www.ncbi.nlm.nih.gov/pubmed/33953408>
- Dee, D. P., Uppala, S. M., Simmons, A. J., Berrisford, P., Poli, P., Kobayashi, S., et al. (2011). The ERA-Interim reanalysis: configuration and performance of the data assimilation system. *Quarterly Journal of the Royal Meteorological Society*, 137(656), 553-597. <Go to ISI>://WOS:000290450900001
- Dutrieux, P., De Rydt, J., Jenkins, A., Holland, P. R., Ha, H. K., Lee, S. H., et al. (2014). Strong sensitivity of Pine Island ice-shelf melting to climatic variability. *Science*, 343(6167), 174-178. <https://www.ncbi.nlm.nih.gov/pubmed/24385606>
- Eom, J., Seo, K.-W., & Ryu, D. (2017). Estimation of Amazon River discharge based on EOF analysis of GRACE gravity data. *Remote Sensing of Environment*, 191, 55-66.
- Forsberg, R., Sørensen, L., & Simonsen, S. (2017). Greenland and Antarctica Ice Sheet Mass Changes and Effects on Global Sea Level. *Surveys in Geophysics*, 38(1), 89-104.
- Fretwell, P., Pritchard, H. D., Vaughan, D. G., Bamber, J. L., Barrand, N. E., Bell, R., et al. (2013). Bedmap2: improved ice bed, surface and thickness datasets for Antarctica. *Cryosphere*, 7(1), 375-393. <Go to ISI>://WOS:000317005200007

- Genthon, C., Krinner, G., & Sacchetti, M. (2003). Interannual Antarctic tropospheric circulation and precipitation variability. *Climate Dynamics*, 21(3-4), 289-307. <Go to ISI>://WOS:000185228700006
- Harman, H. H. (1976). *Modern factor analysis* (3 ed.).
- Held, I. M., & Soden, B. J. (2006). Robust Responses of the Hydrological Cycle to Global Warming. *Journal of Climate*, 19(21), 5686-5699.
- Hersbach, H., Bell, W., Berrisford, P., Horányi, A., M-S, J., Nicolas, J., et al. (2019). Global reanalysis: goodbye ERA-Interim, hello ERA5. *ECMWF Newsletter*, 159, 17-24.
- Hersbach, H., Bell, W., Berrisford, P., Horányi, A., J., M.-S., Nicholas, J., et al. (2019). Global reanalysis: goodbye ERA-Interim, hello ERA5. *ECMWF Newsletter*(159), 17-24.
- Hofman, M. A., Luthcke, S. B., & Blair, J. B. (2013). Estimation of ICESat intercampaign elevation biases from comparison of lidar data in East Antarctica. *Geophysical Research Letters*, 40(21), 5698-5703.
- Jekeli, C. (1981). *Alternative methods to smooth the Earth's gravity field*, Rep. 327. Retrieved from
- Jeon, T., Seo, K. W., Youm, K., Chen, J., & Wilson, C. R. (2018). Global sea level change signatures observed by GRACE satellite gravimetry. *Sci Rep*, 8(1), 13519. <https://www.ncbi.nlm.nih.gov/pubmed/30202083>
- Jevrejeva, S., Moore, J. C., Grinsted, A., Matthews, A. P., & Spada, G. (2014). Trends and acceleration in global and regional sea levels since 1807. *Global and Planetary Change*, 113, 11-22.
- Joughin, I., Bindschadler, R. A., King, M. A., Voigt, D., Alley, R. B., Anandakrishnan, S., et al. (2005). Continued deceleration of Whillans Ice Stream, West Antarctica. *Geophysical Research Letters*, 32(22).
- Kim, B.-H., Eom, J., Seo, K.-W., & Wilson, C. R. (2016). Spurious barometric pressure acceleration in Antarctica and propagation into GRACE Antarctic mass change estimates. *Geophysical Journal International*, 206(2), 1306-1314.
- Kim, J. S., Seo, K. W., Jeon, T., Chen, J., & Wilson, C. R. (2019). Missing Hydrological Contribution to Sea Level Rise. *Geophysical Research Letters*, 46(21), 12049-12055.

- Konrad, H., Gilbert, L., Cornford, S. L., Payne, A., Hogg, A., Muir, A., & Shepherd, A. (2017). Uneven onset and pace of ice-dynamical imbalance in the Amundsen Sea Embayment, West Antarctica. *Geophysical Research Letters*, *44*(2), 910-918.
- Konrad, H., Shepherd, A., Gilbert, L., Hogg, A. E., McMillan, M., Muir, A., & Slater, T. (2018). Net retreat of Antarctic glacier grounding lines. *Nature Geoscience*, *11*(4), 258-262.
- Kopp, R. E., DeConto, R. M., Bader, D. A., Hay, C. C., Horton, R. M., Kulp, S., et al. (2017). Evolving Understanding of Antarctic Ice-Sheet Physics and Ambiguity in Probabilistic Sea-Level Projections. *Earth's Future*, *5*(12), 1217-1233.
- Kusche, J. (2007). Approximate decorrelation and non-isotropic smoothing of time-variable GRACE-type gravity field models. *Journal of Geodesy*, *81*(11), 733-749.
- Landerer, F. (2019). Monthly estimates of degree-1 (geocenter) gravity coefficients, generated from GRACE (04-2002 - 06/2017) and GRACE-FO (06/2018 onward) RL06 solutions, GRACE Technical Note 13, The GRACE Project, NASA Jet Propulsion Laboratory ([https://podaac-tools.jpl.nasa.gov/drive/files/allData/grace/docs/TN-13\\_GEOC\\_CSR\\_RL06.txt](https://podaac-tools.jpl.nasa.gov/drive/files/allData/grace/docs/TN-13_GEOC_CSR_RL06.txt)).
- Lenaerts, J. T. M., Medley, B., van den Broeke, M. R., & Wouters, B. (2019). Observing and Modeling Ice Sheet Surface Mass Balance. *Rev Geophys*, *57*(2), 376-420. <https://www.ncbi.nlm.nih.gov/pubmed/31598609>
- Lenaerts, J. T. M., van Meijgaard, E., van den Broeke, M. R., Ligtenberg, S. R. M., Horwath, M., & Isaksson, E. (2013). Recent snowfall anomalies in Dronning Maud Land, East Antarctica, in a historical and future climate perspective. *Geophysical Research Letters*, *40*(11), 2684-2688.
- Li, X., Rignot, E., Mouginot, J., & Scheuchl, B. (2016). Ice flow dynamics and mass loss of Totten Glacier, East Antarctica, from 1989 to 2015. *Geophysical Research Letters*, *43*(12), 6366-6373.
- Ligtenberg, S. R. M., Helsen, M. M., & van den Broeke, M. R. (2011). An improved semi-empirical model for the densification of Antarctic firn. *Cryosphere*, *5*(4), 809-819. <Go to ISI>://WOS:000298494200001

- Loomis, B. D., Rachlin, K. E., & Luthcke, S. B. (2019). Improved Earth Oblateness Rate Reveals Increased Ice Sheet Losses and Mass-Driven Sea Level Rise. *Geophysical Research Letters*, *46*(12), 6910-6917.
- Lyard, F., Lefevre, F., Letellier, T., & Francis, O. (2006). Modelling the global ocean tides: modern insights from FES2004. *Ocean Dynamics*, *56*(5-6), 394-415.
- Markus, T., Neumann, T., Martino, A., Abdalati, W., Brunt, K., Csatho, B., et al. (2017). The Ice, Cloud, and land Elevation Satellite-2 (ICESat-2): Science requirements, concept, and implementation. *Remote Sensing of Environment*, *190*, 260-273.
- McMillan, M., Shepherd, A., Sundal, A., Briggs, K., Muir, A., Ridout, A., et al. (2014). Increased ice losses from Antarctica detected by CryoSat-2. *Geophysical Research Letters*, *41*(11), 3899-3905. <Go to ISI>://WOS:000339280200030
- Medley, B., & Thomas, E. R. (2018). Increased snowfall over the Antarctic Ice Sheet mitigated twentieth-century sea-level rise. *Nature Climate Change*, *9*(1), 34-39.
- Menke, W. (2012). *Geophysical Data Analysis: Discrete Inverse Theory* (3rd ed.): Academic Press.
- Mohajerani, Y., Velicogna, I., & Rignot, E. (2018). Mass Loss of Totten and Moscow University Glaciers, East Antarctica, Using Regionally Optimized GRACE Mascons. *Geophysical Research Letters*, *45*(14), 7010-7018.
- Morlighem, M., Rignot, E., Binder, T., Blankenship, D., Drews, R., Eagles, G., et al. (2020). Deep glacial troughs and stabilizing ridges unveiled beneath the margins of the Antarctic ice sheet. *Nature Geoscience*, *13*(2), 132-137.
- Mouginot, J., Scheuchl, B., & Rignot, E. (2017). *MEaSURES Antarctic Boundaries for IPY 2007-2009 from Satellite Radar, Version 2*.
- Mouyen, M., Longuevergne, L., Steer, P., Crave, A., Lemoine, J. M., Save, H., & Robin, C. (2018). Assessing modern river sediment discharge to the ocean using satellite gravimetry. *Nat Commun*, *9*(1), 3384. <https://www.ncbi.nlm.nih.gov/pubmed/30139937>
- Mu, D., Yan, H., Feng, W., & Peng, P. (2017). GRACE leakage error correction with regularization technique: Case studies in Greenland and Antarctica. *Geophysical Journal International*.

- Navarra, A., & Simoncini, V. (2010). *A Guide to Empirical Orthogonal Functions for Climate Data Analysis* (1 ed.).
- Oppenheimer et al. (2019). Sea Level Rise and Implications for Low Lying Islands, Coasts and Communities. In *IPCC Special Report on the Ocean and Cryosphere in a Changing Climate*. Cambridge, UK: Cambridge University Press.
- Palerme, C., Claud, C., Dufour, A., Genthon, C., Wood, N. B., & L'Ecuyer, T. (2017). Evaluation of Antarctic snowfall in global meteorological reanalyses. *Atmospheric Research*, *190*, 104-112.
- Paolo, F. S., Padman, L., Fricker, H. A., Adusumilli, S., Howard, S., & Siegfried, M. R. (2018). Response of Pacific-sector Antarctic ice shelves to the El Niño/Southern Oscillation. *Nat Geosci*, *11*(2), 121-126. <https://www.ncbi.nlm.nih.gov/pubmed/29333198>
- Peltier, W. R. (2004). GLOBAL GLACIAL ISOSTASY AND THE SURFACE OF THE ICE-AGE EARTH: The ICE-5G (VM2) Model and GRACE. *Annual Review of Earth and Planetary Sciences*, *32*(1), 111-149.
- Peltier, W. R., Argus, D. F., & Drummond, R. (2015). Space geodesy constrains ice age terminal deglaciation: The global ICE-6G\_C (VM5a) model. *Journal of Geophysical Research: Solid Earth*, *120*(1), 450-487.
- Peltier, W. R., Argus, D. F., & Drummond, R. (2018). Comment on “An Assessment of the ICE-6G\_C (VM5a) Glacial Isostatic Adjustment Model” by Purcell et al. *Journal of Geophysical Research: Solid Earth*, *123*(2), 2019-2028.
- Pritchard, H. D., Ligtenberg, S. R., Fricker, H. A., Vaughan, D. G., van den Broeke, M. R., & Padman, L. (2012). Antarctic ice-sheet loss driven by basal melting of ice shelves. *Nature*, *484*(7395), 502-505. <https://www.ncbi.nlm.nih.gov/pubmed/22538614>
- Purcell, A., Tregoning, P., & Dehecq, A. (2016). An assessment of the ICE6G\_C(VM5a)glacial isostatic adjustment model. *Journal of Geophysical Research: Solid Earth*, *121*(5), 3939-3950.
- Rémy, F., & Parouty, S. (2009). Antarctic Ice Sheet and Radar Altimetry: A Review. *Remote Sensing*, *1*(4), 1212-1239.
- Retzlaff, R., & Bentley, C. R. (1993). Timing of stagnation of ice stream C, West Antarctica from short-pulse-radar studies of buried surface crevasses.

- Journal of Glaciology*, 39, 553-561.
- Rignot, E. (2004). Accelerated ice discharge from the Antarctic Peninsula following the collapse of Larsen B ice shelf. *Geophysical Research Letters*, 31(18).
- Rignot, E., Jacobs, S., Mouginot, J., & Scheuchl, B. (2013). Ice-shelf melting around Antarctica. *Science*, 341(6143), 266-270.  
<https://www.ncbi.nlm.nih.gov/pubmed/23765278>
- Rignot, E., Mouginot, J., & Scheuchl, B. (2017). *MEaSURES InSAR-Based Antarctica Ice Velocity Map, Version 2*.
- Rignot, E., Mouginot, J., Scheuchl, B., van den Broeke, M., van Wessem, M. J., & Morlighem, M. (2019). Four decades of Antarctic Ice Sheet mass balance from 1979-2017. *Proc Natl Acad Sci U S A*, 116(4), 1095-1103.  
<https://www.ncbi.nlm.nih.gov/pubmed/30642972>
- Rodell, M., Velicogna, I., & Famiglietti, J. S. (2009). Satellite-based estimates of groundwater depletion in India. *Nature*, 460(7258), 999-1002.  
<http://www.ncbi.nlm.nih.gov/pubmed/19675570>
- Roy, K., & Peltier, W. R. (2015). Glacial isostatic adjustment, relative sea level history and mantle viscosity: reconciling relative sea level model predictions for the U.S. East coast with geological constraints. *Geophysical Journal International*, 201(2), 1156-1181.
- Save, H., Bettadpur, S., & Tapley, B. D. (2016). High-resolution CSR GRACE RL05 mascons. *Journal of Geophysical Research: Solid Earth*, 121(10), 7547-7569.
- Scambos, T. A., Bohlander, J. A., Shuman, C. A., & Skvarca, P. (2004). Glacier acceleration and thinning after ice shelf collapse in the Larsen B embayment, Antarctica. *Geophysical Research Letters*, 31(18). <Go to ISI>://WOS:000224125900002
- Scambos, T. A., Haran, T. M., Fahnestock, M. A., Painter, T. H., & Bohlander, J. (2007). MODIS-based Mosaic of Antarctica (MOA) data sets: Continent-wide surface morphology and snow grain size. *Remote Sensing of Environment*, 111(2-3), 242-257.
- Schröder, L., Horwath, M., Dietrich, R., Helm, V., van den Broeke, M. R., & Ligtenberg, S. R. M. (2019). Four decades of Antarctic surface elevation changes from multi-mission satellite altimetry. *The Cryosphere*, 13(2), 427-

- Schutz, B. E., Zwally, H. J., Shuman, C. A., Hancock, D., & DiMarzio, J. P. (2005). Overview of the ICESat Mission. *Geophysical Research Letters*, *32*(21).
- Seo, K. W., Kim, J.-S., Youm, K., Chen, J., & Wilson, C. R. (2021). Secular polar motion observed by GRACE. *Journal of Geodesy*, *95*(4).
- Seo, K. W., Oh, S., Eom, J., Chen, J., & Wilson, C. R. (2020). Constrained Linear Deconvolution of GRACE Anomalies to Correct Spatial Leakage. *Remote Sensing*, *12*(11).
- Seo, K. W., Wilson, C. R., Chen, J. L., & Waliser, D. E. (2008). GRACE's spatial aliasing error. *Geophysical Journal International*, *172*(1), 41-48. <Go to ISI>://WOS:000251669800004
- Seo, K. W., Wilson, C. R., Scambos, T., Kim, B. M., Waliser, D. E., Tian, B., et al. (2015). Surface mass balance contributions to acceleration of Antarctic ice mass loss during 2003-2013. *Journal of Geophysical Research-Solid Earth*, *120*(5), 3617-3627. <Go to ISI>://WOS:000356454500041
- Shepherd. (2018). Mass balance of the Antarctic Ice Sheet from 1992 to 2017. *Nature*, *558*(7709), 219-222. <https://www.ncbi.nlm.nih.gov/pubmed/29899482>
- Shepherd, A., Gilbert, L., Muir, A. S., Konrad, H., McMillan, M., Slater, T., et al. (2019). Trends in Antarctic Ice Sheet Elevation and Mass. *Geophysical Research Letters*, *46*(14), 8174-8183.
- Shepherd, A., Ivins, E. R., A, G., Barletta, V. R., Bentley, M. J., Bettadpur, S., et al. (2012). A reconciled estimate of ice-sheet mass balance. *Science*, *338*(6111), 1183-1189. <https://www.ncbi.nlm.nih.gov/pubmed/23197528>
- Slater, T., Lawrence, I. R., Otosaka, I. N., Shepherd, A., Gourmelen, N., Jakob, L., et al. (2021). Review article: Earth's ice imbalance. *The Cryosphere*, *15*(1), 233-246.
- Smith, B. E., Fricker, H. A., Joughin, I. R., & Tulaczyk, S. (2009). An inventory of active subglacial lakes in Antarctica detected by ICESat (2003-2008). *Journal of Glaciology*, *55*(192), 573-595. <Go to ISI>://WOS:000270415200001
- Spence, P., Holmes, R. M., Hogg, A. M., Griffies, S. M., Stewart, K. D., & England, M. H. (2017). Localized rapid warming of West Antarctic subsurface waters by remote winds. *Nature Climate Change*, *7*(8), 595-603. <Go to

ISI>://WOS:000406742500021

- Swenson, S., Chambers, D. P., & Wahr, J. (2008). Estimating geocenter variations from a combination of GRACE and ocean model output. *Journal of Geophysical Research: Solid Earth*, 113(B8).
- Swenson, S., & Wahr, J. (2006). Post-processing removal of correlated errors in GRACE data. *Geophysical Research Letters*, 33(8). <Go to ISI>://WOS:000237411400002
- Tapley, B. D., Watkins, M. M., Flechtner, F., Reigber, C., Bettadpur, S., Rodell, M., et al. (2019). Contributions of GRACE to understanding climate change. *Nat Clim Chang*, 5(5), 358-369. <https://www.ncbi.nlm.nih.gov/pubmed/31534490>
- team, I. (2018). Mass balance of the Antarctic Ice Sheet from 1992 to 2017. *Nature*, 558(7709), 219-222. <https://www.ncbi.nlm.nih.gov/pubmed/29899482>
- Thomas, E. R., van Wessem, J. M., Roberts, J., Isaksson, E., Schlosser, E., Fudge, T. J., et al. (2017). Regional Antarctic snow accumulation over the past 1000 years. *Climate of the Past*, 13(11), 1491-1513.
- Treichler, D., & Kääb, A. (2016). ICESat laser altimetry over small mountain glaciers. *The Cryosphere*, 10(5), 2129-2146.
- Van Wessem, J. M., Reijmer, C. H., Morlighem, M., Mouginit, J., Rignot, E., Medley, B., et al. (2014). Improved representation of East Antarctic surface mass balance in a regional atmospheric climate model. *Journal of Glaciology*, 60(222), 761-770.
- Velicogna, I., Sutterley, T. C., & van den Broeke, M. R. (2014). Regional acceleration in ice mass loss from Greenland and Antarctica using GRACE time-variable gravity data. *Geophysical Research Letters*, 41(22), 8130-8137.
- Velicogna, I., & Wahr, J. (2013). Time-variable gravity observations of ice sheet mass balance: Precision and limitations of the GRACE satellite data. *Geophysical Research Letters*, 40(12), 3055-3063. <Go to ISI>://WOS:000321951300032
- Wahr, J., Molenaar, M., & Bryan, F. (1998). Time variability of the Earth's gravity field: Hydrological and oceanic effects and their possible detection using GRACE. *Journal of Geophysical Research-Solid Earth*, 103(B12), 30205-30229. <Go to ISI>://WOS:000077966900027

- Wang, F., Bamber, J. L., & Cheng, X. (2015). Accuracy and Performance of CryoSat-2 SARIn Mode Data Over Antarctica. *Ieee Geoscience and Remote Sensing Letters*, 12(7), 1516-1520. <Go to ISI>://WOS:000356543100017
- Whitehouse, P. L., Gomez, N., King, M. A., & Wiens, D. A. (2019). Solid Earth change and the evolution of the Antarctic Ice Sheet. *Nat Commun*, 10(1), 503. <https://www.ncbi.nlm.nih.gov/pubmed/30700704>
- Williams, S. D. P., Moore, P., King, M. A., & Whitehouse, P. L. (2014). Revisiting GRACE Antarctic ice mass trends and accelerations considering autocorrelation. *Earth and Planetary Science Letters*, 385, 12-21.
- Wingham, D. J., Francis, C. R., Baker, S., Bouzinac, C., Brockley, D., Cullen, R., et al. (2006). CryoSat: A mission to determine the fluctuations in Earth's land and marine ice fields. *Natural Hazards and Oceanographic Processes from Satellite Data*, 37(4), 841-871. <Go to ISI>://WOS:000238187800026
- Wouters, B., Bamber, J. L., van den Broeke, M. R., Lenaerts, J. T. M., & Sasgen, I. (2013). Limits in detecting acceleration of ice sheet mass loss due to climate variability. *Nature Geoscience*, 6(8), 613-616.
- Xu, P. (1998). Truncated SVD methods for discrete linear ill-posed problems. *Geophysical Journal International*, 135(2), 505-514.
- Zwally, H. J., Mario, B. G., Matthew, A. B., & Jack, L. S. (2012). Antarctic and Greenland Drainage System, GSFC Cryospheric Sciences Laboratory, at [http://icesat4.gsfc.nasa.gov/cryo\\_data/ant\\_grn\\_drainage\\_systems.php](http://icesat4.gsfc.nasa.gov/cryo_data/ant_grn_drainage_systems.php).

## 국문요약

지난 수 십 년 간, 남극의 얼음 질량 변화에 대한 우리의 지식은 인공위성 관측과 지구 물리 모델링 기술의 발전에 의해 비약적으로 향상되어 왔다. 인공위성 관측은 진행중인 남극 얼음 질량 손실과 가속화를 설명할 수 있는 메커니즘들을 지속적으로 제안하고 있으며, 이들을 고려한 모델링은 미래에 진행될 남극 빙하 손실을 정량적으로 산출하고 있다. 현재의 관측과 모델링 모두는 남극의 얼음 배출이 향후에 점차 가속화 될 것이라고 예측하고 있다. 이러한 증가율이 지속된다면, 남극은 가까운 미래에 해수면 상승을 유발시키는 첫번째 기여자가 될 것이다. 남극에서 배출될 빙하의 질량을 정확하게 예측하기 위해서는 진행중인 얼음 질량 손실에 대한 지속적인 관찰과 함께, 그것의 원인 기작을 규명하는 일이 요구된다.

남극의 얼음 질량 변화는 각 빙하마다 비균질하게 발생하고 있으며, 개별 빙하의 동력학은 대기와 해양 순환, 그리고 고체 지구의 변동성 등 다양한 지구 시스템 구성 요소들의 영향을 받고 있다. 각 요소들이 얼음 질량 변화에 미치는 물리적 기작을 보다 정확히 이해하고, 미래 질량 변화 예측의 불확실성을 해소하기 위해서는 이들을 총 망라하는 다학제간 연구가 필요하다. 이러한 흐름의 일환으로, 본 학위 논문에서는 기후 모델들과 원격 탐사 데이터를 활용하여 남극의 얼음 질량 변화를 분석한 세 개의 연구들이 수행되었다.

첫번째 연구는 얼음 질량 변화와 강설량의 관계를 조사한 것으로, 지구 시스템 내의 기권과 빙권 간의 상호작용에 대해 다루고 있다. 조사 결과, 최근 수 십 년 간 발생한 남극의 강설은 얼음 질량 변화의 경년 변동성의 대부분을 설명하고 있었으며, 동 시기 진행된 남극 얼음 질량 손실의 가속화의 약 30%가 강설량 변화의 기여임을 발견하였다. 또한 추가적인 통계분석을 통해, 이러한 강설량 변화가 남반구 극진동 (Southern Annular Mode, SAM)

이라고 불리우는 남반구 고위도의 주기적 기후변화와 밀접한 관련이 있음도 발견하였다.

두 번째 연구에서는 남극 얼음 질량 변화 관측의 해상도를 높이고자 하였다. 이는 빙하 동력학 모델들의 초기 조건을 단일 빙하와 같은 작은 규모에서 효과적으로 제약하기 위한 목적이다. 해상도 증가를 위해, 인공위성 중력계와 고도계 관측 데이터를 융합하는 새로운 선형 역산법을 개발하였다. 역산법의 적용 결과, 남극 대륙 전체의 얼음 질량 변화 (2003-2016) 를 약 27km의 높은 공간 해상도와 함께 한 달의 짧은 샘플링 간격으로 확인할 수 있는 데이터를 산출하였다. 이 연구에서 만든 데이터는 인공위성 중력계나 고도계를 독립적으로 활용하는 것에 비해 더 높은 정확도를 가질 것이라 추측된다. 예를 들어, 새로운 데이터를 활용하여 계산한 남극의 빙하 별 질량 변화는 각 센서를 따로 활용하는 것에 비해, Input-Output 방법이라는 독립적인 관측 결과와 더 높은 유사성을 보이고 있다.

세 번째 연구에서는 남극 빙하 하부의 고체 지구가 유발하는 후빙기 반동 (Glacial Isostatic Adjustment, GIA) 효과를 추정하고자 하였다. 이는 현재의 기술로 관측이 불가능한 GIA 효과가 얼음 질량 관측에 미치는 불확실성을 경감시키기 위한 목적으로 수행되었다. GIA효과를 분리시키기 위해, 앞서 수행한 고해상도 질량 추산 데이터와 다수의 기후모델을 서로 비교하였다. 그 결과, 서남극 로스 빙봉 근처에 위치한 캄 빙류 (Kamb Ice Stream) 하부의 GIA 효과가 효과적으로 분리될 수 있었다. 계산 값을 선행 연구에서 개발된 후빙기 반동 모델들과 비교한 결과, 대부분의 모델들이 캄 빙류의 후빙기 반동을 과대추정하고 있음도 발견하였다. 현존하는 다수의 GIA 모델들에서 캄 빙류 하부의 후빙기 반동 효과가 남극에서 가장 높게 모의되고 있다는 사실을 감안할 때, 이 발견은 모델들의 불확실성을 재고한다는 점에서 남극 얼음 질량 변화에 대한 기존 관측 결과에 시사하는 바가 크다.

세 연구의 결과를 종합한 남극 빙하 배출량 추정과 그에 따른 해수면 상승 예측이 논문의 마지막 장에 제시되어 있다. 이 결과는 대기과 고체 지구의 변동성을 고려함과 동시에, 개별 빙하의 해수면 상승 기여도를 예측하였다는 점에서 이전의 연구들과 차별된다.

**주요어:** 남극, 얼음 질량 변화, 해수면 변화, 인공위성 원격탐사, 지구물리 역산, 후빙기 반동  
**학번:** 2016-30431